Photonic quantum memory and atom-cavity interactions

Chanchal

A thesis submitted for the partial fulfillment of

the degree of Doctor of Philosophy

Department of Physical Sciences

Indian Institute of Science Education & Research (IISER) Mohali

Knowledge city, Sector 81 SAS Nagar, Manauli PO 140306 Punjab, India

October 2023

Dedicated to my parents

for their endless love and support...

Declaration

The work presented in this thesis has been carried out by me under the guidance of Dr. Sandeep K. Goyal at the Indian Institute of Science Education and Research Mohali. This work has not been submitted in part or in full for a degree, a diploma, or a fellowship to any other university or institute. Whenever contributions of others are involved, every effort is made to indicate this clearly, with due acknowledgement of collaborative research and discussions. This thesis is a bonafide record of original work done by me and all sources listed within have been detailed in the bibliography.

Chanchal

In my capacity as the supervisor of the candidate's thesis work, I certify that the above statements by the candidate are true to the best of my knowledge.

Supervisor:

Dr. Sandeep K. Goyal

Acknowledgements

First and foremost, I would like to express my sincere gratitude to my supervisor Dr. Sandeep K. Goyal, for his consistent guidance, support, and encouragement during my Ph.D. His ideas, valuable discussions, and insightful feedback, even during the most challenging times, guided me through all stages of my research and made this thesis possible. I am grateful for his valuable time, expertise, and guidance throughout this research.

I would also like to thank my collaborators, Dr. Christoph Simon and Dr. G. P. Teja, for their useful discussions and feedback, which helped me in my research and expanded my knowledge.

I also thank my doctoral committee members, Dr. Kinjalk Lochan, and Dr. Manabendra Nath Bera.

Finally, I would like to thank my family and friends for their constant support and encouragement.

Abstract

Photons have shown dominance in quantum information processing tasks and long-range quantum communication. Their ability to travel long distances without interacting with the external environment makes them excellent flying qubits. However, certain photonic quantum information processing tasks require the faithful storage and retrieval of single photons while preserving their internal states. This requires a quantum memory, a device that can store and retrieve single photons on demand. It is accomplished through controlled and reversible mapping of the photonic state onto the atomic state.

Apart from storing single photons, engineering and manipulating the quantum states of light is another key requirement in photonic quantum information processing. Atom-cavity interactions are prominently used to achieve this goal as it can provide a strong coupling between single atoms and photons. Furthermore, the strong interaction between atoms and photons allows us to implement the quantum gates between atoms and photons which is essential in order to implement quantum information processing tasks. This thesis focuses on the quantum memories and atom-cavity interactions, the two major components of photonic quantum information processing.

In the first part of the thesis, we present a method to store the internal states of photons using the intra-atomic frequency-comb protocol. We show that I-AFC is capable of storing the polarization states and OAM modes efficiently, which can be employed to store the vector-vortex states. Further, we show that a single atom containing a frequency comb coupled to an optical cavity can work as an efficient quantum memory. This provides us with the possibility to realize robust and efficient

on-chip quantum memory suitable for integrated photonic chips.

In the second part, we discuss the complete input-output theory in the context of atom-cavity interactions. It provides a complete description of the interaction of an input pulse prepared in an arbitrary quantum state interacting with a local quantum system. We apply this theory to investigate the photon-subtraction operation using an atom-cavity system. This reveals the multi-modal nature of the output state upon the photon subtraction process and provides a clear picture of the photon-subtraction process.

Publications

1. **Chanchal**, G. P. Teja, Christoph Simon, and Sandeep K. Goyal. Storing vector-vortex states of light in an intra-atomic frequency-comb quantum memory. Phys. Rev. A, 104:043713, Oct 2021.

2. **Chanchal**, G. P. Teja, and Sandeep K. Goyal. Intra-atomic frequency-comb-based photonic quantum memory using single-atom-cavity setup. Phys. Rev. A, 107:012614, Jan 2023.

3. **Chanchal** and Sandeep K. Goyal. Investigating multimodal nature of photon subtraction process using atom-cavity system. (Manuscript in preparation)

4. [†]G. P. Teja and **Chanchal**. Distillation of optical Fock states using atom-cavity systems. Phys. Rev. Appl., 20:044049, Oct 2023.

[†]Not included in the thesis

Contents

Chapter 1

Introduction

Classical computation is based on encoding the given information in terms of bits that are binary numbers. The classical bit can be either 0 or 1. In quantum information processing, we deal with quantum bits or qubits, representing the equivalent of the classical bit. A qubit can be a physical system whose quantum state can also be represented by 0 and 1. Specifically, it represents a two-level quantum system with states $|0\rangle$ and $|1\rangle$, which is associated with a two-dimensional Hilbert space. However, the key difference from classical computation arises from the fact that, unlike the classical case, the qubit can be in an arbitrary superposition of the two quantum states $|0\rangle$ and $|1\rangle$. Thus, the quantum state can be written as $|\Psi\rangle = \alpha\,|0\rangle + \beta\,|1\rangle$, with $\alpha,\beta \in \mathbb{C}$ [1]. The states $|0\rangle$ and $|1\rangle$ are often known as computational basis states, as they form a basis in the two-dimensional complex vector space. Quantum superposition serves as an important resource in quantum computation and quantum information processing. This concept can be extended to multiple qubits. This can be used to take advantage of another key ingredient from quantum mechanics known as quantum entanglement, which results in the correlation of multiple qubits. Quantum superposition and quantum entanglement are the two powerful and the key resources of quantum computing and quantum information processing [1, 2].

For efficient quantum computation and quantum information processing, we require quantum systems with a long coherence time and a high degree of control. There are several suitable candidates which can be used to encode quantum infor-

mation, such as stationary qubits using nuclear spins, quantum dots, superconducting qubits, trapped ions, and flying qubits using photons. Photons are among the strongest candidates for long-distance quantum communication and quantum computation [3, 4]. Some of the areas where photonic quantum information processing has shown dominance include linear optical quantum computation [5], quantum key distribution [6, 7], quantum teleportation [8, 9], and quantum repeaters [10]. Photons are a natural choice for quantum communication and quantum information processing as they can travel great distances, are easy to manipulate, and do not interact with the environment. Polarization, time bin, and orbital angular momentum [3] are the typical degrees of freedom of photons that are used for quantum information processing.

Although photons serve as excellent flying qubits, storing and retrieving the photons in an efficient and controllable way is one of the biggest challenges in photonic quantum information processing tasks. Storing single photons requires an additional component, an optical quantum memory that can store and emit single photons on demand. The basic idea behind a quantum memory is the light-matter interactions through which a controlled reversible transfer of the photonic quantum information between a light field and a material system is possible [11, 12, 13].

Apart from storing light using a quantum memory, engineering and manipulating the quantum states of light is another key requirement in photonic quantum information processing. Subtracting a single photon from the input field [14], generating Schrödinger cat states [15], producing single photons [16, 17], photon-blockade [18, 19] are some of the examples which engineer quantum states of light and manipulate them. The common ground among all these examples is that they all exploit atom-cavity interactions. Atom-cavity interactions not only allow for strong coupling of a single atom with light but also works as an interface between the photonic and the atomic qubits. This interface can be further used to implement the atom-photon gates and map the photonic state to the atomic state [20].

In this thesis, we mainly discuss these two important aspects of photonic quantum information processing: photonic quantum memory and the atom-cavity interactions.

In the first part of the thesis, we concentrate on optical quantum memory, which is used to store and retrieve single photons. It serves as an essential component in quantum information processing applications such as quantum networks [21, 22], long-range quantum communication [23] and quantum repeaters [24, 25]. Quantum repeater is one of the most important applications of quantum memory. It extends the quantum communication range, which is limited by optical fiber losses. Classical communication uses amplifiers to overcome this loss which can not work in quantum communication since we can not copy the quantum information (also known as the no-cloning theorem). Thus, the quantum repeater is used as an equivalent element of an amplifier. The key idea is to distribute the entanglement between the end nodes A and B by breaking the required transmission distance between A and B into smaller segments. To achieve this, entanglement swapping is used, which generates long-range entanglement by establishing entanglement between shorter nodes. This requires a quantum memory at each sub-node which stores the entanglement until the entire link is ready between the end nodes A and B [24, 12, 25].

Most quantum memory protocols are based on the reversible mapping of the photonic quantum information onto an ensemble of atoms, where the input photon is stored as a collective excitation delocalized over all the atoms in the ensemble. The stored photon is retrieved using a set of control pulses, resulting in controlled storage.

Some of the standard ensemble based quantum memory protocols include electromagnetically induced transparency (EIT) [26, 27, 28, 29], controlled reversible inhomogeneous broadening (CRIB) [30, 31, 32, 33, 34], gradient echo memory (GEM), [35, 36, 37], Raman memory [38, 39, 40, 41, 42], photon-echo using atomic frequency comb (AFC) [43, 44, 45, 46, 47, 48] and intra-atomic frequency comb (I-AFC) [49, 50, 51]. The maximum storage time in these quantum memories can reach up to micro seconds.

If we consider the current status of the different quantum memory protocols, the best demonstrated efficiencies are 92% for quantum memory based on EIT [28, 52], followed by 87% for GEM [37], 82% for the Raman protocol [42], 35% for AFC-based memory [53] and 15% for the CRIB protocol [35].

One of the major challenges in implementing the photonic quantum information processing tasks is to not only store and retrieve the photons but also preserve their internal states in an efficient and controllable way. Polarization, orbital angular momentum (OAM) and time-bins are some of the most commonly used degrees of freedom of photons used in quantum information processing. The polarization space is two-dimensional, while the OAM space is potentially infinite-dimensional, which gives a huge advantage in terms of high information-carrying capacity in individual photons.

Out of all the quantum memory schemes discussed above, EIT, Raman, and AFC-based quantum memory have been enabled to store both the polarization and OAM modes [54, 55, 56, 57]. However, only the EIT protocol has been used to store the polarization and the OAM modes simultaneously [54]. CRIB-based protocol with two orthogonal transitions has also been proposed to store polarization [58], while GEM has been shown to store spatial modes [59]. Further, quantum memory based on GEM and AFC has been shown to store time-bin qubits [60, 61].

In this thesis, we mainly focus on I-AFC-based quantum memory. The I-AFC is a frequency comb constructed from the dipole-allowed transitions between the hyperfine levels of the ground state and the excited state of an atom. The degeneracy in the hyper-fine levels of the ground and excited states is lifted by applying an external magnetic field. Since each allowed transition will have a natural broadening giving Lorentzian lineshape function, these multiple transitions between the ground and excited states give a frequency comb-like structure for each atom. Due to the periodicity of the frequency comb, the probability of the photon emission maximizes at time $t = 2\pi m/\Delta$ for integer m. As a result, the input light gets re-emitted, resulting in a photon-echo. The echo-time can be adjusted by changing the comb spacing Δ, which is, in turn, controlled by the strength of the applied magnetic field. In this way, the I-AFC gives a fixed storage time of $2\pi/\Delta$ and works as a delay line. To obtain on-demand storage, the excitation is usually transferred from the excited state to a spin state with long lifetime by applying a control field. Applying another control field transfers the excitation back to the excited state causing the photon-echo at an appropriate time.

Using quantum memory based on I-AFC, we present a scheme to store vector-vortex (VV) states of light. VV states are the quasi-entangled or non-separable states of light between the polarization and OAM degree of freedom (DOF) [62, 54]. They have various applications in quantum information processing tasks and quantum metrology [63, 64, 65]. We show that I-AFC is a natural candidate to store the VV states by showing that it can individually store the polarization and OAM modes efficiently.

We show that if the atoms are distributed homogeneously throughout the atomic ensemble, then the OAM modes can be stored perfectly at low temperatures. However, at high temperatures, the Doppler shift may affect the quality of storage. In order to store polarization states of light, we need to prepare an ensemble that contains two frequency combs corresponding to two orthogonal polarizations. Further, if the two frequency combs are identical, then the storage of the polarization states is perfect. Nonidentical combs might result in imperfect storage. The I-AFC system capable of storing both LG modes and the polarization states can be employed to store VV beams. We also discuss how I-AFCs in Cs and Rb atoms can work as promising candidates for storing these internal modes of light [51].

In addition to efficient storage of multiple degrees of freedom of photon, achieving scalability in quantum information processing is another big challenge. To gain scalability and practical advantage in quantum information processing, many efforts are being devoted to integrated photonic chips [66, 67, 68, 69]. On-chip single photon sources, on-chip beamsplitters, and on-chip photon detectors have already been implemented on an integrated platform [70, 71, 72, 73, 74]. However, on-chip quantum memory is still a work in progress and is a highly sought after device after the emergence of integrated photonic chip platforms for quantum information processing [75, 76]. Since most of the currently available quantum memory protocols require atomic ensembles or bulk materials to store photons, this creates difficulty for their on-chip integration.

Here, we present a multi-mode photonic quantum memory protocol using only a single-atom-cavity setup. A single atom placed in an optical cavity allows efficient coupling between the atom and the field. Also, by choosing the atom-cavity param-

eters properly, one can modify the rate of decay of the atom into the cavity mode, which results in the pre-dominant emission of the photon into a well-defined cavity mode, also known as the Purcell effect. We describe how a single atom containing a frequency comb coupled to an optical cavity in the Purcell regime is enough to store photons efficiently [77].

The joint single-atom-cavity setup results in a photon-echo, similar to the I-AFC-based quantum memory protocol. This provides the possibility of a robust and efficient on-chip quantum memory suitable for integrated photonic chips. The maximum theoretical efficiency in this scheme can reach up to $\sim 100\%$. Further, the proposed protocol can efficiently store time-multiplexed photons, along with their polarization degree of freedom, hence providing multimode photonic quantum memory. We also discuss the possible implementation of this scheme with the existing techniques considering realistic systems such as Cs and Rb atoms coupled to nanophotonic waveguide cavities. Further, since this scheme requires only a frequency comb coupled to a cavity, it can also be implemented using the quantum dots inside a cavity.

In the second part of this thesis, we discuss the complete and accurate description of the atom-cavity interactions and use it to describe the photon subtraction operation based on the atom-cavity system.

The standard formalism to tackle the dynamics of a local quantum system driven by an input field is based on the conventional input-output theory [78]. However, it has certain limitations. Although it can provide the amplitude and the intensity of the output field mode for a given input field interacting with a local quantum system, however, it becomes challenging to use this approach if we want to obtain the exact quantum state of the output field mode. For example, the generation of Schrödinger cat state has been shown experimentally by reflecting an input coherent state from an atom-cavity system. If we want to study the dynamics of this system theoretically, we need to know the quantum state of the output field mode to confirm the generation of the cat state, which becomes difficult using the standard input-output theory. Another drawback of the conventional input-output theory is that it always provides a single output field mode corresponding to a given input field

mode. However, this is not always true, and for a single mode input field, the output field may get scattered over multiple modes. In such cases, we require a more general and complete input-output theory that can completely describe the interaction of an input field pulse prepared in an arbitrary quantum state with a local quantum system.

At this point, the complete input-output theory using quantum pulses comes to the rescue [79, 80]. This is based on the master equation formalism, and can provide complete information of the dynamics of an atom-cavity system driven by an input pulse prepared in an arbitrary quantum state [79, 80].

We apply this theory to study the photon subtraction operation based on atom-cavity interactions [14]. Photon subtraction process uses an atom-cavity system with a lambda-type three-level atom with two ground states ($|g\rangle, |s\rangle$) and one excited state ($|e\rangle$). The two transitions of the atom, $|g\rangle \leftrightarrow |e\rangle$ and $|s\rangle \leftrightarrow |e\rangle$ are coupled to the two orthogonal polarization through the two cavity modes $\hat{a}$ and $\hat{b}$, respectively [14]. The atom is initially prepared in the ground state $|g\rangle$. By adjusting the atom-cavity parameters properly, for an input pulse driving the cavity $\hat{a}$, the atomic population can be transferred from $|g\rangle$ to $|s\rangle$, resulting in a single photon emission into the cavity mode $\hat{b}$.

We investigate this photon subtraction process using complete input-output theory, which reveals that for an input pulse containing more than one photon, although a single photon is always removed from the input field, the output field after the photon subtraction process is scattered over multiple modes. Further, we observe that each output mode carries a different amount of excitation, and the usual single mode description of the photon-subtraction process as described in [14] fails. We evaluate the photon subtraction process by considering different quantum states of the input field and also analyze the state of the output field modes in each case. This complete description provides a clear and better understanding of the photon-subtraction process, which is an essential tool for generating non-classical states of light [81, 82, 83, 84, 85, 86] and testing the fundamental nature of quantum mechanics [87, 88].

This thesis is organised as follows

Part I :

- In chapter 2, we introduce the formalism of interaction between an atom and an external electromagnetic field using the semiclassical description. Further, we discuss the paraxial wave equation, which is used to describe the dynamics of an electric field passing through an ensemble of atoms. We also discuss the quantization of the classical electromagnetic field.
- In chapter 3, we discuss the atom-cavity interactions. We also introduce the standard input-output theory, which is used to describe the dynamics of an input quantum field driving an atom-cavity system.
- In chapter 4, we introduce the quantum memory protocols based on atomic frequency comb (AFC) and intra-atomic frequency comb (I-AFC).
- Chapter 5 describes the storage of multiple degrees of freedom using I-AFC-based quantum memory. In this chapter, we also discuss the factors that affect the storage of polarization and OAM, and we also discuss how Cs and Rb atoms can work as promising candidates to implement this scheme.
- In chapter 6, we present an efficient optical quantum memory scheme that just uses a single atom with I-AFC coupled to an optical cavity.

Part-II :

- In chapter 7, we introduce the theory of cascaded quantum systems, and using this, we introduce the complete input-output theory of quantum pulses in the context of atom-cavity interactions.
- In chapter 8, we discuss the photon subtraction process using an atom-cavity system using the general input-output theory.
- In chapter 9, we conclude the thesis.

Part I

Chapter 2

Light-matter interactions

Light-matter interactions play a vital role in photonic quantum information processing and quantum communication. Storing photonic quantum information [12], implementing quantum gates [20], quantum sensing [89], and generating atom-photon entanglement [90] are some of the examples which make use of controlled interactions between light and atoms.

In this chapter, we discuss the theoretical framework required to describe the interaction of light with atoms. We start with the standard Hamiltonian, which describes the interaction between a two-level atom and an external electromagnetic field using the semiclassical description. In this, the atom is considered to be a quantum mechanical system with a ground and an excited state, while the external electromagnetic field is treated classically. We also discuss the Maxwell-Schrödinger equations used to describe the dynamics of an electric field passing through an ensemble of atoms. In the end, we discuss the quantum mechanical description of the electromagnetic field.

2.1 Interaction between an atom and external electromagnetic field

In this section, we discuss the interaction of an atom with an electromagnetic field. We introduce the semiclassical description in which the electromagnetic field is treated classically, while the atom is treated as a quantum two-level system with a ground state $|g\rangle$ and an excited state $|e\rangle$.

The Hamiltonian for an electron of mass m and charge e bound to an atom interacting with an external field is given by [91]

$$\hat{H} = \frac{(\hat{\mathbf{p}} + e\mathbf{A}(\mathbf{r},t))^2}{2m} - e\phi(\mathbf{r},t) + V(r), \tag{2.1}$$

where $\hat{\mathbf{p}}$ is the canonical momentum operator given by $-\mathrm{i}\hbar\boldsymbol{\nabla}$ (in position representation), $V(r)$ is the electrostatic potential, which represents the Coulomb interaction between the electron and the nucleus, while $\mathbf{A}(\mathbf{r},t)$ and $\phi(\mathbf{r},t)$ are the vector and scalar potentials of the external field given by [92]

$$\mathbf{E} = -\boldsymbol{\nabla}\phi - \frac{\partial \mathbf{A}}{\partial t}, \tag{2.2}$$

$$\mathbf{B} = \boldsymbol{\nabla} \times \mathbf{A}. \tag{2.3}$$

The time-dependent Schrödinger equation corresponding to the Hamiltonian in Eq. (2.1) describes the motion of the free electron and is given by

$$\mathrm{i}\hbar\frac{\partial}{\partial t}\psi(\mathbf{r},t) = \hat{H}\psi(\mathbf{r},t), \tag{2.4}$$

where $|\psi(\mathbf{r},t)|^2$ describes the probability of finding the electron at time t and position $\mathbf{r}$. In order to simplify the dynamics further, we note that the form of the above equation remains the same under the following gauge transformations [92, 91]

$$A'(\mathbf{r},t) = A(\mathbf{r},t) + \boldsymbol{\nabla}\chi(\mathbf{r},t), \tag{2.5}$$

$$\phi'(\mathbf{r},t) = \phi(\mathbf{r},t) - \frac{\partial\chi(\mathbf{r},t)}{\partial t}, \tag{2.6}$$

$$\psi'(\mathbf{r},t) = \psi(\mathbf{r},t)exp(-\mathrm{i}e\chi(\mathbf{r},t)), \tag{2.7}$$

where $\chi(\mathbf{r},t)$ is an arbitrary differentiable and real function of $\mathbf{r}$ and t. The electric and magnetic fields in Eqs. (2.2) and 2.3 remain invariant under these gauge transformations, whereas the vector and scalar potentials, $\mathbf{A}(\mathbf{r},t)$ and $\phi(\mathbf{r},t)$ respectively,

are gauge dependent. The wave function $\psi'(\mathbf{r},t)$ in Eq. (2.7) satisfies the following Schrödinger equation

$$\mathrm{i}\hbar\frac{\partial\psi'(\mathbf{r},t)}{\partial t} = H'\psi'(\mathbf{r},t), \tag{2.8}$$

where H' is simply given by

$$\hat{H}' = \frac{[\hat{\mathbf{p}} + e\mathbf{A}'(\mathbf{r},t)]^2}{2m} - e\phi'(\mathbf{r},t) + V(r), \tag{2.9}$$

with the scalar and vector potentials now given by Eq. (2.5) and (2.6), respectively. This gauge invariance gives an additional freedom to work in the Coulomb gauge, in which the vector potential satisfies $\boldsymbol{\nabla}\cdot\mathbf{A} = 0$ and $\phi = 0$. Under Coulomb gauge, Eq. (2.1) transforms to

$$\hat{H}' = \frac{[\hat{\mathbf{p}} + e(\mathbf{A} + \boldsymbol{\nabla}\chi)]^2}{2m} + e\frac{\partial\chi}{\partial t} + V(r), \tag{2.10}$$

which is now completely given in terms of $\chi(\mathbf{r},t)$. Also, the vector potential in the Coulomb gauge satisfies the following wave equation

$$\nabla^2 A - \frac{1}{c^2}\frac{\partial^2 A}{\partial t^2} = 0, \tag{2.11}$$

where c is the velocity of light. The solution of Eq. (2.11) can be written as

$$\mathbf{A} = \mathbf{A_0}e^{\mathrm{i}(\mathbf{k}.\mathbf{r}-\omega t)} + c.c, \tag{2.12}$$

where $\mathbf{k}$ is the wave vector of the field and the magnitude $|\mathbf{k}| = \omega/c = 2\pi/\lambda$ represents the wave number. For optical wavelengths, λ is in the range of 400–700 nm, and for $\mathbf{r}$ with typical atomic dimensions of $\sim 10^{-10}$ m, the term $\mathbf{k}\cdot\mathbf{r} \ll 1$. Thus, over the spatial dimensions of an atom, the vector potential is uniform and can be written as $\mathbf{A}(\mathbf{r},t) \simeq \mathbf{A}(t)$. This is known as the dipole approximation, which is extensively used in quantum optics [91, 93]. Applying the dipole approximation and taking the gauge function $\chi(\mathbf{r},t) = -\mathbf{A}(t)\cdot\mathbf{r}$, we have

$$\frac{\partial\chi(\mathbf{r},t)}{\partial t} = -\mathbf{r}\cdot\mathbf{E}(t), \;\; \boldsymbol{\nabla}\chi(\mathbf{r},t) = -\mathbf{A}(t). \tag{2.13}$$

Using this, the Hamiltonian in Eq. (2.10) finally becomes

$$\begin{aligned}\hat{H}' &= \frac{\hat{\mathbf{p}}^2}{2m} + e\mathbf{r}\cdot\mathbf{E}(t) + V(r)\\ &= \hat{H}_0 + e\mathbf{r}\cdot\mathbf{E}(t)\\ &= \hat{H}_0 - \hat{\mathbf{d}}\cdot\mathbf{E}(t),\end{aligned} \tag{2.14}$$

where $\hat{H}_0 = \dfrac{\hat{\mathbf{p}}^2}{2m} + V(r)$ is the Hamiltonian for the unperturbed electron in the absence of an external field. $\hat{\mathbf{d}} = -e\mathbf{r}$ is the dipole moment operator, and the term $\hat{\mathbf{d}} \cdot \mathbf{E}(t)$ describes the atom-field interaction. For a two-level atom with the ground state $|g\rangle$ and an excited state $|e\rangle$, the dipole moment operator becomes $\hat{\mathbf{d}} = \mathbf{d}_{eg} |e\rangle\langle g| + \mathbf{d}_{ge} |g\rangle\langle e|$, where $\mathbf{d}_{eg} = -\langle e|e\mathbf{r}|g\rangle$ is the transition dipole matrix element between the ground state and the excited state. Thus, in the semiclassical picture, the interaction between the atom and the external field is described by the term $\hat{\mathbf{d}}\cdot\mathbf{E}(t)$ and is a starting point for studying the light-matter interactions [91, 93].

In the next section, we discuss how the input light field gets affected as it propagates through an ensemble of atoms and discuss the standard paraxial wave equation that describes the propagation of the electric field through an ensemble of atoms.

2.2 Paraxial wave equation for propagation of light through a medium

In this section, we derive the paraxial wave equation, which is used in solving the dynamics for the propagation of the electric field through an ensemble of atoms. We start with Maxwell's equations for the propagation of electromagnetic field inside a non conducting material in the absence of free charges and currents which are given by [92]

$$\boldsymbol{\nabla} \cdot \epsilon_0 \mathbf{E} = -\boldsymbol{\nabla} \cdot \mathbf{P}, \tag{2.15}$$

$$\boldsymbol{\nabla} \cdot \mathbf{B} = 0, \tag{2.16}$$

$$\boldsymbol{\nabla} \times \mathbf{E} = -\frac{\partial \mathbf{B}}{\partial t}, \tag{2.17}$$

$$\boldsymbol{\nabla} \times \mathbf{B} = \mu_0 \epsilon_0 \frac{\partial \mathbf{E}}{\partial t} + \mu_0 \frac{\partial \mathbf{P}}{\partial t}, \tag{2.18}$$

where $\mathbf{P}$ is the atomic polarization. From the above equations, we can derive the wave equation for $\mathbf{E}$. Taking the curl of Eq. (2.17), we get

$$\begin{aligned} \boldsymbol{\nabla} \times (\boldsymbol{\nabla} \times \mathbf{E}) &= -\frac{\partial}{\partial t}(\boldsymbol{\nabla} \times \mathbf{B}), \\ \implies \boldsymbol{\nabla}(\boldsymbol{\nabla} \cdot \mathbf{E}) - \nabla^2 \mathbf{E} &= -\frac{\partial}{\partial t}(\boldsymbol{\nabla} \times \mathbf{B}). \end{aligned} \tag{2.19}$$

Substituting the value of $\boldsymbol{\nabla} \times \mathbf{B}$ from Eq. (2.18), we get

$$\boldsymbol{\nabla}(\boldsymbol{\nabla} \cdot \mathbf{E}) - \nabla^2 \mathbf{E} = -\mu_0 \epsilon_0 \frac{\partial^2 \mathbf{E}}{\partial t^2} - \mu_0 \frac{\partial^2 \mathbf{P}}{\partial t^2}. \tag{2.20}$$

In the absence of free charge, $\boldsymbol{\nabla} \cdot \mathbf{E} = 0$ and the wave equation then simply reduces to

$$\nabla^2 \mathbf{E} - \frac{1}{c^2} \frac{\partial^2 \mathbf{E}}{\partial t^2} - \mu_0 \frac{\partial^2 \mathbf{P}}{\partial t^2} = 0, \tag{2.21}$$

which is the standard second order wave equation in time and space. However, this can be further simplified to a first order wave equation under certain approximations, which will be discussed in the following section.

2.2.1 Slowly Varying Envelope Approximation

The general form of the solution for Eq. (2.21) can be written as [92]

$$\mathbf{E}(r,t) = \frac{1}{2} \boldsymbol{\mathcal{E}}(r,t) e^{i(\mathbf{k}.\mathbf{r} \pm \omega_0 t)} + c.c, \tag{2.22}$$

$$\mathbf{P}(r,t) = \frac{1}{2} \boldsymbol{\mathcal{P}}(r,t) e^{i(\mathbf{k}.\mathbf{r} \pm \omega_0 t)} + c.c, \tag{2.23}$$

where $\boldsymbol{\mathcal{E}}(r,t)$ and $\boldsymbol{\mathcal{P}}(r,t)$ are the complex time-dependent amplitudes for the electric field and the atomic polarization, respectively, ω_0 is the central frequency, and $k = \omega_0/c$ is the wave number of the incoming field. The terms $(\mathbf{k}.\mathbf{r} - \omega_0 t)$ and $(\mathbf{k}.\mathbf{r} + \omega_0 t)$ in the above equations correspond to the forward and backward propagating waves.

For simplicity, we can take $\hat{\mathbf{z}}$ as the direction of propagation of light, i.e., $\mathbf{k} = k\hat{z}$. Using Eqs. (2.22) and (2.23) and considering the forward propagating field, we can calculate each term in Eq. (2.21), which are given by

$$\nabla^2 \mathbf{E} = \frac{1}{2s} \left(\nabla^2 \boldsymbol{\mathcal{E}} + 2ik \frac{\partial \boldsymbol{\mathcal{E}}}{\partial z} - k^2 \boldsymbol{\mathcal{E}} \right) e^{i(kz - \omega_0 t)} + c.c, \tag{2.24}$$

$$\frac{\partial^2 \mathbf{E}}{\partial t^2} = \frac{1}{2} \left(\frac{\partial^2 \boldsymbol{\mathcal{E}}}{\partial t^2} - 2i\omega_0 \frac{\partial \boldsymbol{\mathcal{E}}}{\partial t} - \omega_0^2 \boldsymbol{\mathcal{E}} \right) e^{i(kz - \omega_0 t)} + c.c, \tag{2.25}$$

$$\frac{\partial^2 \mathbf{P}}{\partial t^2} = \frac{1}{2} \left(\frac{\partial^2 \boldsymbol{\mathcal{P}}}{\partial t^2} - 2i\omega_0 \frac{\partial \boldsymbol{\mathcal{P}}}{\partial t} - \omega_0^2 \boldsymbol{\mathcal{P}} \right) e^{i(kz - \omega_0 t)} + c.c. \tag{2.26}$$

Substituting these values into the wave equation, we get the following

$$\nabla^2 \boldsymbol{\mathcal{E}} + 2ik \frac{\partial \boldsymbol{\mathcal{E}}}{\partial z} - \frac{1}{c^2} \frac{\partial^2 \boldsymbol{\mathcal{E}}}{\partial t^2} + \frac{2i\omega_0}{c^2} \frac{\partial \boldsymbol{\mathcal{E}}}{\partial t} - \frac{1}{\epsilon_0 c^2} \frac{\partial^2 \boldsymbol{\mathcal{P}}}{\partial t^2} + \frac{2i\omega_0}{\epsilon_0 c^2} \frac{\partial \boldsymbol{\mathcal{P}}}{\partial t} + \frac{\omega_0^2}{\epsilon_0 c^2} \boldsymbol{\mathcal{P}} = 0. \tag{2.27}$$

Now, we apply the slowly varying envelope approximation (also called the paraxial approximation), in which it is assumed that the complex field amplitude, $\mathcal{E}(r,t)$ is a slowly varying function in space and time. Considering that $\boldsymbol{\mathcal{E}}$ and $\boldsymbol{\mathcal{P}}$ are slowly varying functions of z and t, we get [93]

$$\left|\frac{\partial^2\boldsymbol{\mathcal{E}}}{\partial z^2}\right| \ll \left|k\frac{\partial\boldsymbol{\mathcal{E}}}{\partial z}\right|, \left|\frac{\partial^2\boldsymbol{\mathcal{E}}}{\partial t^2}\right| \ll \left|\omega_0\frac{\partial\boldsymbol{\mathcal{E}}}{\partial t}\right|, \tag{2.28}$$

$$\left|\frac{\partial^2\boldsymbol{\mathcal{P}}}{\partial z^2}\right| \ll \left|k\frac{\partial\boldsymbol{\mathcal{P}}}{\partial z}\right|, \left|\frac{\partial^2\boldsymbol{\mathcal{P}}}{\partial t^2}\right| \ll \left|\omega_0\frac{\partial\boldsymbol{\mathcal{P}}}{\partial t}\right|, \tag{2.29}$$

and

$$\left|\frac{\partial\boldsymbol{\mathcal{E}}}{\partial z}\right| \ll |k\boldsymbol{\mathcal{E}}|, \left|\frac{\partial\boldsymbol{\mathcal{E}}}{\partial t}\right| \ll |\omega_0\boldsymbol{\mathcal{E}}|, \tag{2.30}$$

$$\left|\frac{\partial\boldsymbol{\mathcal{P}}}{\partial z}\right| \ll |k\boldsymbol{\mathcal{P}}|, \left|\frac{\partial\boldsymbol{\mathcal{P}}}{\partial t}\right| \ll |\omega_0\boldsymbol{\mathcal{P}}|. \tag{2.31}$$

This approximation is valid for the waves propagating along along the z-axis, having negligible spread in the transverse plane, i.e., the transverse profile of $\mathcal{E}$ is much larger than the optical wavelength, $\lambda_0 = 2\pi c/\omega_0$. On the other hand, in the frequency domain, it is justified for the waves with spectral width much smaller than the mean frequency of the light ω_0. Using the slowly varying envelope approximation, we finally arrive at the following wave equation [94]

$$\left[\frac{\partial^2}{\partial x^2} + \frac{\partial^2}{\partial y^2} + 2ik\left(\frac{\partial}{\partial z} + \frac{1}{c}\frac{\partial}{\partial t}\right)\right]\boldsymbol{\mathcal{E}}(r,t) = -\frac{\omega_0 k}{\epsilon_0 c}\boldsymbol{\mathcal{P}}(r,t). \tag{2.32}$$

We may write the above equation as

$$\left[\nabla_\perp^2 + 2ik\left(\frac{\partial}{\partial z} + \frac{1}{c}\frac{\partial}{\partial t}\right)\right]\boldsymbol{\mathcal{E}}(r,t) = -\frac{k^2}{\epsilon_0}\boldsymbol{\mathcal{P}}(r,t), \tag{2.33}$$

where $\nabla_\perp^2 = \frac{\partial^2}{\partial x^2} + \frac{\partial^2}{\partial y^2}$. This is the paraxial wave equation, the left-hand side of which corresponds to the evolution of the electric field in vacuum, while the polarization on the right-hand side acts as a source term that affects the propagation of the electric field inside the medium. Note that the $\nabla_\perp^2$ term leads to transverse effects and is necessary to describe the propagation of light field with a transverse profile through an ensemble of atoms.

However, for a plane wave having no transverse spatial variation, the term $\nabla_\perp^2$ vanishes and it gets reduced to a first order wave equation

$$\left(\frac{\partial}{\partial z} + \frac{1}{c}\frac{\partial}{\partial t}\right)\boldsymbol{\mathcal{E}}(z,t) = \frac{ik}{2\epsilon_0}\boldsymbol{\mathcal{P}}(z,t). \tag{2.34}$$

Thus, the electric field induces atomic polarization while propagating through the medium, which acts as a source term, and in turn, affects the further propagation of the electric field. Note that this paraxial wave equation corresponds to the forward propagating mode. If we consider the backward propagating mode in Eqs. (2.22) and 2.23, then the corresponding first order wave equation becomes

$$\left(\frac{\partial}{\partial z} - \frac{1}{c}\frac{\partial}{\partial t}\right)\boldsymbol{\mathcal{E}}(z,t) = \frac{ik}{2\epsilon_0}\boldsymbol{\mathcal{P}}(z,t). \tag{2.35}$$

Furthermore , the induced atomic polarization amplitude, $\mathcal{P}(z,t)$ in the paraxial wave equation is directly related to the dipole matrix element d_{eg} of the atom. If the state of the atom is described by the density matrix ρ, then the atomic polarization amplitude for an ensemble of two-level atoms is given by [93]

$$\mathcal{P}(z,t) = 2\mathcal{N}d^*_{eg}\rho_{eg}, \tag{2.36}$$

where $\rho_{eg} = \langle e|\rho|g\rangle$ denotes the coherence term of the atomic density matrix and $\mathcal{N}$ is the atomic number density.

The evolution of the atomic state is given by the Lindblad master equation, which incorporates the spontaneous decay rate of the atom due to its coupling with the environment and reads [95]

$$\begin{aligned}\frac{\mathrm{d}\rho}{\mathrm{d}t} &= -\frac{\mathrm{i}}{\hbar}[H,\rho] + \mathcal{D}(\rho),\\ &= -\frac{\mathrm{i}}{\hbar}[H,\rho] + \left(L\rho L^\dagger - \frac{1}{2}L^\dagger L\rho - \frac{1}{2}\rho L^\dagger L\right),\end{aligned} \tag{2.37}$$

where $\mathcal{D}(\rho)$ is the Lindblad dissipator and $L = \sqrt{\gamma}\,|g\rangle\langle e|$ is defined as the Lindblad jump operator or the collapse operator corresponding to the atomic decay rate γ. The paraxial wave equation in Eq. (2.34) and the density matrix equation for the atom in Eq. (2.37) form a self-consistent system of equations and are solved to obtain the complete dynamics of the electric field after interacting through an ensemble of atoms and are also known as the Maxwell-Schrödinger equations [93].

In the next section we introduce the Laguerre-Gauss (LG) modes, which are the solution of the paraxial wave equation in the free space and also discuss the integral form of this equation.

2.3 Paraxial wave equation in free space

The paraxial wave-equation in free space can be obtained by putting the source term in Eq. (2.33) to zero which is given by

$$\left[\nabla_\perp^2 + 2ik\left(\frac{\partial}{\partial z} + \frac{1}{c}\frac{\partial}{\partial t}\right)\right]\boldsymbol{\mathcal{E}}(r,t) = 0. \tag{2.38}$$

Laguerre-Gauss (LG) modes are the eigenmodes of the paraxial wave equation in free space [96, 97]. They are also the eigenmodes of angular momentum operators and possess certain OAM. In the cylindrical coordinates, the expression for the LG modes reads [96]

$$\begin{aligned} LG_p^\ell(r,\phi,z) = &\frac{C}{w(z)}\left(\frac{\sqrt{2}r}{w(z)}\right)^{|\ell|} L_p^{|\ell|}\left(\frac{2r^2}{w(z)^2}\right)\exp\left(\frac{-r^2}{w(z)^2}\right) \\ &\times \exp\left(\frac{\mathrm{i}kr^2}{2\bar{z}}\right)\exp[-\mathrm{i}(2p+|\ell|+1)\psi(z)]\exp(\mathrm{i}\ell\phi) \\ \equiv &f_\ell^p(r,z)\exp(\mathrm{i}\ell\phi), \end{aligned} \tag{2.39}$$

where

$$w(z) = w_0\sqrt{1+\left(\frac{z}{z_R}\right)^2},\ \bar{z} = \frac{z^2+z_R^2}{z}, \tag{2.40}$$

and $\psi(z) = \tan^{-1}\left(\frac{z}{z_R}\right)$ is the Gouy phase. Here ω_0 is the beam waist at $z = 0$, $z_R = \pi w_0^2/\lambda$ represents the Rayleigh range, C is the normalization constant, $L_p^{|\ell|}$ is the associated Laguerre polynomial, $p \geq 0$ is the radial index and $-\infty < \ell < \infty$ is the azimuthal index. $\ell\hbar$ is the OAM per photon for a given LG mode.

We can also write the paraxial wave equation in Eq. (2.38) in integral form by taking Fourier transforms in the transverse position ($\mathbf{r}_\perp \to \mathbf{q}$). The solution for the Fourier transformed electric field $\tilde{\mathcal{E}}(\mathbf{q},z,t)$ reads

$$\tilde{\mathcal{E}}(\mathbf{q},z,t) = \exp\left(\frac{q^2}{2\mathrm{i}k}z\right)\tilde{\mathcal{E}}\left(\mathbf{q},0,t-\frac{z}{c}\right). \tag{2.41}$$

Now, taking the inverse Fourier transform ($\mathbf{q} \to \mathbf{r}_\perp$), we get

$$\mathcal{E}(\mathbf{r}_\perp,z,t) = \mathcal{F}^{-1}\left[\exp\left(\frac{q^2}{2\mathrm{i}k}z\right)\right] * \mathcal{F}^{-1}\left[\tilde{\mathcal{E}}\left(\mathbf{q},0,t-\frac{z}{c}\right)\right], \tag{2.42}$$

where $*$ represents the convolution operation. Using the definition for convolution of two functions

$$f(x) * g(x) = \int_{-\infty}^{\infty} f(x')g(x - x')\ dx', \tag{2.43}$$

we can write the formal expression for $\mathcal{E}(\mathbf{r}_\perp, z, t)$ as

$$\mathcal{E}(\mathbf{r}_\perp, z, t) = \int M(\mathbf{r}_\perp - \mathbf{r}'_\perp, z)\mathcal{E}(\mathbf{r}'_\perp, 0, t - \frac{z}{c})d^2\mathbf{r}'_\perp, \tag{2.44}$$

where

$$M(\mathbf{r}_\perp, z) = \mathcal{F}^{-1}\left[\exp\left(\frac{q^2}{2ik}z\right)\right] = \frac{1}{2\pi}\int e^{i\mathbf{q}\cdot\mathbf{r}_\perp}e^{-iq^2z/2k}d^2\mathbf{q}. \tag{2.45}$$

Eq. (2.44) gives the evolution of electric field in vacuum which does not affect the transverse profile of the field. We will use this representation in chapter 5, where we will discuss the propagation of LG modes through an ensemble of atoms containing inta-atomic frequency comb.

2.4 Quantization of EM field

Until now, we considered the atom to be a quantum mechanical two-level system, while the electromagnetic field was considered classical. In this section, we discuss the quantization of the electromagnetic field, which will be used to describe the dynamics of an atom interacting with the quantized field. The free field is quantized by assuming the free space as a cubic cavity of length L and volume $V = L^3$. This cavity is considered a quantization cavity without any real boundaries. The solution of the wave equation for the vector potential $\mathbf{A}(\mathbf{r}, t)$ given in Eq. (2.11) upon imposing the travelling wave periodic boundary conditions can be written as [98]

$$\mathbf{A}(\mathbf{r}, t) = \sum_{\mathbf{k},\lambda} \hat{\mathbf{e}}_{\mathbf{k},\lambda}\big(A_{\mathbf{k},\lambda}e^{i(\mathbf{k}\cdot\mathbf{r}-\omega_k t)} - A^*_{\mathbf{k},\lambda}e^{-i(\mathbf{k}\cdot\mathbf{r}-\omega_k t)}\big), \tag{2.46}$$

which is expressed in terms of the superposition of plane waves with wave vector $\mathbf{k}$. This can be considered as the sum of contributions from different modes of the

cavity. Here $A_{\mathbf{k},\lambda}$ is the complex field amplitude, $\hat{\mathbf{e}}_{\mathbf{k},\lambda}$ is the polarization vector of the field, and $\omega_k = ck$. The components of the wave vector $\mathbf{k}$ here are given by

$$k_x = \frac{2\pi n_x}{L}, \tag{2.47}$$

$$k_y = \frac{2\pi n_y}{L}, \tag{2.48}$$

$$k_z = \frac{2\pi n_z}{L}, \tag{2.49}$$

with $n_x = n_y = n_z = 0, \pm 1, \pm 2, ...$

The electric and magnetic fields can be obtained from this vector potential by using Eq. (2.2) and (2.3) respectively which gives [98]

$$\mathbf{E}(\mathbf{r},t) = \mathrm{i}\sum_{\mathbf{k},\lambda} \hat{\mathbf{e}}_{\mathbf{k},\lambda}\omega_k \big(A_{\mathbf{k},\lambda}e^{\mathrm{i}(k\cdot r-\omega_k t)} - A^*_{\mathbf{k},\lambda}e^{-\mathrm{i}(k\cdot r-\omega_k t)}\big), \tag{2.50}$$

$$\mathbf{B}(\mathbf{r},t) = \mathrm{i}\sum_{\mathbf{k},\lambda} \frac{\mathbf{k}\times\hat{\mathbf{e}}_{\mathbf{k},\lambda}}{k}\omega_k \big(A_{\mathbf{k},\lambda}e^{\mathrm{i}(k\cdot r-\omega_k t)} - A^*_{\mathbf{k},\lambda}e^{-\mathrm{i}(k\cdot r-\omega_k t)}\big). \tag{2.51}$$

The total energy of the electromagnetic field inside the cavity can be written as

$$\begin{aligned} H &= \frac{1}{2}\int_V \left(\epsilon_0 \mathbf{E}\cdot\mathbf{E} + \frac{\mathbf{B}\cdot\mathbf{B}}{\mu_0}\right) dV \\ &= \epsilon_0 V \sum_{\mathbf{k},\lambda} \omega_k^2 \big(A_{\mathbf{k},\lambda}A^*_{\mathbf{k},\lambda} + A^*_{\mathbf{k},\lambda}A_{\mathbf{k},\lambda}\big) \end{aligned} \tag{2.52}$$

Next, the canonical conjugate variables q and p are introduced, which are related to $A_{\mathbf{k},\lambda}, A^*_{\mathbf{k},\lambda}$ as

$$A_{\mathbf{k},\lambda} = \frac{1}{2\omega_k\sqrt{\epsilon_0 V}}(\omega_k q_{\mathbf{k},\lambda} + \mathrm{i}p_{\mathbf{k},\lambda}), \tag{2.53}$$

$$A^*_{\mathbf{k},\lambda} = \frac{1}{2\omega_k\sqrt{\epsilon_0 V}}(\omega_k q_{\mathbf{k},\lambda} - \mathrm{i}p_{\mathbf{k},\lambda}). \tag{2.54}$$

The introduction of these variables q and p simplifies the energy of the field to the following form (from Eq. (2.52))

$$H = \frac{1}{2}\sum_{\mathbf{k},\lambda}\big(p^2_{\mathbf{k},\lambda} + \omega_k^2 q^2_{\mathbf{k},\lambda}\big). \tag{2.55}$$

This is the energy of a simple harmonic oscillator of unit mass. The quantization of the electromagnetic field is done by replacing these canonical conjugate variables

$q_{\mathbf{k},\lambda}$ and $p_{\mathbf{k},\lambda}$ by their respective quantum mechanical operators $\hat{q}_{\mathbf{k},\lambda}$ and $\hat{p}_{\mathbf{k},\lambda}$ which satisfy the following commutation relations

$$[\hat{q}_{\mathbf{k},\lambda}, \hat{q}_{\mathbf{k}',\lambda'}] = 0,\ [\hat{p}_{\mathbf{k},\lambda}, \hat{p}_{\mathbf{k}',\lambda'}] = 0,\ [\hat{q}_{\mathbf{k},\lambda}, \hat{p}_{\mathbf{k}',\lambda'}] = \mathrm{i}\hbar\delta_{\mathbf{k}\mathbf{k}'}\delta_{\lambda\lambda'}, \tag{2.56}$$

while the variables $A_{\mathbf{k},\lambda}$ and $A^*_{\mathbf{k},\lambda}$ are accordingly replaced by the annihilation and creation operators of harmonic ocillator i.e., $\hat{a}$ and $\hat{a^\dagger}$ respectively, such that [98, 91]

$$A_{\mathbf{k},\lambda} \to \sqrt{\frac{\hbar}{2\omega_k\epsilon_0 V}}\hat{a}, \tag{2.57}$$

$$A^*_{\mathbf{k},\lambda} \to \sqrt{\frac{\hbar}{2\omega_k\epsilon_0 V}}\hat{a}^\dagger, \tag{2.58}$$

which eventually gives

$$\hat{a}_{\mathbf{k},\lambda} = \frac{1}{\sqrt{2\hbar\omega_k}}(\omega_k\hat{q}_{\mathbf{k},\lambda} + \mathrm{i}\hat{p}_{\mathbf{k},\lambda}), \tag{2.59}$$

$$\hat{a}^\dagger_{\mathbf{k},\lambda} = \frac{1}{\sqrt{2\hbar\omega_k}}(\omega_k\hat{q}_{\mathbf{k},\lambda} - \mathrm{i}\hat{p}_{\mathbf{k},\lambda}). \tag{2.60}$$

The operators $\hat{a}$ and $\hat{a}^\dagger$ satisfy the following commutation relations

$$[\hat{a}_{\mathbf{k},\lambda}, \hat{a}_{\mathbf{k}',\lambda'}] = 0,\ \left[\hat{a}^\dagger_{\mathbf{k},\lambda}, \hat{a}^\dagger_{\mathbf{k}',\lambda'}\right] = 0,\ \left[\hat{a}_{\mathbf{k},\lambda}, \hat{a}^\dagger_{\mathbf{k}',\lambda'}\right] = \delta_{\mathbf{k}\mathbf{k}'}\delta_{\lambda\lambda'}. \tag{2.61}$$

Using this, the corresponding energy of the field, which is now identified as the Hamiltonian operator, simply becomes

$$\hat{H} = \sum_{\mathbf{k},\lambda}\hbar\omega_k\left(\hat{a}^\dagger_{\mathbf{k},\lambda}\hat{a}_{\mathbf{k},\lambda} + \frac{1}{2}\right), \tag{2.62}$$

For a single mode with creation and annihilation operators $\hat{a}$ and $\hat{a}^\dagger$ respectively and frequency ω, it can be written as

$$\hat{H} = \hbar\omega\left(\hat{a}^\dagger\hat{a} + \frac{1}{2}\right) = \hbar\omega\left(\hat{n} + \frac{1}{2}\right), \tag{2.63}$$

where $\hat{n} = \hat{a}^\dagger\hat{a}$ is the number operator. The fock state $|n\rangle$ represents the eigen state of this Hamiltonian with energy $n\hbar\omega$ corresponding to n photons and given by

$$|n\rangle = \frac{\hat{a}^{\dagger n}}{\sqrt{n!}}|0\rangle, \tag{2.64}$$

Finally, the electric field and the magnetic field operators resulting from the quantization can be written using Eqs. (2.2) and (2.3) as

$$\hat{\mathbf{E}}(\mathbf{r},t) = \mathrm{i}\sum_{\mathbf{k},\lambda}\hat{\mathbf{e}}_{\mathbf{k},\lambda}\sqrt{\frac{\hbar\omega_k}{2\epsilon_0 V}}\left(\hat{a}_{\mathbf{k},\lambda}e^{\mathrm{i}(k\cdot r-\omega_k t)} - \hat{a}^\dagger_{\mathbf{k},\lambda}e^{-\mathrm{i}(k\cdot r-\omega_k t)}\right), \tag{2.65}$$

$$\hat{\mathbf{B}}(\mathbf{r},t) = \frac{\mathrm{i}}{c}\sum_{\mathbf{k},\lambda}\left(\hat{\mathbf{k}}\times\hat{\mathbf{e}}_{\mathbf{k},\lambda}\right)\sqrt{\frac{\hbar\omega_k}{2\epsilon_0 V}}\left(\hat{a}_{\mathbf{k},\lambda}e^{\mathrm{i}(k\cdot r-\omega_k t)} - \hat{a}^\dagger_{\mathbf{k},\lambda}e^{-\mathrm{i}(k\cdot r-\omega_k t)}\right). \tag{2.66}$$

Note that the operators $\hat{a}_{\mathbf{k},\lambda}$ and $\hat{a}^{\dagger}_{\mathbf{k},\lambda}$ used to describe the electromagnetic field in Eqs. (2.65) and (2.66) are in the Heisenberg picture at time $t = 0$. Further, the electric field in Eq. (2.65) can be written as [98, 91]

$$\hat{\mathbf{E}}(\mathbf{r},t) = \mathrm{i}\sum_{\mathbf{k},\lambda}\hat{\mathbf{e}}_{\mathbf{k},\lambda}\sqrt{\frac{\hbar\omega_k}{2\epsilon_0 V}}\Big(\hat{a}_{\mathbf{k},\lambda}(t)e^{\mathrm{i}k\cdot r} - \hat{a}^{\dagger}_{\mathbf{k},\lambda}(t)e^{-\mathrm{i}k\cdot r}\Big), \tag{2.67}$$

where $\hat{a}_{\mathbf{k},\lambda}(t)$ and $\hat{a}^{\dagger}_{\mathbf{k},\lambda}(t)$ now represent the time-dependent annihilation and creation operators, which are given by

$$\hat{a}_{\mathbf{k},\lambda}(t) = \hat{a}_{\mathbf{k},\lambda}(0)e^{-\mathrm{i}\omega_k t}, \tag{2.68}$$

$$\hat{a}^{\dagger}_{\mathbf{k},\lambda}(t) = \hat{a}^{\dagger}_{\mathbf{k},\lambda}(0)e^{\mathrm{i}\omega_k t}. \tag{2.69}$$

The electric field operator for a single mode field polarized in a particular direction $\hat{\mathbf{e}}$ can be written as

$$\hat{\mathbf{E}}(\mathbf{r},t) = \mathrm{i}\sqrt{\frac{\hbar\omega_k}{2\epsilon_0 V}}\big(\hat{a}e^{\mathrm{i}(k\cdot r-\omega_k t)} - \hat{a}^{\dagger}e^{-\mathrm{i}(k\cdot r-\omega_k t)}\big)\hat{\mathbf{e}}. \tag{2.70}$$

The single mode electric field under the dipole approximation reads

$$\begin{aligned}\hat{\mathbf{E}}(\mathbf{r},t) &= \mathrm{i}\sqrt{\frac{\hbar\omega_k}{2\epsilon_0 V}}\big(\hat{a}e^{-\mathrm{i}\omega_k t} - \hat{a}^{\dagger}e^{\mathrm{i}\omega_k t}\big)\hat{\mathbf{e}},\\ &= \mathrm{i}\sqrt{\frac{\hbar\omega_k}{2\epsilon_0 V}}\big(\hat{a}(t) - \hat{a}^{\dagger}(t)\big)\hat{\mathbf{e}}.\end{aligned} \tag{2.71}$$

The corresponding Hamiltonian used to describe the interaction of a two-level atom with the single mode quantized field will now be given by $\hat{\mathbf{d}}\cdot\hat{\mathbf{E}}(\mathbf{r},t)$, where the electric field is now a quantum mechanical operator given by Eq. (2.71). This is often used to describe the interaction of an atom with single mode cavity field and will be used in the next chapter to describe the atom-cavity interactions.

Chapter 3

Atom-cavity interactions

In the previous chapter, we discussed the dynamics of the interaction of atoms with an external electromagnetic field. In this chapter, we discuss the interaction of a single atom with a quantized field mode, i.e., a fully quantum mechanical description of atom-field interaction. However, achieving the interaction between a single atom and the electric field in free space is not possible. Therefore, the single atom is placed in an optical cavity consisting of two mirrors with high reflectivity, as shown in Fig. 3.1. It allows light to bounce to and fro multiple times before it leaves the cavity. The coupling of an atom to a cavity has two significant advantages: (a) It allows for an efficient coupling between the atom and the quantized field mode. (b) By choosing the atom-cavity parameters properly, one can modify the rate of decay of the atom into the cavity mode, which results in the pre-dominant emission of the photon into a well-defined cavity mode.

We start with discussing a simple model of a two-level atom in an optical cavity with perfect mirrors interacting with a single-mode cavity field. It is also known as the Jaynes-Cummings model [99]. We also discuss the effects of cavity losses and the finite decay rate of the atom on the dynamics of the atom-cavity system. We then proceed to discuss the standard input-output formalism [78], which is used to study the effect on the input quantum field upon its interaction with the atom-cavity system. This can be used to obtain the output field outside the cavity in terms of the input field.

3.1 Interaction of an atom with single mode cavity field: Jaynes-Cummings model

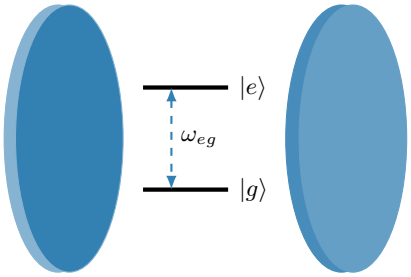

Figure 3.1: Two-level atom interacting with cavity.

In this section, we discuss the Jaynes-Cummings model which describes the quantum mechanical interaction between a two-level atom with a single-mode radiation of quantized electromagnetic field inside a cavity. We consider the ground and excited states of a two-level atom as $|g\rangle$ and $|e\rangle$ respectively. The Hamiltonian of a two-level atom interacting with the single-mode cavity field is given by the sum of three contributions, the atom part, the field part and the interaction between the atom and the single mode electric field [100, 91]

$$\begin{aligned} \hat{H} &= \hat{H}_C + \hat{H}_A + \hat{H}_I \\ &= \hbar\omega_c \hat{a}^\dagger \hat{a} + \hbar\omega_{eg} |e\rangle\langle e| - \hat{\mathbf{d}} \cdot \hat{\mathbf{E}}. \end{aligned} \tag{3.1}$$

Here, we assume that the ground state energy of the two-level atom is 0 and the energy of the excited state is $\hbar\omega_{eg}$ and $\hat{\mathbf{E}}$ represents the single mode cavity field operator, which can be written in the Schrodinger picture as [91]

$$\hat{\mathbf{E}} = \sqrt{\frac{\hbar\omega_c}{2\epsilon_0 V}}(\hat{a} + \hat{a}^\dagger)\hat{\mathbf{e}}, \tag{3.2}$$

where ω_c and V are the cavity frequency and the cavity mode volume, respectively. Substituting $\hat{\mathbf{E}}$ in Eq. (3.1), the Hamiltonian can be written as

$$\begin{aligned} \hat{H} &= \hbar\omega_c \hat{a}^\dagger \hat{a} + \hbar\omega_{eg} |e\rangle\langle e| - \hbar g\big(|e\rangle\langle g| \hat{a} + |e\rangle\langle g| \hat{a}^\dagger + |g\rangle\langle e| \hat{a} + |g\rangle\langle e| \hat{a}^\dagger\big), \\ &= \hbar\omega_c \hat{a}^\dagger \hat{a} + \hbar\omega_{eg}\sigma_{ee} - \hbar g\big(\sigma_{eg}\hat{a} + \sigma_{eg}\hat{a}^\dagger + \sigma_{ge}\hat{a} + \sigma_{ge}\hat{a}^\dagger\big), \\ &= H_0 + H_I, \end{aligned} \tag{3.3}$$

where $\hat{H}_0$ corresponds to the free Hamiltonian part for the cavity and atom, while H_I denotes the interaction between the atom and the cavity mode. $\sigma_{ij} = |i\rangle\langle j|$, and $g = \frac{d_{eg}}{\hbar}\sqrt{\frac{\hbar\omega_c}{2\epsilon_0 V}}$ is the coupling constant describing the strength of the coupling between the atom and cavity mode. V is the mode volume of the cavity and $d_{eg} = \langle e|\hat{d}|g\rangle$ is the transition dipole matrix element between the atomic states $|e\rangle$ and $|g\rangle$.

We can transform the above Hamiltonian to the interaction picture with respect to H_0, in which, the operators simply evolve in time according to the free evolution[1]

$$\begin{aligned} H_{\text{int}} &= e^{\mathrm{i}H_0 t/\hbar} H_I e^{-\mathrm{i}H_0 t/\hbar} \\ &= -\hbar g\big(\sigma_{eg}\hat{a}e^{\mathrm{i}(\omega_{eg}-\omega_c)t} + \sigma_{eg}\hat{a}^\dagger e^{\mathrm{i}(\omega_{eg}+\omega_c)t} + \sigma_{ge}\hat{a}e^{-\mathrm{i}(\omega_{eg}+\omega_c)t} + \sigma_{ge}\hat{a}^\dagger e^{-\mathrm{i}(\omega_{eg}-\omega_c)t}\big). \end{aligned} \tag{3.4}$$

This clearly shows that the terms $\sigma_{eg}\hat{a}$ and $\sigma_{ge}\hat{a}^\dagger$ exhibit time dependence $\propto e^{\mathrm{i}(\omega_{eg}-\omega_c)t}$ and $e^{-\mathrm{i}(\omega_{eg}-\omega_c)t}$, respectively. On the other hand, the terms $\sigma_{eg}\hat{a}^\dagger$ and $\sigma_{ge}\hat{a}$ evolve as $e^{\mathrm{i}(\omega_{eg}+\omega_c)t}$ and $e^{-\mathrm{i}(\omega_{eg}+\omega_c)t}$, respectively. For $\omega_c \sim \omega_{eg}$, the last two terms oscillate rapidly as compared to the first two terms; thus, these fast rotating terms are dropped under the rotating wave approximation (RWA) [93]. The Hamiltonian under RWA can be written as

$$H_{JC} = \hbar\omega_c\hat{a}^\dagger\hat{a} + \hbar\omega_{eg}\sigma_{ee} - \hbar g\big(\sigma_{eg}\hat{a} + \sigma_{ge}\hat{a}^\dagger\big), \tag{3.5}$$

which is known as the Jaynes-Cummings Hamiltonian [99, 100].

We further note that the JC Hamiltonian conserves the total energy in the system as $\big[(\sigma_{ee} + \hat{a}^\dagger\hat{a}), H\big] = 0$. The interaction between the atom and field mode indicates a reversible transfer of a quantum of excitation, i.e., a single photon between the atom and the single-mode cavity field. The atom excites to the state $|e\rangle$ after absorbing a single photon (corresponds to the term $\sigma_{eg}\hat{a}$) or the single atom de-excites to the ground state by emitting a photon into the cavity field (corresponds to the term $\sigma_{ge}\hat{a}^\dagger$).

Thus, we can choose the basis to be the product states $\{|g,n\rangle, |e,n-1\rangle\}$ in the

[1]The time dependence for the free evolution of the operator $\hat{a}$ can also be obtained directly from the expression of $\hat{\mathbf{E}}$ in the Heisenberg picture using Eq. (2.71), where $\hat{a}(t) = \hat{a}(0)e^{-\mathrm{i}\omega_c t}$. Similarly, the free evolution of atomic operator is given by $\sigma_{eg}(t) = \sigma_{eg}(0)e^{\mathrm{i}\omega_{eg}t}$.

Hilbert space of atom and the cavity field, where

$$|g,n\rangle \equiv |g\rangle \otimes |n\rangle\,, \quad |e,n-1\rangle \equiv |g\rangle \otimes |n-1\rangle \tag{3.6}$$

are the product states in the atom and field basis.

In order to solve the dynamics of the atom-cavity system, we write the JC Hamiltonian in Eq. (3.5) in the interaction picture taking $H_0 = \hbar\omega_c \hat{a}^\dagger \hat{a} + \hbar\omega_c \,|e\rangle\langle e|$, which is given by

$$\begin{aligned} H' &= e^{\mathrm{i}H_0 t/\hbar} H_I e^{-\mathrm{i}H_0 t/\hbar} \\ &= \hbar\Delta_{ac}\,|e\rangle\langle e| - \hbar g\big(\sigma_{eg}\hat{a} + \sigma_{ge}\hat{a}^\dagger\big), \end{aligned} \tag{3.7}$$

where $\Delta_{ac} = \omega_{eg} - \omega_c$ is the detuning between the atomic transition and the cavity frequency.

The general state in the joint atom-cavity basis $\{|g,n\rangle\,, |e,n-1\rangle\}$ can be simply written as

$$|\psi(t)\rangle = C_1(t)\,|g,n\rangle + C_2(t)\,|e,n-1\rangle\,. \tag{3.8}$$

The Schrödinger equation for the state $|\psi(t)\rangle$ considering the JC Hamiltonian in Eq. (3.7) gives

$$\mathrm{i}\frac{\mathrm{d}C_1}{\mathrm{d}t} = -g\sqrt{n}C_2, \tag{3.9}$$

$$\mathrm{i}\frac{\mathrm{d}C_2}{\mathrm{d}t} = -g\sqrt{n}C_1 + \Delta_{ac}C_2. \tag{3.10}$$

Solving above equations with the initial condition $C_1(0) = 1$ i.e., taking $|g,n\rangle$ as the initial state gives

$$C_1(t) = e^{-\frac{\mathrm{i}\Delta_{ac}t}{2}}\left[\cos\left(\frac{\Omega_n t}{2}\right) + \frac{\mathrm{i}\Delta_{ac}}{\Omega_n}\sin\left(\frac{\Omega_n t}{2}\right)\right], \tag{3.11}$$

$$C_2(t) = \frac{\mathrm{i}2g\sqrt{n}}{\Omega_n} e^{-\frac{\mathrm{i}\Delta_{ac}t}{2}} \sin\left(\frac{\Omega_n t}{2}\right), \tag{3.12}$$

where $\Omega_n = \sqrt{\Delta_{ac}^2 + 4g^2 n}$ is called the n-photon Rabi-frequency.

For the case when the cavity is in resonance with the atom i.e., $\Delta_{ac} = 0$, $\Omega_n = 2g\sqrt{n}$ which represents n-photon Rabi frequency on resonance. The probability of obtaining state $|e,n-1\rangle$ is

$$P_{e,n-1}(\Delta_{ac}=0) = |C_2|^2 = \sin^2(2g\sqrt{n}), \tag{3.13}$$

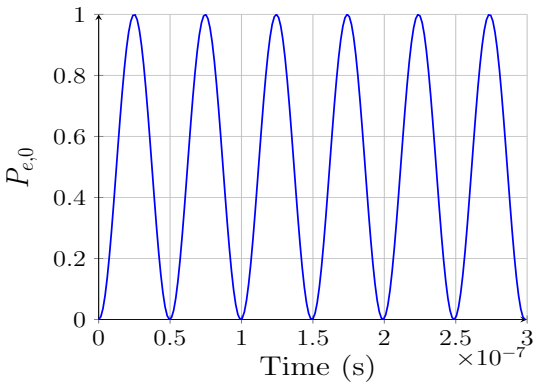

Figure 3.2: Rabi oscillations in JC model. The initial state of the system is $|g, n\rangle$, which represents atom in the ground state and the cavity field containing n photons.

which clearly shows that the system undergoes Rabi oscillations between the states $|g, n\rangle$ and $|e, n-1\rangle$ with the frequency $2g\sqrt{n}$. Fig. 3.2 shows the Rabi oscillations for the atom cavity system for $\Delta_{ac} = 0$.

Rabi oscillations are observed even when we start with the atom in an excited state with no photon in the cavity ($|e, 0\rangle$). These are called the vacuum Rabi oscillations, which occur with the vacuum Rabi frequency $2g$, which shows the cycle of emission of a photon by the atom in the excited state into the cavity mode and then re-absorption of the photon [91]. Such re-absorption of photon is not possible in the spontaneous decay of an atom in free space, where the photon can emit in infinite free space modes.

3.1.1 Dressed state picture

One can obtain the stationary states of the atom-cavity system, which gives better understanding of the atom-cavity interaction. For this, we write the JC Hamiltonian in the atom-cavity basis $\{|g, n\rangle, |e, n-1\rangle\}$ which reads

$$H_n = \hbar\Delta_{ac} |e, n-1\rangle\langle e, n-1| - \hbar g\sqrt{n}(|g, n\rangle\langle e, n-1| + |e, n-1\rangle\langle g, n|), \tag{3.14}$$

which can be written in the matrix form as

$$\begin{bmatrix} 0 & -\hbar g\sqrt{n} \\ -\hbar g\sqrt{n} & \hbar\Delta_{ac} \end{bmatrix}. \tag{3.15}$$

The eigenvalues of the above matrix are given by

$$E_{\pm}^{N} = \frac{\hbar}{2}\Big(\Delta_{ac} \pm \sqrt{\Delta_{ac}^{2} + 4g^{2}n}\Big). \tag{3.16}$$

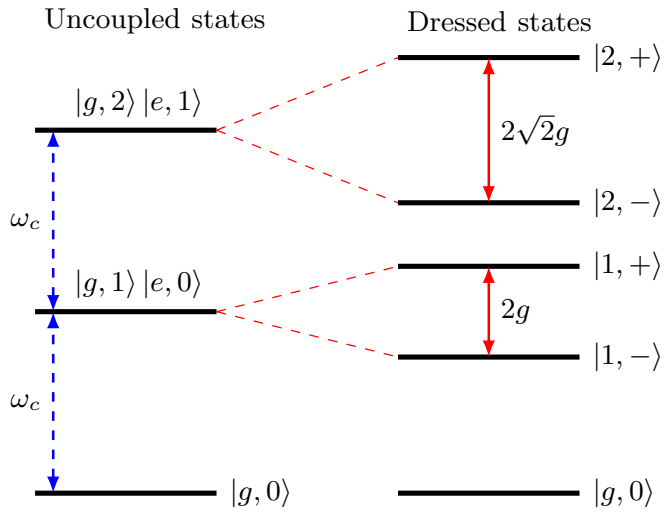

Figure 3.3: Jaynes Cummings anharmonic ladder structure.

We consider the simplest case when the cavity is in resonance with the atomic transition frequency, $\Delta_{ac} = 0$ so that the eigenvalues simply become $E_{\pm}^{N} = \pm\hbar g\sqrt{n}$ and the difference between the two eigenvalues is $E_{+}^{N} - E_{-}^{N} = \hbar(2g\sqrt{n}) \equiv \hbar\Omega_R$. The eigenvectors for this case will be

$$|N,\pm\rangle = \frac{|e,n-1\rangle \pm |g,n\rangle}{\sqrt{2}}. \tag{3.17}$$

which are the linear superposition of the basis states $\{|g,n\rangle, |e,n-1\rangle\}$. Thus, for zero detuning between the atom and the cavity, the eigenstates are $|N,\pm\rangle$ separated by $2g\sqrt{n}$. The eigenstates $|N,\pm\rangle$ are also known as the dressed states, and the splitting between these dressed states increases with the increase in the photon number n, which ultimately yields a non-linear energy spectrum. Fig. 3.3 shows the anharmonic ladder structure of the JC model for zero atom-cavity detuning. This non-linearity in the JC model has been demonstrated and used in engineering quantum states of light, atom-photon gates, and photon blockade [101, 18, 19].

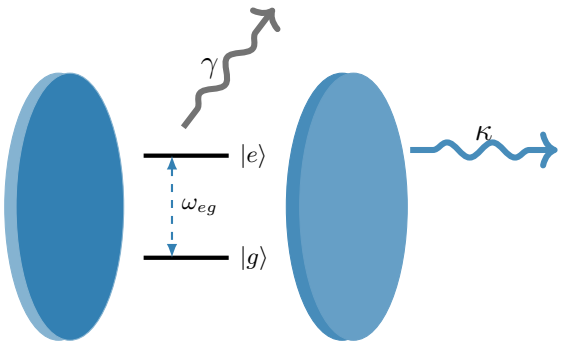

Figure 3.4: Atom-cavity system with atomic decay rate γ and cavity decay rate κ .

3.2 Atom-cavity system with damping

The JC model discussed above is for an ideal atom-cavity system where we have not considered any loss. However, the actual atom-cavity setup is an open quantum system coupled to the environment. There are two prominent loss channels. The first one is due to the spontaneous decay rate of the atom with a rate γ, which results in the emission of photon into the free space modes, while the second damping channel is due to the finite decay rate of the cavity mode through the cavity mirror at a rate κ as shown in Fig. 3.4. Due to these decay channels, the dynamics is no longer unitary. In order to study the dynamics of the damped atom-cavity system, including these decay channels, we use the Lindblad Master equation, which gives the evolution of the density matrix ρ of the system with the Hamiltonian H_S interacting with the environment and reads [95]

$$\frac{\mathrm{d}\rho}{\mathrm{d}t} = -\frac{\mathrm{i}}{\hbar}[H_S, \rho] + \left[\sum_{i=1}^{2} L_i \rho L_i^\dagger - \frac{1}{2} L_i^\dagger L_i \rho - \frac{1}{2} \rho L_i^\dagger L_i\right], \tag{3.18}$$

where $L_1 = \sqrt{\gamma}\sigma_{ge}$ and $L_2 = \sqrt{\kappa}\hat{a}$ are the Lindblad jump operators corresponding to the atomic and cavity decay with decay rates γ and κ, respectively. Substituting L_1 and L_2 gives

$$\frac{d\rho}{dt} = -\frac{\mathrm{i}}{\hbar}[H_S, \rho] - \frac{\gamma}{2}[2\sigma_{ge}\rho\sigma_{eg} - \rho\sigma_{ee} - \sigma_{ee}\rho] - \frac{\kappa}{2}[2\hat{a}\rho\hat{a}^\dagger - \rho\hat{a}^\dagger\hat{a} - \hat{a}^\dagger\hat{a}\rho]. \tag{3.19}$$

Solving this Master equation gives the complete evolution of the atom-cavity system. We use QuTiP software [102] in order to solve the atom-cavity dynamics

with H_S given in Eq. (3.7) for given parameters (g, κ, γ). Depending on the value of the parameters (g, κ, γ), we can classify the atom-cavity coupling in the two important regimes: the strong coupling regime and the bad cavity regime.

3.2.1 Strong coupling regime

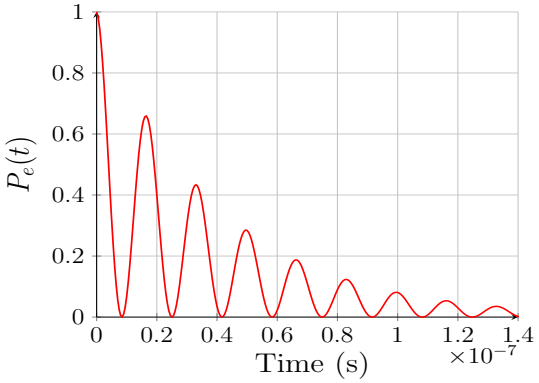

Figure 3.5: Population of atom in excited state as a function of time in case of strong coupling regime with atom cavity parameters $(g, \kappa, \gamma) = 2\pi \times (30, 5, 3)$ MHz.

In the strong coupling regime, the atom-cavity coupling g is highest, which means that the vacuum Rabi frequency is much greater than the decay rate of the cavity mode and the atom $g \gg \kappa, \gamma$ or $C = g^2/\kappa\gamma \gg 1$ where C is defined as the cooperativity parameter [20]. In the strong coupling regime, the system shows damped Rabi oscillations. Fig. 3.5 shows the evolution of the atomic population in the excited state when the system starts with an atom in the excited state with no photon present in the cavity, i.e., $|e, 0\rangle$. This is obtained by solving the master Eq. 3.19 numerically, which shows the reversible exchange of the photon between the atom and the cavity in the form of damped vacuum Rabi oscillations before it leaks out of the cavity. In this case, the atom-cavity parameters are taken to be $(g, \kappa, \gamma) = 2\pi \times (30, 5, 3)$ MHz and satisfy $g \gg (\kappa, \gamma)$.

3.2.2 Bad cavity regime

Contrary to the strong coupling regime, in the bad cavity regime, the cavity decay rate κ is the highest, and $\kappa \gg g^2/\kappa \gg \gamma$ such that $C = g^2/\kappa\gamma$ is still greater than 1. The vacuum Rabi oscillations are not possible in this regime, since the system is overdamped, and the photon emitted by the atom leaks out of the cavity at rate κ before it can be re-absorbed by the atom again. However, due to the atom-cavity coupling, the density of the photonic modes is changed, and the atomic decay rate is enhanced in the cavity mode over the free space decay rate by a factor of g^2/κ so that the effective decay rate into the cavity becomes $\Gamma_c = \gamma + g^2/\kappa \sim g^2/\kappa$ [20].[2] This increase in the atomic decay rate into the cavity mode is well known as the 'Purcell effect'.

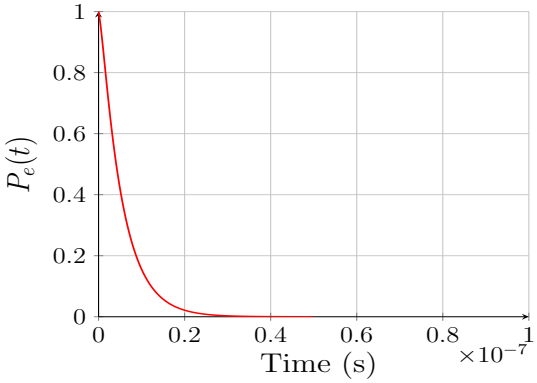

Figure 3.6: Population in the excited state as a function of time in case of bad cavity regime with atom cavity parameters $(g, \kappa, \gamma) = 2\pi \times (10, 90, 3)$ MHz .

Fig. 3.6 shows the atomic population in the excited state of an atom as a function of time, with the initial state of the atom-cavity system being $|e, 0\rangle$. The atom-cavity parameters, in this case are $(g, \kappa, \gamma) = 2\pi \times (10, 90, 3)$ MHz. As expected, there are no Rabi oscillations as the system is overdamped, and the population in the excited state rapidly decays to zero.

The JC model explains the dynamics of the atom-cavity interactions. However, it is limited to the case where we deal with the photons present inside the cavity. Typically, we deal with the atom-cavity systems, which are driven through one of

[2]The Purcell enhancement factor for finite atom-cavity detuning Δ_{ac} is $\frac{g^2\kappa}{\kappa^2 + \Delta_{ac}^2}$ which shows that the enhancement of decay rate into cavity mode is maximum on resonance.

the cavity mirrors by an input field with a specific pulse shape. In the next section, we discuss the input-output theory, which can be used to obtain the response of an atom-cavity system to an input quantum field that drives the cavity mode [20].

3.3 Input-Output formalism (Heisenberg-Langevin approach)

In this section, we study the relationship between the input and output field after interaction with a local quantum system, which is often helpful and a convenient tool to describe the interaction of an input field with a local quantum system. The framework of input-output theory allows one to calculate the response of the atom-cavity systems to the input field. It can be used to obtain the output field in terms of the driven input field upon interaction with the system [78].

We consider a system interacting with a heat bath which can be described by the following Hamiltonian [78]

$$H = H_S + H_B + H_I, \tag{3.20}$$

where H_S is the system Hamiltonian, H_B is the Hamiltonan for the bath which can be described by the bosonic annihilation field mode operator $b(\omega)$

$$H_B = \int_{-\infty}^{\infty} d\omega \hbar\omega \hat{b}^\dagger(\omega)\hat{b}(\omega), \tag{3.21}$$

and the bath operators $\hat{b}(\omega)$ and $\hat{b}^\dagger(\omega)$ satisfies the commutation relation $\left[\hat{b}(\omega), \hat{b}^\dagger(\omega')\right] = \delta(\omega - \omega')$. The term H_I describes the interaction between the system and the bath given by [78]

$$H_I = \mathrm{i}\hbar \int_{-\infty}^{\infty} d\omega \kappa(\omega)[\hat{b}^\dagger(\omega)\hat{c} - \hat{c}^\dagger\hat{b}(\omega)], \tag{3.22}$$

where $\hat{c}$ is one of the system operators (which simply becomes the intracavity field operator if we consider the localized system as a cavity) and $\kappa(\omega)$ is the strength of the coupling between the system and the bath. Note that the frequency limits in the Hamiltonian should be 0 to ∞. However, for optical systems with high frequencies,

one can shift the integration to a frequency Ω, which is the characteristic frequency of the system. For e.g., for a cavity, this Ω becomes the resonance frequency of the cavity. Thus, we change the limits to $(-\Omega, \infty)$. Since Ω is very large, it is approximated to $-\infty$.[3] Next, we write the Heisenberg equations of motion for a general system operator $\hat{a}$ and the bath operator using Eqs. (3.21) and (3.22), which reads [78]

$$\dot{\hat{a}} = \frac{1}{\mathrm{i}\hbar}[a, H_S] + \int d\omega\ \kappa(\omega)\Big[\hat{b}^\dagger(\omega)[\hat{a}, \hat{c}] - \big[\hat{a}, \hat{c}^\dagger\big]\hat{b}(\omega)\Big], \tag{3.23}$$

$$\dot{\hat{b}} = -\,\mathrm{i}\omega\hat{b}(\omega) + \kappa(\omega)\hat{c}. \tag{3.24}$$

The general solution of Eq. (3.24) can be written as

$$\hat{b}(\omega) = e^{-\mathrm{i}\omega(t-t_0)}\hat{b}_0(\omega) + \kappa(\omega)\int_{t_0}^{t} e^{-\mathrm{i}\omega(t-t')}\hat{c}(t')dt', \tag{3.25}$$

where $\hat{b}_0(\omega)$ is $\hat{b}(\omega)$ at initial time $t = t_0$ and is considered as the input field mode. Using this in Eq. (3.23) gives

$$\dot{\hat{a}} = \frac{1}{\mathrm{i}\hbar}[\hat{a}, H_S] + \int\ \kappa(\omega)\Big[e^{\mathrm{i}\omega(t-t_0)}\hat{b}_0^\dagger(\omega)[\hat{a}, \hat{c}] - e^{-\mathrm{i}\omega(t-t_0)}\big[\hat{a}, \hat{c}^\dagger\big]\hat{b}_0(\omega)\Big]d\omega \tag{3.26}$$

$$+ \int d\omega[\kappa(\omega)]^2\ \int_{t_0}^{t}\Big[e^{\mathrm{i}\omega(t-t')}c^\dagger(t')(\omega)[\hat{a}, \hat{c}] - e^{-\mathrm{i}\omega(t-t')}\big[\hat{a}, \hat{c}^\dagger\big]\hat{b}_0(\omega)\Big]. \tag{3.27}$$

Further, it is assumed that the coupling strength $\kappa(\omega)$ is constant and $\kappa(\omega) = \sqrt{\gamma/2\pi}$, which is called the *First Markov approximation*. This approximation holds good for weak system-bath coupling ($\kappa(\omega) \ll \Omega$)) where $\kappa(\omega)$ is independent over a narrowband of frequencies around the characteristic frequency Ω. Now, an input field $\hat{b}_{\mathrm{in}}$ is defined as [78]

$$\hat{b}_{\mathrm{in}} = \frac{1}{\sqrt{2\pi}}\int e^{-\mathrm{i}\omega(t-t_0)}\hat{b}_0(\omega)d\omega, \tag{3.28}$$

which can be understood as the part of the field incident on the local system and follows the commutation relation

$$\Big[\hat{b}_{\mathrm{in}}(t), \hat{b}_{\mathrm{in}}^\dagger(t')\Big] = \delta(t - t'). \tag{3.29}$$

Using this, the quantum Langevin equation for any system operator $\hat{a}$ is given by [78]

$$\dot{\hat{a}} = \frac{1}{\mathrm{i}\hbar}[\hat{a}, H_S] - \big[\hat{a}, \hat{c}^\dagger\big]\Big(\frac{\gamma}{2}\hat{c} + \sqrt{\gamma}\hat{b}_{\mathrm{in}}(t)\Big) + \Big(\frac{\gamma}{2}\hat{c}^\dagger + \sqrt{\gamma}\hat{b}_{\mathrm{in}}^\dagger(t)\Big)[\hat{a}, \hat{c}], \tag{3.30}$$

[3] This is a good approximation since the field modes far away from Ω have negligible interaction with the system.

which clearly shows that the damping term depends only on the system operators evaluated at time t and not on the previous time, which follows from the *first Markov approximation.*

It is noted that Eq. (3.25) is written for time $t > t_0$. If we consider time $t_1 > t$, the solution corresponding to Eq. (3.24) becomes [78]

$$\hat{b}(\omega) = e^{-\mathrm{i}\omega(t-t_1)}\hat{b}_1(\omega) - \kappa(\omega)\int_t^{t_1} e^{-\mathrm{i}\omega(t-t')}\hat{c}(t')dt'. \tag{3.31}$$

with $\hat{b}_1(\omega)$ being evaluated at time t_1 ($t_1 > t$). Using this gives us the time reversed Langevin equation, which reads

$$\dot{\hat{a}} = \frac{1}{\mathrm{i}\hbar}[\hat{a}, H_S] - [\hat{a}, \hat{c}^\dagger]\left(-\frac{\gamma}{2}\hat{c} + \sqrt{\gamma}\hat{b}_{\mathrm{out}}(t)\right) + \left(-\frac{\gamma}{2}\hat{c}^\dagger + \sqrt{\gamma}\hat{b}^\dagger_{\mathrm{out}}(t)\right)[\hat{a}, \hat{c}], \tag{3.32}$$

where the output field is defined as

$$\hat{b}_{\mathrm{out}} = \frac{1}{\sqrt{2\pi}}\int e^{-\mathrm{i}\omega(t-t')}\hat{b}_1(\omega)d\omega, \tag{3.33}$$

which can be interpreted as the output field scattered by the localized system due to its interaction with the input field. Furthermore, from Eqs. (3.25) and (3.31), it follows that

$$\int \hat{b}(\omega)d\omega = \hat{b}_{\mathrm{in}}(t) + \frac{\sqrt{\gamma}}{2}\hat{c}(t) = \hat{b}_{\mathrm{out}}(t) - \frac{\sqrt{\gamma}}{2}\hat{c}(t), \tag{3.34}$$

which finally gives the following standard input-output relation

$$\hat{b}_{\mathrm{out}}(t) - \hat{b}_{\mathrm{in}}(t) = \sqrt{\gamma}\hat{c}(t). \tag{3.35}$$

If we consider the input field to be a single photon state with temporal profile $f(t)$, such that $\int |f(t)|^2 dt = 1$, then the field creation operator for the input state is given by [103, 104]

$$\hat{B}^\dagger = \int dt f(t)\hat{b}^\dagger_{in}(t), \tag{3.36}$$

so that the input state is represented as

$$|1_f\rangle = \hat{B}^\dagger|0\rangle = \int dt f(t)\hat{b}^\dagger_{\mathrm{in}}(t)|0\rangle\,. \tag{3.37}$$

Similarly, for N photon state, the input state will be given by

$$|N_f\rangle = \frac{\hat{B}^{\dagger N}}{\sqrt{N!}}|0\rangle\,. \tag{3.38}$$

Similarly, for coherent state with amplitude $\alpha(t) = \alpha_0 f(t)$, the input state is given by

$$|\alpha\rangle_f = e^{(\alpha_0\hat{B}^\dagger - \alpha_0^*\hat{B})}|0\rangle\,. \tag{3.39}$$

Further, in this case $\langle\hat{b}_{\rm in}(t)\rangle = \alpha(t)$, so using Eq. (3.35) gives $\langle\hat{b}_{\rm out}(t)\rangle = \sqrt{\kappa}\,\langle\hat{c}(t)\rangle + \alpha(t)$.

Now we consider the system of interest to be a single cavity mode interacting with an external field, which leaks at a rate κ, the system operator $\hat{a}$ simply becomes the harmonic oscillator mode with $H_S = \hbar\omega_c\hat{a}^\dagger\hat{a}$ and the corresponding Langevin equation for the cavity mode reads

$$\dot{\hat{a}} = -\mathrm{i}\omega_c\hat{a} - \frac{\gamma}{2}\hat{a} - \sqrt{\kappa}\hat{a}_{\rm in}(t), \tag{3.40}$$

where $a_{\rm in}(t)$ represents the input quantum field . The standard input-output relation for the cavity in this case reads

$$\hat{a}_{\rm out}(t) - \hat{a}_{\rm in}(t) = \sqrt{\kappa}\hat{a}(t), \tag{3.41}$$

which relates the input, output, and the intra-cavity fields of the cavity. This is typically useful to calculate the output field from the cavity or atom-cavity systems that interact with an input quantum field, $\hat{a}_{\rm in}(t)$.

As another example, we now consider a system of a two-level atom interacting with a single cavity mode, as shown in Fig. 3.7. It will have two decay channels, one corresponding to the decay of the cavity mode at a rate κ, while the other is due to the spontaneous emission by the atom into the free space modes at a rate γ. The corresponding set of dynamical equations in accordance with the input-output theory for the atomic operator $\sigma_{ge} = |g\rangle\langle e|$, $\sigma_{gg} = |g\rangle\langle g|$ and the cavity mode

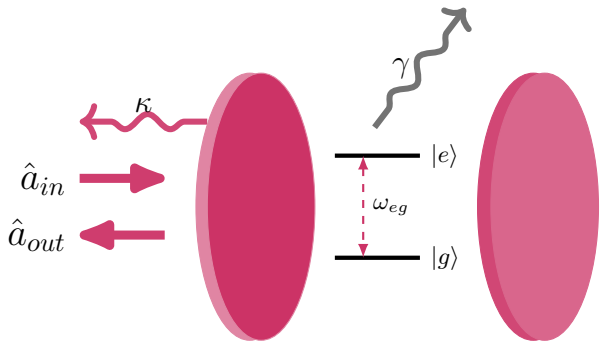

Figure 3.7: Atom-cavity system with atomic decay rate γ and cavity decay rate κ .

operator $\hat{a}$ using the Hamiltonian in Eq. (3.1) can be written as

$$\frac{\mathrm{d}\sigma_{ge}}{\mathrm{d}t} = -\Big(\mathrm{i}\Delta_a + \frac{\gamma}{2}\Big)\sigma_{ge} + \mathrm{i}g(2\sigma_{gg} - 1)\hat{a}, \tag{3.42}$$

$$\frac{\mathrm{d}\sigma_{gg}}{\mathrm{d}t} = -\mathrm{i}g\big(\sigma_{eg}\hat{a} - \sigma_{ge}\hat{a}^\dagger\big) + \gamma\sigma_{ee}, \tag{3.43}$$

$$\frac{\mathrm{d}\hat{a}}{\mathrm{d}t} = -\Big(\mathrm{i}\Delta_c + \frac{\kappa}{2}\Big)\hat{a} + \mathrm{i}g^*\sigma_{ge} - \sqrt{\kappa}\hat{a}_{\mathrm{in}}, \tag{3.44}$$

where ω_L is the mean frequency of the input field, $\Delta_c = \omega_c - \omega_L$ and $\Delta = \omega_{eg} - \omega_L$ are the cavity and the atomic detunings from the input field, respectively. The above set of equations along with the input-output relation in Eq. (3.41) gives the complete dynamics of the atom-cavity system.

If the atomic excitation is negligible, i.e., $\sigma_{gg} \sim 1$ and the input photon pulse width in time is greater than the cavity decay rate, we can find the steady state solution for the atom-cavity system by putting $\frac{\mathrm{d}\sigma_{ge}}{\mathrm{d}t} = 0$ and $\frac{\mathrm{d}\hat{a}}{\mathrm{d}t} = 0$ which gives

$$-\Big(\mathrm{i}\Delta_a + \frac{\gamma}{2}\Big)\sigma_{ge} + \mathrm{i}g\hat{a} = 0, \tag{3.45}$$

$$-\Big(\mathrm{i}\Delta_c + \frac{\kappa}{2}\Big)\hat{a} + \mathrm{i}g^*\sigma_{ge} - \sqrt{\kappa}\hat{a}_{\mathrm{in}} = 0. \tag{3.46}$$

Solving these equations for $\hat{a}$, and using the input-output relation gives the analytical expression for the reflection coefficient of the cavity which is given by [20]

$$r = \frac{\hat{a}_{\mathrm{out}}}{\hat{a}_{in}} = \frac{|g|^2 + (\mathrm{i}\Delta_c - \kappa/2)(\mathrm{i}\Delta_a + \gamma/2)}{|g|^2 + (\mathrm{i}\Delta_c + \kappa/2)(\mathrm{i}\Delta_a + \gamma/2)}. \tag{3.47}$$

For the atom and cavity both on resonance with the input field, it simplifies to

$$r = \frac{\hat{a}_{\mathrm{out}}}{\hat{a}_{\mathrm{in}}} = \frac{|g|^2 - \kappa\gamma/4}{|g|^2 + \kappa\gamma/4}. \tag{3.48}$$

For an atom-cavity system with $|g|^2 \gg \kappa\gamma$, the reflection coefficient $r \sim 1$. On the contrary, if the atom is not coupled to the cavity, i.e., $g = 0$, then the reflection coefficient $r = -1$. Thus, there is a phase difference of π for the outgoing photon when the atom-cavity system is decoupled. This property has been used extensively to generate quantum gates between atoms and photons [105, 106, 69].

We will use the atom-cavity interactions and the input-output theory to discuss how a single atom coupled to an optical cavity can be used as an efficient quantum memory in chapter 6.

Chapter 4

Quantum memory using AFC and I-AFC

Photonic quantum information processing requires storage and retrieval of the photons in an efficient and controllable way. This is achieved by quantum memory, a device which can store and re-emit photons on demand. In a typical atomic ensemble-based quantum memory, a weak light pulse is absorbed as delocalized atomic excitation over all the atoms in the ensemble. This collective atomic excitation is then transferred to a long-lived spin state of the atoms using control pulses. In order to retrieve the photons from the atomic ensemble, a trigger pulse is used to transfer the excitation from the long-lived spin state to the excited state of the atom, which emits the photon at the desired time [12].

Some of the commonly used quantum memory protocols include electromagnetically induced transparency (EIT) [26, 27, 28, 29], controlled reversible inhomogeneous broadening (CRIB) [30, 31, 32, 33], gradient echo memory (GEM), [35, 36, 37], Raman memory [39, 41, 42], photon-echo using atomic frequency comb (AFC) [43, 44, 45, 46, 48] and intra-atomic frequency comb (I-AFC) [49, 50, 51]. In all these protocols, a photon is made to interact with an ensemble of atoms or atom-like systems, carefully tuned to maximize the absorption of the photons. A controlled sequence of pulses is used to switch on and off the interaction between the photon and the atomic ensemble to achieve controlled storage.

In this chapter, we introduce the quantum memory protocols based on atomic frequency comb (AFC) and intra-atomic frequency comb (I-AFC).

4.1 Quantum memory using atomic frequency comb (AFC)

The storage medium used for the quantum memory based on the atomic frequency comb (AFC) usually consists of rare earth ion doped crystal, which consists of an optical transition between the ground state $|g\rangle$ and the excited state $|e\rangle$. This transition has an inherent narrow homogeneous broadening at low temperatures ($<$ 4 K) with linewidth γ, which is in the range 0.1–100 kHz [43]. Further, due to doping of rare earth ions in the crystal, different ions experience different local environment giving rise to a large inhomogeneous broadening $\sim \Gamma(\sim$ GHz) such that $\Gamma \gg \gamma$ [43]. Pr^{3+} doped Y_2SiO_5 and Eu^{3+} doped Y_2SiO_5 are typically used rare earth ion doped crystals to achieve AFC [44, 46, 48].

The storage protocol using AFC includes spectral shaping of this large inhomogeneously broadened absorption profile into a series of equispaced narrow peaks of width γ with spacing Δ which ultimately gives a comb-like structure as shown in Fig. 4.1(a). This is achieved using frequency selective transfer of the population in the ground state to some auxiliary state with a long lifetime, which is also known as spectral hole burning. This process is repeated at different frequencies in order to achieve a periodic comb-like structure of the absorption profile in the frequency domain [44, 46, 48].

The single photon with spectral width γ_p gets stored as a single excitation delocalized over all the peaks in the system. The collective excited state of the system, after the absorption of a single photon in the AFC, can be described as [43]

$$|\Psi\rangle_e = \sum_{j=1}^{N} \left(c_j e^{i\delta_j t} |g_1 ... e_j ... g_N\rangle \right), \tag{4.1}$$

where N $\rightarrow$ total number of atoms $\delta_j \rightarrow$ detuning of the j-th atom with respect to the input field and c_j represent the corresponding absorption coefficient of the j-th

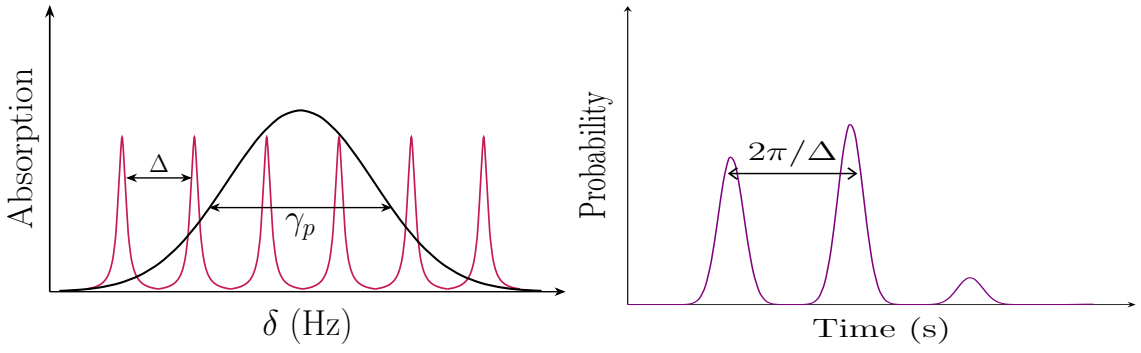

(a) (b)

Figure 4.1: (a) AFC with comb spacing Δ interacting with an input pulse of width γ_p, which spectrally covers the frequency comb. (b) Typical photon-echo using AFC after time a time delay of $2\pi/\Delta$.

atom.

From Eq. (4.1), we see that initially, at $t = 0$, all the components are in the same phase. However, the state $|\Psi\rangle_e$ rapidly dephases as the system evolves into a non-collective state due to different detunings for different atoms, which shows up as a phase factor of $e^{i\delta_j t}$ with each term in Eq. (4.1). However, considering the frequency comb structure as in Fig. 4.1(a), we can approximate $\delta_j \sim m_j\Delta$ for integer m_j and comb spacing Δ. The collective state then can be written as

$$|\Psi\rangle_e = \sum_{j=1}^{N} \left(c_j e^{im_j\Delta t} |g_1...e_j...g_N\rangle\right). \tag{4.2}$$

Thus, due to the periodicity of the frequency comb structure, all the components of $|\Psi\rangle_e$ become in phase again after integral multiples of time $2\pi/\Delta$, which results in the re-emission of the input photon in the forward direction known as photon-echo. Fig. 4.1(b) shows a typical photon-echo using AFC. Here, the first peak represents the amount of the input light which does not interact with the ensemble of atoms and passes as it is, while the second peak is the photon-echo which occurs due to the rephasing process as discussed above after time $2\pi/\Delta$. Similarly, the third peak represents the second photon-echo which occurs after time period of $4\pi/\Delta$. Since the first photon-echo is the prominent one, the amplitude of third and higher order photon-echoes is small. Further, the relative amplitude of the photon-echo

determines the efficiency of the quantum memory. However, as we will see in the upcoming section that this is limited to $\sim 54\%$.

This process gives a fixed storage time depending on the comb spacing Δ. However, to get control over the storage time and to achieve on-demand storage, the collective excitation in excited state $|e\rangle$ is ususally transferred to a long-lived spin state $|s\rangle$ by applying a control field before the echo-time $2\pi/\Delta$. After a time T_s, another counterpropagating control field is applied, which transfers back the excitation from $|s\rangle$ to $|e\rangle$. This finally results in the emission of the photon in the backward direction with a storage time of $2\pi/\Delta + T_s$ [43]. In the next section, we discuss the dynamics of storage using AFC and the efficiency of this protocol in the case of forward emission and the backward emission.

4.1.1 Dynamics of atomic frequency comb

The dynamics of light interacting with AFC-based ensemble is governed by the electric field and the atomic polarization. To describe the dynamics of light field interacting with an ensemble of atoms with ground state $|g\rangle$ and excited state $|e\rangle$, we define the atomic operator $\sigma_{ge}(z,t,\delta)$ as follows [43, 33]

$$\sigma_{ge}(z,t,\delta) = \frac{1}{N(\delta,z)} \sum_{i=1}^{N(\delta,z)} |g\rangle_i \langle e| \,, \tag{4.3}$$

where the sum is over all the atoms, $N(\delta,z) = n(\delta)dzd\delta/L$ which have detuning in range $(\delta - d\delta/2, \delta + d\delta/2)$ and position in range $(z - dz/2, z + dz/2)$. Here, $n(\delta)$ describes the spectral distribution of atoms such that $\int_{-\infty}^{\infty} n(\delta)d\delta = N_a$, where N_a is the total number of atoms. L is the length of the atomic ensemble. Further, we decompose the atomic coherence operator σ_{ge} into a forward and backward propagating mode given by [43, 33]

$$\sigma_{ge}(z,t,\delta) = \sigma_f(z,t,\delta)e^{\mathrm{i}\omega_0 z/c} + \sigma_b(z,t,\delta)e^{-\mathrm{i}\omega_0 z/c}, \tag{4.4}$$

where ω_0 is the mean frequency of the light field. Similarly, we can decompose the electric field also in the forward and backward propagating modes. The dynamical equations of motion for the forward and backward modes of the electric field and

the corresponding atomic polarization are given by (see Sec. 2.3) [43].

$$\frac{\partial}{\partial t}\sigma_f(z,t,\delta) = -\mathrm{i}\delta\sigma_f(z,t,\delta) + \mathrm{i}d_{eg}E_f(z,t), \tag{4.5}$$

$$\left(\frac{\partial}{\partial t} + c\frac{\partial}{\partial z}\right)E_f(z,t) = \mathrm{i}\tilde{\rho}\int_{-\infty}^{\infty} n(\delta)\sigma_f(z,t,\delta)d\delta, \tag{4.6}$$

$$\frac{\partial}{\partial t}\sigma_b(z,t,\delta) = -\mathrm{i}\delta\sigma_b(z,t,\delta) + \mathrm{i}d_{eg}E_b(z,t), \tag{4.7}$$

$$\left(\frac{\partial}{\partial t} - c\frac{\partial}{\partial z}\right)E_b(z,t) = \mathrm{i}\tilde{\rho}\int_{-\infty}^{\infty} n(\delta)\sigma_b(z,t,\delta)d\delta, \tag{4.8}$$

where d_{eg} is the transition dipole moment between the ground and excited state defined as $d_{eg} = \langle e|e\mathbf{r}|g\rangle$. $\tilde{\rho}$ is defined as $\tilde{\rho} = g_0^2 d_{eg}$, with $g_0 = \sqrt{\omega_0/(2\epsilon_0 V)}$, ω_0 is the transition frequency, and V is the quantization volume.

We assume that the spectral atomic distribution is comb shaped which is given in the frequency domain as [43]

$$n(\delta) \propto e^{\delta^2/2\Gamma^2} \sum_{n=-\infty}^{\infty} e^{(\delta - n\Delta)^2/2\gamma^2}, \tag{4.9}$$

where Δ represents the comb spacing, γ specifies the individual peak width, and Γ represents the overall bandwidth of the frequency comb. The Fourier transform of the above equation gives the spectral distribution in the time domain given by

$$\begin{aligned} n(t) = F[n(\delta)] &= \int_{-\infty}^{\infty} n(\delta)e^{-\mathrm{i}\delta t}d\delta, \\ &= F\left[e^{\delta^2/2\Gamma^2}\right] * F\left[\sum_{n=-\infty}^{\infty} e^{(\delta - n\Delta)^2/2\gamma^2}\right], \end{aligned} \tag{4.10}$$

where * represents the convolution of two functions and is defined as

$$g * h = \int_{-\infty}^{\infty} g(\tau)h(t-\tau)d\tau. \tag{4.11}$$

Using this, the final expression for $n(t)$ becomes

$$n(t) \propto \sum_{n=-\infty}^{n=\infty} e^{-\left(t - \frac{2\pi n}{\Delta}\right)^2 \frac{\Gamma^2}{2}} e^{-\left(\frac{2\pi n}{\Delta}\right)^2 \frac{\gamma^2}{2}}. \tag{4.12}$$

The interaction of AFC with the incoming light can be divided into two parts, the absorption process and the emission process.

4.1.1.1 Absorption process

The absorption process can be described by the forward mode Eqs. (4.5) and (4.6) which couple $\sigma_f(z,t,\delta)$ and $E_f(z,t)$. The formal solution of Eq. (4.5) reads

$$\sigma_f(z,t,\delta) = \mathrm{i}d_{eg}e^{-\mathrm{i}\delta t}\int_{-\infty}^{t} E_f(z,t')e^{\mathrm{i}\delta t'}dt', \tag{4.13}$$

where $\sigma_f(z,-\infty)=0$. Substituting it into Eq. (4.6), we get

$$\left(\frac{\partial}{\partial t}+c\frac{\partial}{\partial z}\right)E_f(z,t) = -d_{eg}\tilde{\rho}\int_{-\infty}^{t}\tilde{\eta}(t-t')E_f(z,t')dt'. \tag{4.14}$$

If τ is the temporal width of the input pulse, we consider the regime where $\tau \gg L/c$, with L being the length of the ensemble. Further, if the temporal width is less than the echo-time, i.e., $\tau \ll 2\pi/\Delta$, then only the central peak in $\tilde{n}(t)$ contributes such that [43]

$$\tilde{n}(t-t') \propto e^{-(t-t')^2\Gamma^2/2}. \tag{4.15}$$

In addition, we assume that the width of the whole spectral distribution Γ is much greater than the width of the input pulse in the frequency domain, i.e., $\Gamma \gg 1/\tau$. Thus, we can approximate $\tilde{n}(t-t')$ to be the Dirac delta which simplifies Eq. (4.14) to

$$\left(\frac{\partial}{\partial t}+c\frac{\partial}{\partial z}\right)E_f(z,t) = -\frac{d_{eg}\tilde{\rho}}{2}E_f(z,t). \tag{4.16}$$

Making the transformation $t' \to t - z/c$ further simplifies it to

$$\frac{\partial}{\partial z}E_f(z,t') = -\frac{\tilde{\alpha}}{2}E_f(z,t'), \tag{4.17}$$

where $\tilde{\alpha}$ is defined as the absorption coefficient. For $\tau \gg L/c$, we can replace t' with t which gives [43]

$$\frac{\partial}{\partial z}E_f(z,t) = -\frac{\tilde{\alpha}}{2}E_f(z,t). \tag{4.18}$$

The above equation has a simple solution given by

$$E_f(z,t) = e^{-\frac{\tilde{\alpha}z}{2}}E_f(0,t). \tag{4.19}$$

The effective absorption depth for the AFC protocol is defined as $\tilde{d} = \tilde{\alpha}L$. Hence, for a medium of length L, the forward mode field amplitude becomes

$$E_f(L,t) = e^{-\frac{\tilde{d}}{2}} E_f(0,t). \tag{4.20}$$

This describes the absorption process. In the next section, we discuss the re-emission of the input field.

4.1.1.2 Re-emission of input field

Re-emission in forward mode

The absorption of the field occurs from $t = -\infty$ to 0, while the emission of the field is considered between 0 and t. The corresponding field equation for the forward mode for $-\infty$ to t becomes [43]

$$\frac{\partial}{\partial z}E_f(z,t) = -\tilde{\alpha}\int_{-\infty}^{0} \tilde{n}(t-t')E_f(z,t')dt' - \tilde{\alpha}\int_{0}^{t} \tilde{n}(t-t')E_f(z,t')dt'. \tag{4.21}$$

Applying the same argument as in the case of absorption and considering $n(t-t') = \delta(t-t')$, it becomes

$$\frac{\partial}{\partial z}E_f(z,t) + \frac{\tilde{\alpha}}{2}E_f(z,t) = -\tilde{\alpha}\sum_{n=-\infty}^{\infty} E_f\left(z, t - \frac{2\pi n}{\Delta}\right) e^{-\left(\frac{2\pi n}{\Delta}\right)^2 \frac{\gamma^2}{2}}. \tag{4.22}$$

Note that, in the case of re-emission, there are peaks for $\eta(t-t')$ around $t - t' = 2\pi n/\Delta$ apart from the central peak. The solution of the above equation can be written as

$$\begin{aligned} E_f(z,t) &= -\tilde{\alpha}\sum_{n=-\infty}^{\infty} e^{-\left(\frac{2\pi n}{\Delta}\right)^2 \frac{\gamma^2}{2}} e^{\tilde{\alpha}z/2}\int_0^z E_f\left(z', t - \frac{2\pi n}{\Delta}\right) e^{-\tilde{\alpha}z'/2}dz', \\ &= -\tilde{\alpha}\sum_{n=-\infty}^{\infty} e^{-\left(\frac{2\pi n}{\Delta}\right)^2 \frac{\gamma^2}{2}} e^{-\tilde{\alpha}z/2} E_f\left(0, t - \frac{2\pi n}{\Delta}\right)\int_0^z dz'. \end{aligned} \tag{4.23}$$

The output at $z = L$ becomes

$$E_f(L,t) = -\tilde{\alpha}Le^{-\tilde{\alpha}L/2}\sum_{n=-\infty}^{\infty} e^{-\left(\frac{2\pi n}{\Delta}\right)^2 \frac{\gamma^2}{2}} E_f\left(0, t - \frac{2\pi n}{\Delta}\right). \tag{4.24}$$

Efficiency

The efficiency for the first photon-echo in AFC protocol is defined as the ratio of the intensity of output light obtained in the first echo to the total intensity of the input light and is given by [43]

$$\eta_f = \frac{\int_{\pi/\Delta}^{3\pi/\Delta} |E(z=L,t)|^2}{\int |E(z=0,t)|^2}. \tag{4.25}$$

Using Eq. (4.24), the efficiency in the forward emission for the first photon-echo becomes

$$\eta_f = (\tilde{\alpha}L)^2 e^{-\tilde{\alpha}L} e^{-\left(\frac{2\pi\gamma}{\Delta}\right)^2}. \tag{4.26}$$

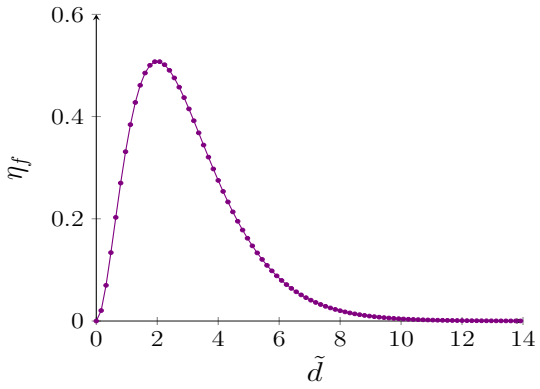

Figure 4.2: Forward mode efficiency as function of absorption depth $\tilde{d}$.

Fig. 4.2 shows the plot of the efficiency in the forward mode as a function of effective absorption depth, $\tilde{d} = \tilde{\alpha L}$ for comb finesse $F = \Delta/\gamma = 25$.

The maximum theoretical efficiency that can be achieved in the forward mode is $\sim 54\%$. This is because of the re-absorption of the photon-echo by the atoms present in the ensemble. However, if the re-emission of the input field can be forced in the backward direction, the optimized efficiency can reach $\sim 100\%$. In the next section, we discuss the dynamics of the re-emission in the backward mode.

4.1.1.3 Backward mode

The backward mode re-emission is used to obtain longer echo time and on-demand storage. In this process, a π pulse is used to transfer the excitation to a long-lived

state, and then after a time T, another π pulse is applied in a counterpropagating direction. This couples the atomic polarization to the backward propagating field mode, which eventually results in the photon-echo in the backward direction after a time $2\pi/\Delta + T$ [43].

The corresponding dynamical equation for the backward atomic polarization, in this case at $t = 0$ can be written as [43]

$$\sigma_b(z, 0, \delta) = \sigma_f(z, 0, \delta) = \int_{-\infty}^{0} E_f(z, 0) e^{\mathrm{i}\delta t'} dt', \tag{4.27}$$

where, it is assumed that $E_b(z, 0) = 0$. The solution of Eq. (4.7) can be written as

$$\sigma_b(z, t, \delta) = \mathrm{i} d_{eg} e^{-\mathrm{i}\delta t} \int_{0}^{t} E_b(z, t') e^{\mathrm{i}\delta t'} dt' + \sigma_b(z, 0). \tag{4.28}$$

Using Eq. (4.27), it becomes

$$\sigma_b(z, t, \delta) = \mathrm{i} d_{eg} e^{-\mathrm{i}\delta t} \left(\int_{0}^{t} E_b(z, t') e^{\mathrm{i}\delta t'} dt' + \int_{-\infty}^{0} E_f(z, 0) e^{\mathrm{i}\delta t'} dt' \right). \tag{4.29}$$

The corresponding field equation for the backward mode using Eq. (4.29) becomes

$$\left(\frac{\partial}{\partial t} - c \frac{\partial}{\partial z} \right) E_b(z, t) = -d_{eg} \tilde{\rho} \left[\int_{-\infty}^{0} \tilde{\eta}(t - t') E_f(z, t') dt' + \int_{0}^{t} \tilde{\eta}(t - t') E_b(z, t') dt' \right]. \tag{4.30}$$

Using the same approach as in forward emission, we get the following equation for the evolution of field in backward mode

$$\frac{\partial}{\partial z} E_b(z, t) = \frac{\tilde{\alpha}}{2} E_b(z, t) + \tilde{\alpha} \sum_{n=-\infty}^{\infty} E_f\left(z, t - \frac{2\pi n}{\Delta} \right) e^{-\left(\frac{2\pi n}{\Delta} \right)^2 \frac{\gamma^2}{2}}. \tag{4.31}$$

The solution of Eq. (4.31) reads

$$E_b(z, t) = -\tilde{\alpha} \sum_{n=-\infty}^{\infty} e^{-\left(\frac{2\pi n}{\Delta} \right)^2 \frac{\gamma^2}{2}} e^{-\tilde{\alpha} z/2} E_f\left(0, t - \frac{2\pi n}{\Delta} \right) \int_{L}^{z} e^{-\tilde{\alpha} z'} dz'. \tag{4.32}$$

For the backward propagating field, the output at $z = 0$ becomes

$$\begin{aligned} E_b(0, t) &= -\tilde{\alpha} \sum_{n=-\infty}^{\infty} e^{-\left(\frac{2\pi n}{\Delta} \right)^2 \frac{\gamma^2}{2}} E_f\left(0, t - \frac{2\pi n}{\Delta} \right) \int_{L}^{0} e^{-\tilde{\alpha} z'} dz', \\ &= \sum_{n=-\infty}^{\infty} e^{-\left(\frac{2\pi n}{\Delta} \right)^2 \frac{\gamma^2}{2}} E_f\left(0, t - \frac{2\pi n}{\Delta} \right) (1 - e^{-\tilde{\alpha} L}). \end{aligned} \tag{4.33}$$

Thus, the efficiency corresponding to the first photon-echo in the backward mode is given by [43]

$$\eta_b = \left(1 - e^{-\tilde{\alpha}L}\right)^2 e^{-\left(\frac{2\pi\gamma}{\Delta}\right)^2}. \tag{4.34}$$

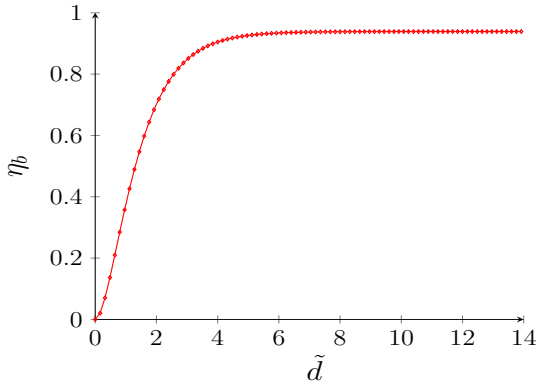

Figure 4.3: Backward mode efficiency as a function of absorption depth $\tilde{d}$ for comb finesse, $F = \Delta/\gamma = 25$.

The maximum theoretical efficiency in backward mode can reach $\sim 100\%$. Fig. 4.3 shows the variation of the efficiency in the backward mode as a function of the effective absorption depth $\tilde{d} = \tilde{\alpha}L$. The backward mode emission provides on-demand storage along with higher efficiency compared to the forward mode emission.

4.2 Quantum memory based on intra-Atomic frequency comb (I-AFC)

As discussed in the previous section, the AFC protocol requires spectral shaping of the transition of the rare-earth ion-doped crystals into a comb-shaped structure. This requires applying optical pulses and transferring the atomic population selectively to an auxiliary state. Moreover, the AFC scheme relies on the collective excitation by all the atoms in the system. A slight relative fluctuation in the phase of different atoms can affect the storage process. To overcome these difficulties, one can simply obtain the frequency comb using the transitions in an atom with multiple ground and excited states, known as the intra-atomic frequency comb (I-AFC) [49].

In I-AFC quantum memory, we consider an atom with the degenerate ground and excited hyperfine levels. The degeneracy in the hyper-fine levels is lifted by applying an external magnetic field, resulting in multiple ground and excited states. Due to the natural broadening, each allowed transition between the ground and the excited state exhibits a Lorentzian lineshape. All these multiple dipole allowed transitions collectively result in a comb-like structure known as I-AFC as shown in Fig. 4.4. Each tooth in the I-AFC corresponds to one transition between a ground state and an excited state. The frequency comb is characterized by two parameters; the width of the tooth γ (or the peak width), which is determined by the natural broadening of the concerned transition, and the comb spacing Δ, which is determined by the strength of the applied magnetic field. In the next section, we discuss the dynamics of I-AFC.

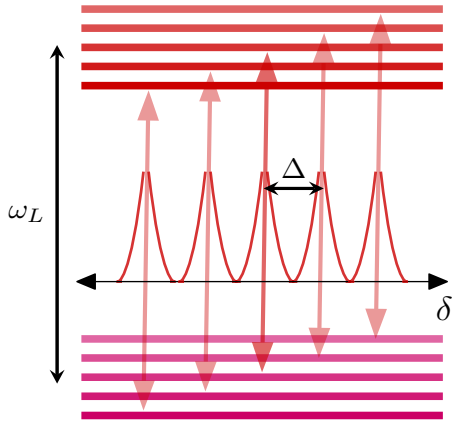

Figure 4.4: Transitions between multiple ground and excited states resulting in an intra atomic frequency comb with comb spacing Δ which is controlled by the strength of the applied magnetic field. Each transition having a natural linewidth results in a tooth width γ.

4.2.1 Dynamics of Intra-Atomic frequency comb (I-AFC)

The Hamiltonian for an atom that exhibits I-AFC, interacting with a weak electromagnetic pulse $\mathcal{E}(z,t)$ with spectral width γ_p with mean frequency ω_L reads [49]

$$H = \sum_{n=1}^{N_e} \hbar\omega_n^e \left|e_n\right\rangle\!\left\langle e_n\right| + \sum_{m=1}^{N_g} \hbar\omega_m^g \left|g_m\right\rangle\!\left\langle g_m\right| - \hbar \sum_{n,m} \left(\Omega_{nm} \left|e_n\right\rangle\!\left\langle g_m\right| e^{-i\omega_L t} + h.c.\right), \tag{4.35}$$

where $|e_n\rangle$ and $|g_m\rangle$ represents the nth excited and mth ground state respectively, corresponding to the energy $\hbar\omega_n^e$ and $\hbar\omega_m^g$ respectively, $\Omega_{nm}(z,t) = d_{nm}\mathcal{E}(z,t)/2\hbar$ is the Rabi frequency and and d_{nm} is the transition dipole moment between $|e_n\rangle \leftrightarrow |g_m\rangle$ transition. The above Hamiltonian in the interaction picture with respect to $H_0 = \sum_{n=1}^{N_e} \hbar\omega_L \left|e_n\right\rangle\!\left\langle e_n\right|$ can be written as

$$H_I = \sum_{n=1}^{N_e} \hbar(\omega_n^e - \omega_L) \left|e_n\right\rangle\!\left\langle e_n\right| + \sum_{n=1}^{N_g} \hbar\omega_n^g \left|g_n\right\rangle\!\left\langle g_n\right| - \hbar\left(\sum_{n,m} \Omega_{nm} \left|e_n\right\rangle\!\left\langle g_m\right| + h.c.\right). \tag{4.36}$$

The state of the I-AFC can be described by density matrix ρ, where $\rho_{nn} = \langle n|\rho|n\rangle$ and $\rho_{mm} = \langle m|\rho|m\rangle$ represent the population in the excited state $|e_n\rangle$ and the ground state $|g_m\rangle$, respectively, and $\rho_{nm} = \langle n|\rho|m\rangle$ represents the coherence term. The evolution of the density matrix of the atomic system is given by the Lindblad Master equation [95]

$$\frac{\mathrm{d}\rho}{\mathrm{d}t} = -\frac{\mathrm{i}}{\hbar}[H,\rho] + \left[L\rho L^\dagger - \frac{1}{2}L^\dagger L\rho - \frac{1}{2}\rho L^\dagger L\right], \tag{4.37}$$

where $L = \sqrt{\gamma}\sigma_{mn}$, is the Lindblad jump operator with $\sigma_{mn} = |e_m\rangle\langle g_n|$ and γ being the decay rate of the chosen atomic transition. Using this, the equation for the evolution of the coherence term, $\rho_{nm} = \langle n|\rho|m\rangle$ then can be written as [49]

$$\frac{\partial\rho_{nm}(r,t)}{\partial t} = -\left(i\Delta_{nm} + \frac{\gamma}{2}\right)\rho_{nm}(r,t) + i\Omega_{nm}\rho_{mm}, \tag{4.38}$$

where $\Delta_{nm} = [(\omega_n^e - \omega_m^g) - \omega_L]$ is the detuning between the transition $|e_n\rangle \leftrightarrow |g_m\rangle$ and the mean frequency of light ω_L. ρ_{mm} is the initial population in the ground state and it is assumed that the population in the excited state is negligible i.e., $\rho_{nn} \simeq 0$[1].

[1]For a weak input field, number of photons are much less than number of atoms in the ensemble, hence $\sum_m \rho_{mm} \simeq 1$ and $\rho_{nn} \simeq 0$.

The effect of the atomic polarization on the propagation of light through an atomic ensemble is described by the first order wave equation given by Eq. (2.34)

$$\left(\frac{\partial}{\partial z}+\frac{1}{c}\frac{\partial}{\partial t}\right)\mathcal{E}(z,t)=\frac{\mathrm{i}\omega_L}{2\epsilon_0 c}\mathcal{P}(z,t), \tag{4.39}$$

where $\mathcal{P}(z,t)$ is the macroscopic induced atomic polarization of the atomic ensemble and it can be written as a function of the atomic state ρ as [Eq. (2.36)]

$$\mathcal{P}(z,t)=2\mathcal{N}\sum_{n,m} d^*_{nm}\rho_{nm}, \tag{4.40}$$

where $\mathcal{N}$ is the atomic number density.

Eqs. (4.38) and (4.39) together characterize the propagation of light through an atomic ensemble. In order to obtain the electric field at a later time t and position z, we need to solve these equations simultaneously. Taking the Fourier transform of Eqs. (4.38) and (4.40), we get

$$\tilde{\rho}_{nm}(z,\omega)=\frac{i\tilde{\Omega}_{nm}\rho_{mm}}{i(\delta_{nm}+\omega)+\frac{\gamma}{2}}=\frac{id_{nm}\tilde{\mathcal{E}}(z,\omega)}{2\hbar\left[i(\delta_{nm}+\omega)+\frac{\gamma}{2}\right]}\rho_{mm}, \tag{4.41}$$

$$\tilde{\mathcal{P}}(z,\omega)=2\mathcal{N}\sum_{n,m} d^*_{nm}\tilde{\rho}_{nm}, \tag{4.42}$$

while taking the Fourier transform of Eq. (4.39) and using Eq. (4.40) gives

$$\frac{\partial\tilde{\mathcal{E}}}{\partial z}=-\left(\frac{\mathrm{i}\omega}{c}+\frac{\omega_L\mathcal{N}}{2c\hbar\epsilon_0}\sum_{n,m}\frac{|d_{nm}|^2}{\left[\mathrm{i}(\delta_{nm}+w)+\frac{\gamma}{2}\right]}\rho_{mm}\right)\tilde{\mathcal{E}}. \tag{4.43}$$

Since a typical dipole allowed atomic transition absorbs and emits light in accordance with the transition selection rules $\Delta m=\pm 1$, we write d_{nm} in the spherical basis, hence the dipole matrix element d_{nm} is always real.

Solving the above equation gives the following expression for the output electric field in the frequency domain [49]

$$\tilde{\mathcal{E}}(z,\omega)=e^{-\mathcal{D}z}e^{-\mathrm{i}\omega z/c}\tilde{\mathcal{E}}(0,\omega), \tag{4.44}$$

where $\tilde{\mathcal{E}}(0,\omega)$ is the input electric field amplitude and $\mathcal{D}$ is given by

$$\mathcal{D}=\sum_{n,m}\frac{g_{mm}}{\left[\mathrm{i}(\Delta_{nm}+\omega)+\frac{\gamma}{2}\right]}d^2_{nm}, g_{mm}=\frac{\omega_L\mathcal{N}\rho_{mm}}{2c\hbar\epsilon_0}. \tag{4.45}$$

In the ideal case, when the comb spacing Δ_{nm} and the dipole matrix elements d_{nm} are the same for all neighbouring transitions, a photon-echo is observed in the output at times which are integral multiples of $2\pi/\Delta$. In non-ideal cases, when the frequency comb is non-uniform, the photon-echo may be observed at $2\pi/\Delta'$, for some effective comb spacing Δ' [50] with lower efficiency. In this way, the I-AFC system behaves like a delay line. To achieve on-demand quantum memory, the excitation is transferred from the excited level to a long-lived spin level by applying an appropriate π-pulse. Another such pulse will transfer the excitation back to the excited level, which will cause the photon-echo.

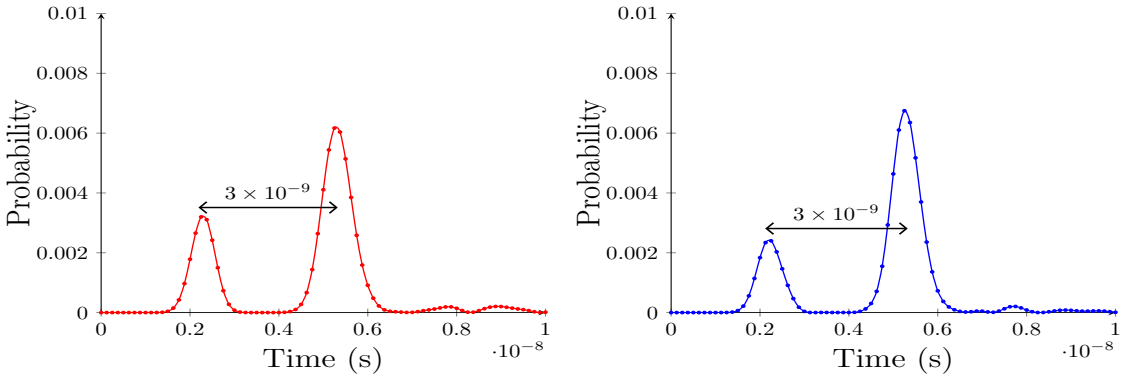

(a) (b)

Figure 4.5: Photon-echo in Cs atom ($6s_{1/2} \rightarrow 8p_{3/2}$) corresponding to the transition selection rule $\Delta m = -1$ and $+1$, respectively, at an applied magnetic field strength of 0.1 T.

Similar to the AFC, the efficiency η of the I-AFC quantum memory protocol is defined as

$$\eta = \frac{\int_{\pi/\Delta}^{3\pi/\Delta} |\mathcal{E}(z = L, t)|^2 \, dt}{\int |\mathcal{E}(z = 0, t)|^2 \, dt}. \tag{4.46}$$

where L is the length of the atomic ensemble along the direction of propagation of light. The maximum efficiency that can be achieved using the standard I-AFC scheme is 54% in the forward mode and 100% in the backward mode [49].

Fig. 4.5(a) and 4.5(b) show the numerically obtained photon-echo for an ensemble of Cs atoms corresponding to the transition selection rule $\Delta m = \pm 1$ for the transition $6s_{1/2} \rightarrow 8p_{3/2}$. Here the length of the ensemble is fixed to be 5 cm, and

the atomic number density $\mathcal{N}$ is taken to be 10^{18} m^{-3}. The applied magnetic field strength is 0.1 T. The optimized efficiency in the case of Cs atoms is obtained to be $\sim 52\%$.

While the AFC scheme is based on the spectral shaping of the broad inhomogeneous absorption profile of a transition between a single ground and excited state, in the I-AFC scheme, the frequency comb is formed due to the presence of all dipole allowed transitions between the multiple ground and excited hyperfine levels. Thus, the comb width only depends on the number of dipole allowed transitions and the strength of the applied magnetic field. It does not change as we reduce the temperature and is sufficient enough to be covered by the pulse width. Further, in a typical I-AFC, the minimum number of peaks required to get photon-echo is 5, which gives the lower limit for the minimum comb width $\sim 4\Delta$.

Thus, the I-AFC protocol can be used for robust and efficient storage of photons, and unlike AFC, it does not require specific preparation techniques such as spectral hole burning and selective optical pumping to achieve the frequency comb structure. Moreover, the echo time can be adjusted by tuning the magnetic field, which directly changes the comb spacing Δ.

In the next chapter, we discuss how can we use this I-AFC protocol to store the internal degrees of freedom of photons, such as the polarization and orbital angular momentum of photons. This can be utilized to store the vector-vortex states of light.

Chapter 5

Multimode quantum memory using intra-atomic frequency comb

Some of the common degrees of freedom (DoFs) of photons used in quantum information processing (QIP) tasks are polarization, time-bins and the orbital angular momentum (OAM) [3]. While the polarization space is two-dimensional, the time-bins and OAM space are potentially infinite dimensional, which enables high information carrying capacity in individual photons. One of the biggest challenges in photonic quantum information processing tasks is to store and retrieve the photons while preserving their internal states in an efficient and controllable way.

Typically, the atoms are tuned to interact with a single polarization in atomic ensemble-based quantum memories. Therefore, one can not store polarization states of light in such systems. Several solutions have been implemented to overcome this problem. For example, in EIT-based quantum memories, the orthogonal polarization states of the input light are mapped to two distinguished paths with the same polarizations and absorbed in the atomic ensemble. Finally, when the light is retrieved, the paths are mapped to the polarization states at the output [107, 52, 108, 109, 110]. A similar technique is used in AFC-based quantum memory to store the polarization DoF of light [111, 112, 113, 56]. The EIT and AFC-based quantum memories have been shown to store transverse modes [114, 115, 116, 117, 118, 119, 120, 121, 57, 55], however, only EIT is extended to

store polarization and OAM simultaneously [54, 122].

Apart from these two techniques, polarization storage has also been implemented using an atom-cavity system. [123, 124]. A CRIB protocol with two orthogonal transitions is also proposed to store polarization [125, 58]. However, this requires the reversal of detunings in a controlled fashion and the application of a position-dependent phase for efficient retrieval.

In this chapter, we present a scheme to store the vector-vortex (VV) states of light using I-AFC [51]. Since each of the atom contains a frequency comb, I-AFC-based quantum memory is robust against phase fluctuations and uniformity in the comb structure [50].

VV states are the quasi-entangled states between polarization and OAM DoFs of light and are very useful for QIP tasks and quantum metrology [63, 64, 65]. We show that I-AFC is a natural candidate for storing VV states by showing that it can individually store the polarization and OAM modes efficiently. Unlike EIT-based quantum memory, the I-AFC does not require high optical depths and elongated atomic traps to store VV states of light. An I-AFC can easily be realized by Zeeman splitting the hyperfine levels in atoms and possesses all the necessary features of a typical AFC [49]. This makes the I-AFC a feasible tool to implement protocols using OAM and polarization qubits. We also show that I-AFCs in Cs and Rb atoms can be employed to store VV states.

We start with a brief introduction to VV beams. Subsequently, we discuss storing VV states of light in ideal I-AFC systems. We also discuss factors that affect the quality of the storage. We then show numerically that an ensemble of Cs and Rb atoms can store VV states efficiently under appropriate conditions.

5.1 Vector-vortex states

The general state of the transverse Laguerre-Gauss (LG) modes along with the polarization can be written as

$$\boldsymbol{\mathcal{E}}(\mathbf{r}_\perp) = \sum_{\ell,p} \left(\alpha_{\ell,p} LG_p^\ell(\mathbf{r}_\perp)\,|R\rangle + \beta_{\ell,p} LG_p^\ell(\mathbf{r}_\perp)\,|L\rangle\right), \tag{5.1}$$

where $LG_p^\ell(\mathbf{r}_\perp)$ represents the LG mode with radial index p and azimuthal index ℓ given by Eq. (2.39). $|R\rangle$ ($|L\rangle$) corresponds to the right (left) circular polarization and $\alpha_{\ell,p}, \beta_{\ell,p} \in \mathbb{C}$ such that $\sum_{\ell,p}\left(|\alpha_{\ell,p}|^2 + |\beta_{\ell,p}|^2\right) = 1$.

In this work, we set $p = 0$ and represent LG_0^ℓ by $|\ell\rangle$. Further, we restrict to only $\pm\ell$ values of OAM and consider the states of the form

$$\boldsymbol{\mathcal{E}}(\mathbf{r}_\perp) = [\alpha\,|\ell\rangle\,|R\rangle + \beta\,|-\ell\rangle\,|L\rangle]. \tag{5.2}$$

These states are called the vector-vortex states [62, 54] and they exhibit a position dependent polarization in the transverse plane. In Fig. 5.1 we show two such VV states for different choices of α and β.

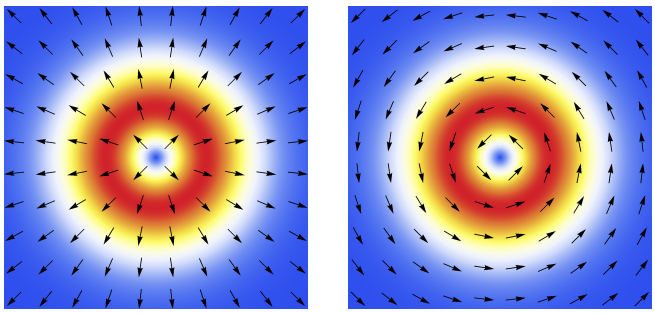

(a) (b)

Figure 5.1: Polarization distribution in VV states. (a) (b) corresponds to the states $\frac{1}{\sqrt{2}}[|\ell\rangle\,|R\rangle + |-\ell\rangle\,|L\rangle]$ and $\frac{\mathrm{i}}{\sqrt{2}}[|\ell\rangle\,|R\rangle - |-\ell\rangle\,|L\rangle]$ respectively.

5.2 Storing VV states

In this section, we show that the VV states of light can be stored efficiently in an appropriately designed I-AFC-based quantum memory. Here, we start with storing

the LG modes of a paraxial light in I-AFC. We show that if the number density $\mathcal{N}$ of the atomic ensemble is homogeneous, then the LG modes can be stored perfectly at low temperatures. At high temperatures, the Doppler shift may affect the quality of storage. In order to store polarization states of light, we need to prepare an ensemble that contains two frequency combs corresponding to two orthogonal polarizations. We show that if the two frequency combs are identical, then the storage of the polarization states is perfect. Non-identical combs might result in imperfect storage. The I-AFC system, whih is capable of storing both LG modes and polarization states, can be employed to store VV beams. For example, we show that I-AFC in Cs and Rb atoms can store VV modes [51].

5.2.1 Storing LG modes in I-AFC

LG modes are the eigenmodes of the paraxial wave equation in free space. However, in an atomic ensemble, they might get affected due to the presence of induced atomic polarization $\mathcal{P}$, especially if the medium is inhomogeneous. In this section, we show that an atomic ensemble possessing I-AFC can store LG modes of light. In order to do so, we will solve the propagation of the LG modes through such an atomic ensemble and show that we observe a photon-echo at time $2\pi/\Delta$ with high efficiency, which is a signature of the I-AFC-based quantum memory. Further, we show that the fidelity between the input and output states of light is near perfect for an idealized case.

The Hamiltonian of the atomic ensemble interacting with a classical electromagnetic field can be written as

$$H = \sum_{n=1}^{N_e} \hbar\omega_n^e \left|e_n\right\rangle\!\left\langle e_n\right| + \sum_{m=1}^{N_g} \hbar\omega_m^g \left|g_m\right\rangle\!\left\langle g_m\right| - \hbar \sum_{n,m} \left(\Omega_{nm} \left|e_n\right\rangle\!\left\langle g_m\right| e^{-\mathrm{i}\omega_L t} + H.c.\right), \quad (5.3)$$

where $\hbar\omega_n^e$ is the energy of the nth state in the excited level, $\hbar\omega_m^g$ is the energy of the mth state in the ground level, and $\Omega_{nm} = \dfrac{d_{nm}\mathcal{E}(\mathbf{r}_\perp, z, t)}{2\hbar}$. Here, the electric field $\mathcal{E}(\mathbf{r}_\perp, z, t)$ has the mean frequency ω_L.

For simplification, we have assumed here that the chosen I-AFC interacts with a fixed polarization state, i.e., right or left circular polarization (corresponding to the

transition selection rule $\Delta m = \pm 1$), and the electric field $\mathcal{E}(\mathbf{r}_\perp, z, t)$ is also polarized along the same direction so that the dot product between d_{nm} and $\mathcal{E}(\mathbf{r}_\perp, z, t)$ does not appear in Ω_{nm}. However, as we will see in the next section, one can use a dual comb structure to store a transverse field polarized in an arbitrary direction, which will form a basis to store the VV states.

The paraxial wave equation inside a medium can be written as [see Eq. (2.33)]

$$\left[\nabla_\perp^2 + 2\mathrm{i}k\left(\frac{\partial}{\partial z} + \frac{1}{c}\frac{\partial}{\partial t}\right)\right]\mathcal{E}(\boldsymbol{r}, t) = -\frac{k^2}{\epsilon_0}\mathcal{P}(\boldsymbol{r}, t), \tag{5.4}$$

where $\mathcal{P}$ is the induced atomic polarization. Further, the dynamical equation for the atomic coherence corresponding to the Hamiltonian in Eq. (5.3) can be written as

$$\frac{\partial \rho_{nm}(\mathbf{r}_\perp, z, t)}{\partial t} + \left(i\Delta_{nm} + \frac{\gamma}{2}\right)\rho_{nm}(\mathbf{r}_\perp, z, t) = i\frac{d_{nm}\mathcal{E}(\mathbf{r}_\perp, z, t)}{2\hbar}\rho_{mm}. \tag{5.5}$$

The paraxial wave equation along with the dynamical equation for the atomic coherence can be solved together for spatially homogeneous medium (see Appendix A for details) and gives the following expression for the output field

$$\mathcal{E}(\mathbf{r}_\perp, z, t) = \int M(\mathbf{r}_\perp - \mathbf{r}'_\perp, z) \times \left[\int N(t-\tau, z)\mathcal{E}(\mathbf{r}'_\perp, 0, \tau - \frac{z}{c})d\tau\right] d^2\mathbf{r}'_\perp. \tag{5.6}$$

where

$$M(\mathbf{r}_\perp, z) = \frac{1}{2\pi}\int e^{\mathrm{i}\mathbf{q}.\mathbf{r}_\perp} e^{-\mathrm{i}q^2 z/2k} d^2\mathbf{q}, \tag{5.7}$$

$$N(t, z) = \frac{1}{2\pi}\int e^{\mathrm{i}\omega t} e^{-\mathcal{D}(\omega)z} d\omega, \tag{5.8}$$

and the variables $\mathbf{q}$ and ω correspond to the Fourier transform in the transverse position ($\mathbf{r}_\perp \to \mathbf{q}$) and time ($t \to \omega$), respectively. $\mathcal{D}(\omega)$ represents the I-AFC propagator given by Eq. (4.45).

If the input light is in a pure LG mode $LG_0^l(\mathbf{r}_\perp)$ with a temporal profile given by $\mathcal{E}(0, t)$, then the expression for the input electric field $\mathcal{E}(\mathbf{r}_\perp, 0, t)$ reads

$$\mathcal{E}(\mathbf{r}_\perp, 0, t) = \mathcal{E}(0, t)LG_0^l(\mathbf{r}_\perp). \tag{5.9}$$

In this case, the output field $\mathcal{E}(\mathbf{r}_\perp, z, t)$ will be

$$\mathcal{E}(\mathbf{r}_\perp, z, t) = \left(\int M(\mathbf{r}_\perp - \mathbf{r}'_\perp, z)LG_0^l(\mathbf{r}'_\perp)\, d^2\mathbf{r}'_\perp\right) \times \left(\int N(t-\tau, z)\, \mathcal{E}(0, \tau - z/c)d\tau\right). \tag{5.10}$$

Interestingly, the evolution of the electric field $\mathcal{E}(\mathbf{r}_\perp, 0, t)$ splits into two parts, one which drives the transverse evolution and the other which drives the time evolution. On close inspection, we can see that the evolution in the transverse plane is identical to the one in the vacuum, as shown in Eq. (2.44). Since LG modes are the eigenmodes of paraxial wave-equation, the pure LG modes remain unaffected in this evolution except acquiring an overall phase, i.e., Gouy phase given by $\exp[-\mathrm{i}(|\ell|+1)\tan^{-1}(z/z_R)]$ [Eq. (2.39)]. In our numerical calculations, we have considered the length of the medium to be 5 cm and the transverse dimensions to be ~ 8 mm, as can be found in some magneto-optical traps setups at low temperatures [126]. Therefore, the beam waist w_0 will be of the order of millimeters. These parameters result in $z/z_R = z\lambda/\pi w_0^2 \sim 10^{-4}$. Therefore, the Gouy phase becomes negligible which allows us to store a superposition of LG modes.

Furthermore, the information about the I-AFC is completely contained in the kernel N which controls the time evolution of the state. Therefore, the temporal part in Eq. (5.10) is identical to the ordinary I-AFC evolution which results in a photon-echo at times which are multiples of $2\pi/\Delta$, without affecting the transverse part. Therefore, I-AFC in the homogeneous atomic ensemble is fully capable of storing LG modes of light.

The quality of the quantum memory can be expressed in terms of two parameters: storage efficiency η and the fidelity $\mathcal{F}$ between the input and output states of light. The storage efficiency of the quantum memory in the I-AFC protocol is defined as the ratio of the output intensity in the first echo to the total input intensity of light and reads [49]

$$\eta = \frac{\int_{\pi/\Delta}^{3\pi/\Delta} dt |\mathcal{E}(z=L,t)|^2}{\int dt |\mathcal{E}(z=0,t)|^2}, \tag{5.11}$$

where L is the length of the atomic ensemble. The fidelity of the quantum memory describes the amount of overlap between the input state $|\Psi_{in}\rangle$ and the output state $|\Psi_{out}\rangle$, and can be formally written as

$$\mathcal{F} = |\langle \Psi_{\mathrm{in}} | \Psi_{\mathrm{out}} \rangle|^2. \tag{5.12}$$

Since in I-AFC, the output electric field comes out at time $2\pi/\Delta$, the fidelity in the

I-AFC scheme between the input electric field $\mathcal{E}_{\text{in}}(t)$ and the first echo is given as

$$\mathcal{F} = \frac{\left| \int_{\pi/\Delta}^{3\pi/\Delta} dt \ \langle \boldsymbol{\mathcal{E}}_{\text{in}}(t - 2\pi/\Delta) | \boldsymbol{\mathcal{E}}_{\text{out}}(t) \rangle \right|^2}{\left[\int dt \ \langle \boldsymbol{\mathcal{E}}_{\text{in}} | \boldsymbol{\mathcal{E}}_{\text{in}} \rangle \right] \left[\int dt \ \langle \boldsymbol{\mathcal{E}}_{\text{out}} | \boldsymbol{\mathcal{E}}_{\text{out}} \rangle \right]}. \tag{5.13}$$

The most general state of light, including the polarization and the transverse profile, can be written as

$$\boldsymbol{\mathcal{E}}(t) = \begin{bmatrix} \mathcal{E}_+(x, y, t) \\ \mathcal{E}_-(x, y, t) \end{bmatrix}, \tag{5.14}$$

where $\mathcal{E}_+$ ($\mathcal{E}_-$) corresponds to the right (left) polarization component of the electric field and x, y are the transverse coordinates. In such cases, the expression for the fidelity between the input and output can be written as

$$\mathcal{F} = \frac{\left| \int_{\pi/\Delta}^{3\pi/\Delta} dt \ \int dx\, dy \ \left[\mathcal{E}^*_{\text{in}+}(x, y, t - 2\pi/\Delta) \mathcal{E}_{\text{out}+}(x, y, t) + \mathcal{E}^*_{\text{in}-}(x, y, t - 2\pi/\Delta) \mathcal{E}_{\text{out}-}(x, y, t) \right] \right|^2}{\left[\int dt \ \int dx\, dy \ (|\mathcal{E}_{\text{in}+}|^2 + |\mathcal{E}_{\text{in}-}|^2) \right] \left[\int dt \ \int dx\, dy \ (|\mathcal{E}_{\text{out}+}|^2 + |\mathcal{E}_{\text{out}-}|^2) \right]}. \tag{5.15}$$

This definition will be used in the next section where we discuss regarding polarization storage.

In Fig. 5.2 we plot the numerically obtained re-emission of LG modes from an ideal I-AFC. The comb spacing Δ here is 400 MHz, and peak width γ is 5 MHz. We choose LG_0^1, $(LG_0^1 + LG_0^{-1})/\sqrt{2}$ and $(LG_0^1 + \mathrm{i}LG_0^{-1})/\sqrt{2}$ modes with a Gaussian temporal profile. As expected, the LG modes rephase after time $2\pi/\Delta$ while preserving the transverse profile. The first transverse profile in Fig. 5.2 at ~ 0.23ns corresponds to the probability of the photon being unabsorbed, while the second transverse profile at $\sim$ 2.7ns represents the photon-echo corresponding to the input LG mode. The brightness of the transverse profile is proportional to the probability of the photon emission, which clearly indicates the higher probability of the first echo relative to the noise at ~ 0.23ns. The optimized efficiency and fidelity are found to be 53.44% and 100%.

Since for the parameters we have considered the Gouy phase is very small, one can store an arbitrary superposition of higher-dimensional LG modes (within a reasonable range of ℓ values) without affecting the fidelity. In Fig. 5.3 we show rephasing of the $(LG_0^1 + LG_0^{-5} + LG_0^{10})/\sqrt{3}$ state with $\sim 100\%$ fidelity.

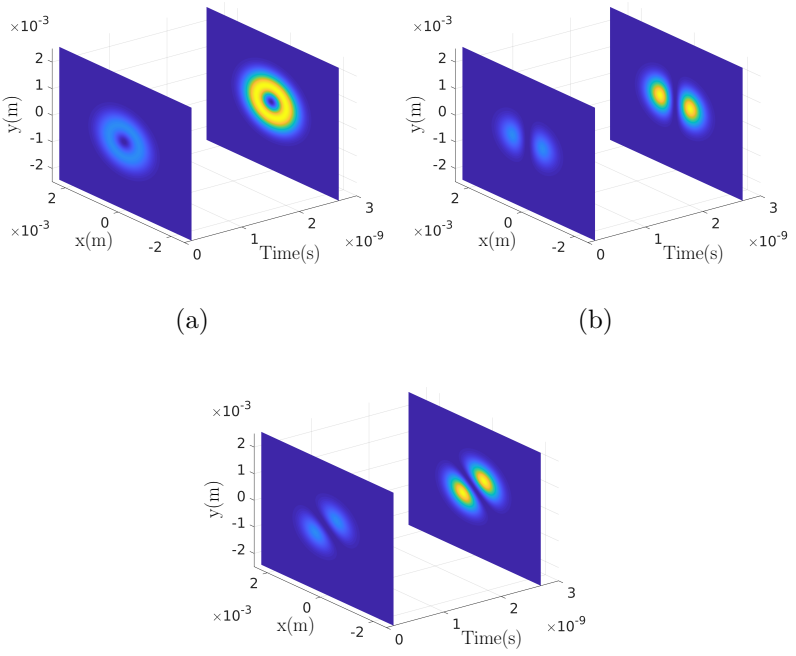

Figure 5.2: Storing OAM in I-AFC. (a), (b) and (c) Photon echoes for the ideal comb for the OAM states $|1\rangle$, $(|1\rangle+|-1\rangle)/\sqrt{2}$ and $(|1\rangle+\mathrm{i}\,|-1\rangle)/\sqrt{2}$ respectively. The first and the second transverse profile in the plots correspond to the probability of the photon being unabsorbed and the probability of the photon-echo. All the calculations are done at 0K.

Note that the storage of the LG modes was made possible by the assumption that the atomic number density $\mathcal{N}(\mathbf{r}_\perp)$ is homogeneous in the transverse plane, which made the kernel N independent of the transverse coordinates $\mathbf{r}_\perp$. Inhomogeneity in the atomic ensemble will affect the LG modes and the storage fidelity will not be perfect. We will discuss this in detail in Sec. 5.3.

5.2.2 Storing polarization qubit

In order to store polarization states of light, the system of interest must be capable of interacting with two orthogonal states of light identically. Here, we present a scheme to store polarization states using I-AFC-based quantum memory. For that purpose, we consider atoms with degenerate ground and excited states. The external

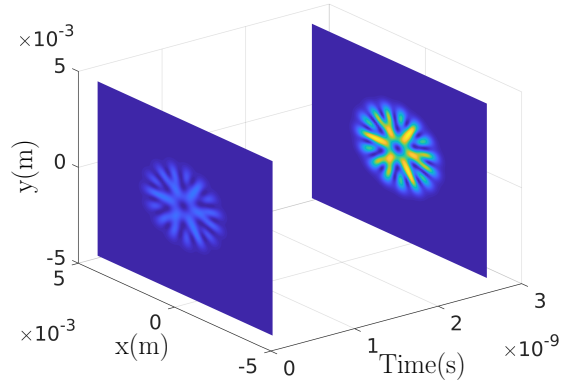

Figure 5.3: Photon-echo for the ideal comb for the OAM state $(|1\rangle + |-5\rangle + |10\rangle)/\sqrt{3}$.

magnetic field to lift the degeneracy is applied in the z direction. Therefore, the transitions between the ground states and the excited states satisfy the selection rules $\Delta m = \pm 1$. The Hamiltonian for such a system interacting with a light pulse of mean frequency ω_L reads

$$H = \sum_{n=1}^{N_e} \hbar\omega_n^e \, |e_n\rangle\langle e_n| + \sum_{m=1}^{N_g} \hbar\omega_m^g \, |g_m\rangle\langle g_m| - \hbar \sum_{n,m} \left(\Omega_{nm} \, |e_n\rangle\langle g_m| \, e^{-\mathrm{i}\omega_L t} + H.c.\right), \tag{5.16}$$

where

$$\Omega_{nm} = \frac{\mathbf{d}_{nm} \cdot \boldsymbol{\mathcal{E}}(z,t)}{2\hbar}, \tag{5.17}$$

with $\mathbf{d}_{nm} = d_{nm}^{+}\hat{\mathbf{e}}_{+} + d_{nm}^{-}\hat{\mathbf{e}}_{-} \equiv \begin{bmatrix} d_{nm}^{+} \\ d_{nm}^{-} \end{bmatrix}$ being the transition dipole moment vector between the nth excited state $|e_n\rangle$ and the mth ground state $|g_m\rangle$ where the elements of the vector correspond to $\Delta m = \pm 1$ transitions.

The electric field vector $\boldsymbol{\mathcal{E}}(z,t)$ in a superposition of the two polarizations can be written as [127]

$$\boldsymbol{\mathcal{E}}(z,t) = \mathcal{E}_{+}(z,t)\hat{\mathbf{e}}_{+} + \mathcal{E}_{-}(z,t)\hat{\mathbf{e}}_{-} \equiv \begin{bmatrix} \mathcal{E}_{+} \\ \mathcal{E}_{-} \end{bmatrix}, \tag{5.18}$$

where $\hat{\mathbf{e}}_{\pm}$ are the unit vectors along the left and right circular polarization and interact with the transition corresponding to $\Delta m = \pm 1$.

The dynamics of the electric field and the atomic ensemble is given by Maxwell-Schrödinger equations [Eqs. (4.38) and (4.39)]. Solving the dynamics for the electric field vectors results in the following expression for the output electric field $\tilde{\boldsymbol{\mathcal{E}}}$ in the frequency domain,

$$\frac{\partial \tilde{\boldsymbol{\mathcal{E}}}}{\partial z} = -\frac{\mathrm{i}\omega}{c}\tilde{\boldsymbol{\mathcal{E}}} - \frac{\omega_L \mathcal{N}}{2c\hbar\epsilon_0}\sum_{n,m}\frac{\mathbf{d}_{nm}(\mathbf{d}_{nm}\cdot\tilde{\boldsymbol{\mathcal{E}}})}{\left[\mathrm{i}(\Delta_{nm}+\omega)+\frac{\gamma}{2}\right]}\rho_{mm}, \tag{5.19}$$

where ρ_{mm} is the population of the mth energy level. On using Eqs. (5.18) and (5.19), the equations for the two orthogonal polarization components can be written as

$$\frac{\partial}{\partial z}\begin{bmatrix}\tilde{\mathcal{E}}_+\\ \tilde{\mathcal{E}}_-\end{bmatrix} = \begin{bmatrix}-\mathrm{i}\omega/c - \mathcal{D}^+(\omega) & -\mathcal{G}(\omega)\\ -\mathcal{G}(\omega) & -\mathrm{i}\omega/c - \mathcal{D}^-(\omega)\end{bmatrix}\begin{bmatrix}\tilde{\mathcal{E}}_+\\ \tilde{\mathcal{E}}_-\end{bmatrix} \equiv A\begin{bmatrix}\tilde{\mathcal{E}}_+\\ \tilde{\mathcal{E}}_-\end{bmatrix}. \tag{5.20}$$

From Eq. (5.20) we can calculate the output electric field, which reads $\tilde{\boldsymbol{\mathcal{E}}}(z,\omega) = \mathrm{e}^{Az}\tilde{\boldsymbol{\mathcal{E}}}(0,\omega)$. Here, $\mathcal{D}^{\pm}(\omega)$ and $\mathcal{G}(\omega)$ are defined as

$$\mathcal{D}^{\pm}(\omega) = \sum_{nm}\frac{g_{mm}}{\left[\mathrm{i}(\Delta_{nm}+\omega)+\frac{\gamma}{2}\right]}d_{nm}^{\pm 2}, \tag{5.21}$$

$$\mathcal{G}(\omega) = \sum_{nm}\frac{g_{mm}}{\left[\mathrm{i}(\Delta_{nm}+\omega)+\frac{\gamma}{2}\right]}d_{nm}^{+}d_{nm}^{-}. \tag{5.22}$$

For the case when the magnetic quantum number m is not a good quantum number for atomic states, both the transition dipole moments $d_{nm}^{\pm}$ between the nth excited state and the mth ground state might not vanish. This will result in a nonzero $\mathcal{G}(\omega)$ term which is responsible for the mixing of the two polarizations. On the other hand, the terms $\mathcal{D}^{\pm}(\omega)$ in Eq. (5.20) are the propagators corresponding to the two I-AFCs corresponding to $\Delta m = \pm 1$ transitions. For the case when the off-diagonal term vanishes, the two orthogonal polarizations propagate independently through the I-AFC.

To calculate fidelity for the storage of polarization qubit, we use Eq. (5.15) and

define the fidelity for polarization qubit as

$$\mathcal{F} = \frac{\left|\int_{\pi/\Delta}^{3\pi/\Delta} dt \;\; \left[\mathcal{E}^*_{\text{in}+}(t-2\pi/\Delta)\mathcal{E}_{\text{out}+}(t) + \mathcal{E}^*_{\text{in}-}(t-2\pi/\Delta)\mathcal{E}_{\text{out}-}(t)\right]\right|^2}{\left[\int dt \;\; (|\mathcal{E}_{\text{in}+}|^2 + |\mathcal{E}_{\text{in}-}|^2)\right]\left[\int dt \;\; (|\mathcal{E}_{\text{out}+}|^2 + |\mathcal{E}_{\text{out}-}|^2)\right]}, \tag{5.23}$$

where $\pm$ denotes the left and right circular polarization component of the input and output polarization qubit. This gives the information about the temporal overlap of the input and output pulse as well as the polarization fidelity, which can not be unity if $\mathcal{G}(\omega)$ is not zero indicating a mixing of the polarization.

Note that if $D^{\pm}(\omega)$ is same for both polarizations and $\mathcal{G} = 0$, then the matrix A is proportional to the identity matrix. Hence, the propagation of the light inside the I-AFC will be independent of the polarization, resulting in polarization-independent storage. In such cases, the I-AFC-based quantum memory can store the polarization efficiently. However, in physical systems the propagators for the two combs may not always be equal. Different propagators $\mathcal{D}^{\pm}$ may result in different photon-echo times and different efficiencies for orthogonal polarizations, which in turn may result in lower fidelity between the input and output states of light if the input light is in some superposition of the two polarizations.

In conclusion, an atomic ensemble containing two identical I-AFCs corresponding to two orthogonal polarizations can store polarization states of light efficiently. Since the OAM states of light (LG modes) are independent of polarization, if the atomic ensemble is homogeneous, it can also be used to store these states efficiently. Therefore, one can store VV states of light in I-AFC-based quantum memory.

5.3 Factors affecting the quality of quantum memory

So far, we have discussed the storage of VV modes only in ideal systems. There are several factors that might affect the quality of the storage. In this section, we discuss some factors, such as temperature and non-homogeneous number density, and their effects in detail. Although the non-uniformity in the frequency comb can

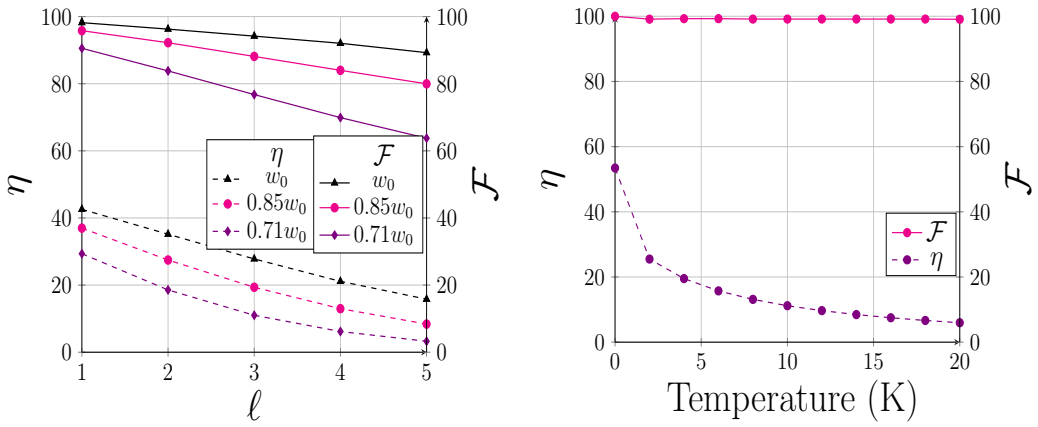

(a) (b)

Figure 5.4: The efficiency (dashed curve) and the fidelity (solid curve) for different values of w_0' as a function of ℓ for the input state $|\ell\rangle$ in (a) and as a function of temperature for the OAM state $(|1\rangle + |-1\rangle)/\sqrt{2}$ in (b). For these plots, we consider an ideal comb consisting of nine peaks with uniform comb spacing $\Delta = 400$ MHz giving a comb width of $\sim 8\Delta$ and the peak width γ is taken to be 5 MHz. The spectral width of the input pulse is 600 MHz.

also affect the efficiency of the quantum storage [50], it seldom affects the fidelity of the stored light. Therefore, in this section, we restrict our analysis to ideal combs. We consider examples of the non-ideal and non-uniform frequency comb in Sec. 5.4, where we show the storage of VV beams in Cs and Rb atoms.

5.3.1 Effects of the nonhomogeneous number density on the storage of LG modes

As we have noticed in the case of storing LG modes in homogeneous systems, the evolution of the electric field decouples in two parts [Eq. (5.10)]; one corresponds to the evolution in the transverse plane, and the other corresponds to the time evolution. However, if the atomic number density is not homogeneous, this separation is not guaranteed. To study the adverse effect of the nonhomogeneous number density on the quality of the quantum memory, we consider a simple case in which the number density is a function of $|\mathbf{r}_\perp| \equiv r_\perp = \sqrt{x^2 + y^2}$, in the transverse plane. For simplicity, we choose a Gaussian distribution of atomic density in the trans-

verse plane, i.e., $\mathcal{N}'(\mathbf{r}_\perp) = \mathcal{N}_0 \exp[-(x^2+y^2)/2w_0'^2]$, where w_0' is the width of the distribution and $\mathcal{N}_0$ is a constant.

In order to calculate the effect of the nonhomogeneous number density, we numerically solve the paraxial wave equation for the electric field given in Eq. (5.4) along with the dynamical equation for the atomic coherence in Eq. (5.5). The efficiency of the photon-echo and the fidelity between the input and output states of the electric field can be calculated using the relations for the efficiency and the fidelity given in Eqs. (5.11) and Eq. (5.15), respectively. In fig. 5.4(a) we plot the efficiency η and the fidelity $\mathcal{F}$ as a function of the ℓ value of the LG modes for different values of w_0' for a fixed beam waist w_0, while keeping $p = 0$.

As expected, the non-homogeneity of the atomic ensemble affects the quality of the quantum memory more for the larger values of ℓ. This result can be explained by noticing that the size of the transverse profile of the LG modes increases with increasing the ℓ value. Hence, the beams with a large ℓ value see fewer atoms, which results in a lower absorption rate and hence lower efficiency. Furthermore, the LG modes are not the eigenmodes inside the non-homogeneous medium. This explains the drop in the fidelity.

5.3.2 Effects of temperature on the storage of LG modes

Besides the nonhomogeneous number density, thermal effects can also affect the quality of the storage of OAM states of light. We first introduce the effect of Doppler shift on the LG modes, and then use it to study the effect on temperature on storing the LG modes.

5.3.2.1 Effect of Doppler shift on OAM states of light

Light carrying non-zero OAM interacts differently with an atomic ensemble. A moving atom interacting with a light beam carrying $\ell\hbar$ OAM experiences an ℓ-dependent Doppler shift in the azimuthal direction apart from the usual longitudinal Doppler shift kv_z. This azimuthal Doppler shift is entirely due to the OAM modes

of light. The total Doppler shift for OAM state $|\ell\rangle$ with an arbitrary polarization is given by [128, 129]

$$\begin{aligned}\delta_{LG} =& v_z\left(-k + \frac{kr^2(z^2 - z_R^2)}{2(z^2 + z_R^2)^2} - \frac{(|\ell| + 1)z_R}{(z^2 + z_R^2)}\right) - v_r\left(\frac{kr}{\bar{z}}\right) - v_\phi\left(\frac{\ell}{r}\right) \\ =& \delta_z + \delta_r + \delta_\phi,\end{aligned} \tag{5.24}$$

where v_r, v_ϕ, and v_z are the radial, azimuthal, and longitudinal components of the velocity $\mathbf{v}$ of the atom.

Here the term kv_z is the usual Doppler shift along the propagation direction and will be the only term for a plane wave. The term $\propto (|\ell| + 1)$ is due to the Gouy phase of the LG mode and the terms including v_z and v_r are due to the transverse profile of the LG modes along the radial direction [128]. The final ℓ dependent term which is directly proportional to the OAM of the LG mode accounts for the azimuthal Doppler shift. Typically, kv_z is the leading term dominating by a factor 10^4 [130] compared to the radial and azimuthal Doppler shifts. The above ℓ-dependent Doppler shift yields an ℓ-dependent phase in the paraxial light, which might affect the fidelity of the OAM modes upon storage. In the next section, we use the above Doppler shift δ_{LG} to incorporate the effect of temperature on the storage of OAM modes.

5.3.2.2 Effects of doppler shift on storing LG modes

To study the effect of the temperature on the OAM storage, we consider a homogeneous atomic ensemble in thermal equilibrium at temperature T. The atomic velocity distribution in such an ensemble can be written as

$$p(v)d^3v = \left(\frac{m}{2\pi k_b T}\right)^{3/2} \exp\left(-m(v_x^2 + v_y^2 + v_z^2)/2k_B T\right) d^3v, \tag{5.25}$$

where m is the mass of the atom, v_x, v_y, and v_z are the velocities of the atom along the x, y, and z directions, respectively; and k_B is the Boltzmann constant.

An atom moving with velocity $\mathbf{v}$ and interacting with light with a nonzero OAM value experiences a change in the detuning from Δ to $\Delta + \delta_{LG}(\mathbf{v})$ due to the Doppler shift given by Eq. (5.24). Hence, the modified expression for the atomic polarization

$\tilde{\mathcal{P}}(\mathbf{r}_\perp, z, \omega, \mathbf{v})$ after incorporating the Doppler shift can be written as

$$\tilde{\mathcal{P}}(\mathbf{r}_\perp, z, \omega, \mathbf{v}) = 2\mathcal{N} \sum_{n,m} \frac{\mathrm{i} d_{nm}^2 \tilde{\mathcal{E}}(\mathbf{q}, z, \omega) \rho_{mm}}{2\hbar \left[\mathrm{i}(\Delta_{nm} + \delta_{LG}(\mathbf{v}) + \omega) + \frac{\gamma}{2} \right]}. \tag{5.26}$$

The net atomic polarization can be calculated by averaging $\tilde{\mathcal{P}}(\mathbf{r}_\perp, z, \omega, \mathbf{v})$ over all the velocities [131, 49], i.e.,

$$\tilde{\mathcal{P}}(\mathbf{r}_\perp, z, \omega) = \int \tilde{\mathcal{P}}(\mathbf{r}_\perp, z, \omega, v) p_v d^3 v. \tag{5.27}$$

To calculate the analytical expression from Eq. (5.27), the Gaussian distribution $p_v \propto \exp[-mv_i^2/2k_BT]$ is approximated by the corresponding Lorentzian distribution $\mathcal{L}_v = \dfrac{a}{\pi(a^2 + v_i^2)}$ where $a \propto \sqrt{\dfrac{k_BT}{m}}$ [49]. The proportionality constant for a is obtained using the numerical curve fitting and is found to be close to 0.76. The final expression for the average macroscopic polarization can be written as

$$\tilde{\mathcal{P}}(\mathbf{r}_\perp, z, \omega) = 2\mathcal{N} \sum_{n,m} \frac{\mathrm{i} d_{nm}^2 \tilde{\mathcal{E}}(\mathbf{q}, z, \omega) \rho_{mm}}{2\hbar \left[\mathrm{i}(\Delta_{nm} + \omega) + \frac{\gamma}{2} + a f(\mathbf{r}_\perp, z) \right]}, \tag{5.28}$$

where the function $f(\mathbf{r}_\perp, z)$ reads

$$f(\mathbf{r}_\perp, z) = \frac{k(x+y)}{\bar{z}} + \frac{\ell(x-y)}{x^2+y^2} - \frac{(|\ell|+1) z_R}{z^2 + z_R^2} - \frac{k(x^2+y^2)}{2\bar{z}^2} \frac{(z^2 - z_R^2)}{z^2} + k. \tag{5.29}$$

From Eq. (5.28), it is clear that the effect of the temperature shows up as the broadening of the peak width γ by a factor $af(\mathbf{r}_\perp, z)$, where ka is the leading-order term. This leading term results in lowering the finesse of the frequency comb and results in lower efficiency of the quantum memory [49]. Other sub-leading terms in the broadening are ℓ-dependent and position-dependent due to the transverse profile of the field. The ℓ and position dependence of these terms will yield different efficiencies for different LG-modes, which will affect the fidelity of the quantum memory.

To study the effect of the Doppler shift δ_{LG} due to the transverse profile of light, we numerically solve the dynamical equations for the atomic coherence [Eq. (5.4)] and the electric field [Eq. (5.5)] by replacing $\left(i\Delta_{nm} + \dfrac{\gamma}{2}\right)$ with $\left(i\Delta_{nm} + \dfrac{\gamma}{2} + af(\mathbf{r}_\perp, z)\right)$ in Eq. (5.5). The variation of the optimized efficiency and the corresponding fidelity with the temperature for the ideal comb are shown in Fig. 5.4(b). In this figure,

we consider an ideal comb with nine teeth and tooth spacing $\Delta = 400$MHz. The peak width $\gamma = 5$ MHz. We see that the efficiency of the quantum memory drops as we increase the temperature falling below 10% for $T = 20$ K. However, the fidelity appears to be unaffected. This shows that the contribution from the ka term is much stronger than the contribution from the sub-leading terms in the Doppler shift. There is no direct relationship between the temperature and the optimized number density. The change in the optimized number density upon varying the temperature is negligible.

5.3.3 Factors affecting the polarization storage

Unlike the LG modes, polarization states of light do not depend on the spatial coordinates as long as the transverse plane is well defined. Therefore, the non homogeneity in the number density has very little effect on polarization storage. However, factors such as unequal $\mathcal{D}$ propagators and the non overlapping frequency combs corresponding to two orthogonal polarizations can affect the quality of the quantum memory. Here we will discuss some of those factors and study their effects. For simplicity, we will assume $\mathcal{G} = 0$ throughout this section, since most of the real systems exhibit this property.

The most common factor that can affect the quality of the quantum memory for polarization states is the unequal $\mathcal{D}$ propagators, i.e., $\mathcal{D}^+ \neq \mathcal{D}^-$. This will result in different echo times and efficiencies for the two orthogonal polarizations. By choosing a wave plate appropriately, one can compensate for the unequal storage times for the two polarizations. However, the different efficiencies of the two polarization components can affect the fidelity of the output polarization states. This can be compensated by choosing the mean frequency of light ω_L lying exactly in the middle of the two combs or by selectively absorbing light corresponding to a particular polarization, which will result in overall lower efficiency but higher fidelity.

In some cases, even if the frequency combs corresponding to two polarizations are identical, they might be displaced with respect to each other [Fig. 5.5(a)]. This factor can also adversely affect the storage of polarization states. In such cases, the

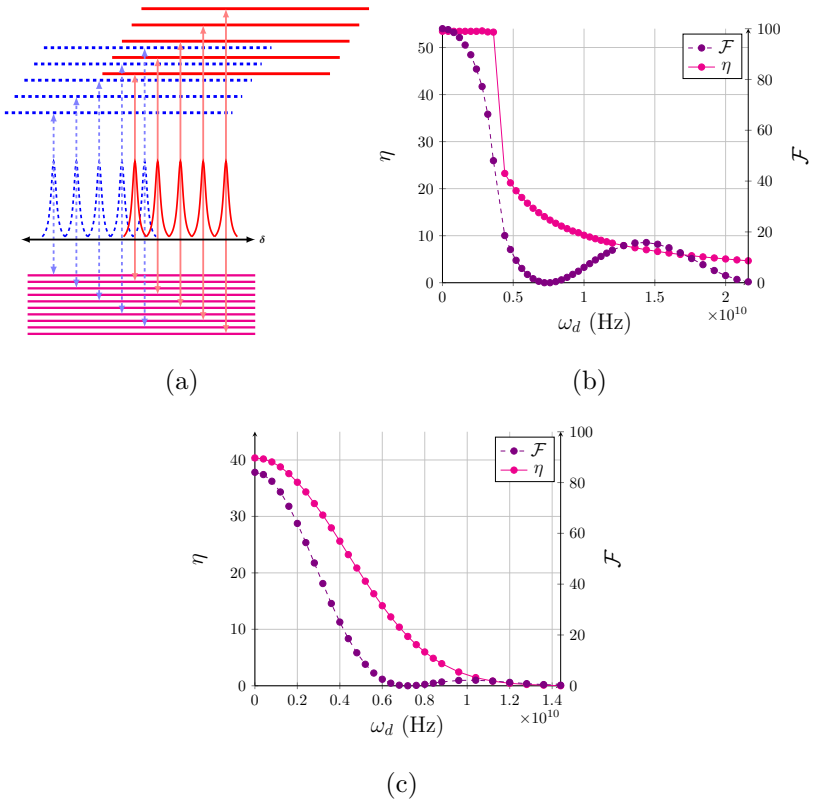

Figure 5.5: Storing polarization in I-AFC. (b) Storing plarization states using I-AFC. The two orthogonal polarization components couple separately to two non-overlapping frequency combs (red and blue) according to the transition selection rule $\Delta m = \pm 1$. (b) Variation of the optimized efficiency (η) w.r.t the input width and the corresponding fidelity ($\mathcal{F}$) as a function of separation between two combs (ω_d). (c) Variation of the storage efficiency (η) and the corresponding fidelity ($\mathcal{F}$) as a function of separation between two combs at a fixed input width of 2.4 GHz. Both frequency combs consist of 11 peaks with fixed comb spacing of 400 MHz and peak width 5 MHz. Here the input field is taken as $\mathcal{E}(0,\omega) = e^{-\omega^2/(2b^2)}$.

photon echoes for both polarizations occur at the same time, but an additional phase is attributed to them due to the shifted combs. This can be understood as follows: consider a comb shifted by $\pm\omega_d/2$ so that the detuning Δ_{nm} becomes $\rightarrow \Delta_{nm} \pm \omega_d/2$ for two combs. Solving Eqs. (4.38) and (4.39) in the frequency domain yields

$$\tilde{\mathcal{E}}_{\pm}(z,\omega_{\pm}) = e^{-\mathcal{D}^{\pm}z} e^{-\mathrm{i}\omega z/c} e^{\mp \mathrm{i}\omega_d z/2c} \tilde{\mathcal{E}}(0,\omega_{\pm}), \tag{5.30}$$

where $\tilde{\mathcal{E}}(0,\omega_{\pm})$ is the input electric field amplitude, $\omega_{\pm} = \omega \pm \omega_d/2$, and $\mathcal{D}$ is given

by

$$\mathcal{D}^{\pm}(\omega_{\pm}) = \sum_{n,m} \frac{g_{mm}}{\left[\mathrm{i}(\Delta_{nm} + \omega_{\pm}) + \frac{\gamma}{2}\right]} d_{nm}^2, \tag{5.31}$$

Hence, the output fields get equal and opposite phase $e^{\mp \mathrm{i}\omega_d z/2c}$ for the two combs. For a small shift ω_d, the fidelity drop is also small, whereas the drop increases as the value of ω_d increases.

We consider an I-AFC for polarization storage such that the frequency combs corresponding to two orthogonal polarizations are ideal but displaced with respect to each other by a magnitude ω_d. In Figs. 5.5(b) and 5.5(c), we plot the effect of the relative shift ω_d on the efficiency of the quantum memory and the fidelity of the output polarization state with respect to the input state. In these results, each of the frequency comb has eleven teeth with comb spacing $\Delta = 400$ MHz and peak width $\gamma = 5$ MHz. Hence, the total size of each comb is 4 GHz. These parameters are close to the $6s_{1/2} \leftrightarrow 8p_{3/2}$ transition in the Cs atom.

Here we consider two cases to study the effect of ω_d. In the first case, the intensity is optimized over the spectral width and the mean frequency of the incoming light and the corresponding fidelity is obtained as shown in Fig. 5.5(b). From this figure, we can see that the efficiency η is close to 54% when the two combs are perfectly overlapping. This is the maximum efficiency that can be achieved in I-AFC for forward propagating modes. This feature persists as long as the separation between the two combs is $\omega_d < 4$ GHz. After that point the efficiency starts to decrease. Interestingly, the drop in the efficiency is sharp. The value of η drops from $\sim 54\%$ at $\omega_d = 3.6$ GHz to below 24% at $\omega_d = 4.4$ GHz. On the other hand, the fidelity $\mathcal{F}$ shows a smooth behaviour as we increase ω_d. It starts with fidelity $\mathcal{F} = 100\%$ at $\omega_d = 0$ and shows damped oscillations as we increase ω_d.

In the second case, the optimization is done over the mean frequency of the input while keeping the spectral width of the input to be fixed [see Fig. 5.5(c)]. In Fig. 5.5(c) the input width is fixed at 2.5 GHz. Contrary to the previous case, here we can see a smooth variation in the efficiency as we increase ω_d. However, since the spectral width is fixed, the efficiency $\eta \sim 40\%$ at $\omega_d = 0$ GHz which is considerably lower than the maximum possible, i.e., 54%. Similarly, the fidelity $\mathcal{F} \sim 84\%$ at

$\omega_d = 0$.

Apart from these factors, temperature may also affect the storage efficiency and fidelity. However, those effects are generally independent of the polarization and affect only the overall efficiency, not the fidelity. In conclusion, the I-AFC-based quantum memory for VV states of light is robust and efficient against prominent environmental factors.

5.4 I-AFC in Cesium and Rubidium atoms

In this section we show that the Cesium and Rubidium atoms can be a feasible system to store both the polarization as well as OAM modes of light. Hence, these atoms are suitable for storing VV states of light.

We consider the $6s_{1/2} \leftrightarrow 8p_{3/2}$ transitions for Cs atoms and the $5s_{1/2} \leftrightarrow 6p_{3/2}$ transition for Rb atoms. In both the atoms, the atomic transitions are such that only one of the transition dipole moments, d^{+}_{nm} or d^{-}_{nm}, is nonzero, thus giving $\mathcal{G}(\omega) = 0$, which results in an independent propagation of the two polarization components. In both atoms, the frequency combs are not uniform, and the combs corresponding to $\Delta m = \pm 1$ are shifted with respect to each other [see Figs. 5.6(a) and 5.6(b)].

In Fig. 5.6(c) (Cs) and 5.6(d) (Rb), we show numerically obtained photon echoes for the polarization storage. The optimized fidelity and efficiency $(\mathcal{F}, \eta)$ for the Cs and Rb atoms are found to be $(88.23\%,\ 41.3\%)$ and $(87.46\%,\ 41.16\%)$, respectively. Since the $\mathcal{D}^{\pm}(\omega)$ propagators are not identical for both Cs and Rb atoms, the efficiency and fidelity in these cases are lower than in the ideal cases. Similarly, we observe the rephasing of the LG modes in Cs and Rb atoms. The optimized parameters, $(\mathcal{F}, \eta)$ in this case are found to be $(98.7\%,\ 51.96\%)$ for Cs and $(97.91\%,\ 51.84\%)$ for the Rb atoms, and the photon-echo plots are similar to Fig. 5.2.

We also show the effects of non-homogeneous number density on the OAM storage in the case of Cs and Rb atoms in Fig. 5.7(a), where $\mathcal{N}'(\mathbf{r}_\perp) = \mathcal{N}\exp[-(x^2+y^2)/2w_0'^2]$, with $w_0' = 0.71w_0$. It is clear that the Cs and Rb atoms show a similar drop in

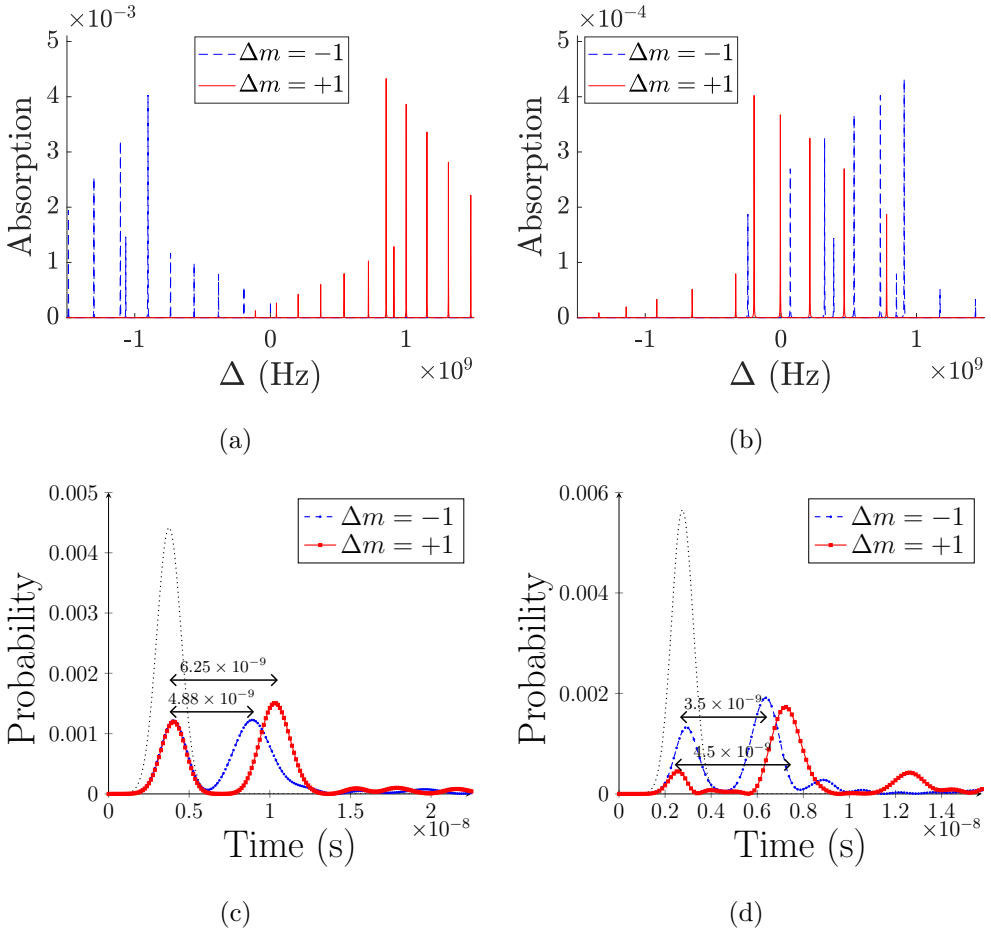

Figure 5.6: I-AFC in Cs and Rb atoms. In (a) and (b) we plot the frequency combs in the Cs and Rb atoms. Here $6s_{1/2} \leftrightarrow 8p_{3/2}$ and $5s_{1/2} \leftrightarrow 6p_{3/2}$ transitions are considered for Cs and Rb atoms, respectively. The degeneracy is lifted by applying external magnetic field of strength 0.05T and 0.06T, respectively, for the two cases. In (c) and (d) we plot the photon-echo corresponding to $\Delta m = +1$ and $\Delta m = -1$ transitions in Cs and Rb atoms respectively. The black (dotted) curve shows the corresponding input field in each case.

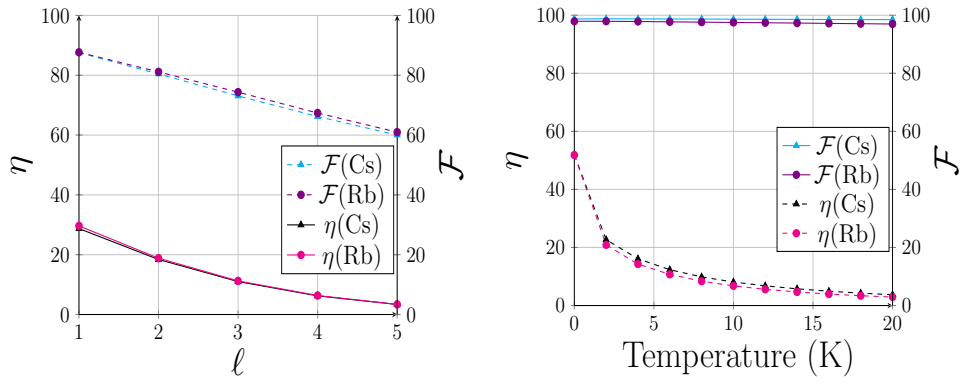

(a) (b)

Figure 5.7: Effect of non-homogeneous number density and temperature on OAM storage. (a) Efficiency (η) and the corresponding fidelity ($\mathcal{F}$) as a function of ℓ value for Cs and Rb atoms for the input state $|\ell\rangle$. (b) Efficiency and the corresponding fidelity in Cs and Rb atoms as a function of temperature for the OAM state $(|1\rangle + |-1\rangle)/\sqrt{2}$.

the efficiency and fidelity as in the ideal case discussed in Sec. 5.3.1 [Fig. 5.4(a)]. Fig. 5.7(b) shows the effect of the temperature on storing OAM modes in Cs and Rb, and the results are similar to those of an ideal comb [see Fig. 5.4(b)].

The atomic number densities ($\mathcal{N}$) for Cs and Rb atoms in the above calculations are taken to be $\sim 10^{18}$ m^{-3}, respectively, and the length of the cell is taken to be 5 cm [126]. These parameters are feasible at low temperatures ($T \sim 100$ μK) in the magneto-optical traps [132, 133, 134, 135]. Since Cesium and Rubidium atoms are capable of storing both the polarization and OAM modes, we expect them to store the VV beams.

Chapter 6

Quantum memory using single atom coupled to a cavity

The typical quantum memory protocols use a large ensemble of atoms or bulk materials to store photons. To gain scalability and practical advantage in quantum information processing, many efforts are being devoted towards integrated photonic chips [66, 67, 68, 69, 136, 137, 138, 139]. On-chip single photon sources, on-chip beamsplitters, and on-chip photon detectors are already available on integrated platform [70, 71, 72, 73, 74], while on-chip quantum memory is still a work in progress and is highly sought after device [75, 76]. Atomic ensemble-based quantum memories pose challenges for their on-chip integration. So far, only the AFC-based quantum memory protocol has been extended for on-chip implementation [75, 76]. Further, the Raman quantum memory protocol has been extended to a single-atom level, which can potentially be used on integrated photonic chips [123].

The conventional I-AFC-based quantum memory scheme also uses an ensemble of atoms to store single photons. However, since each atom in I-AFC contains a frequency comb, it can be argued that a single atom can store photons provided the atom and light couple strongly. In principle, one can use a single-mode optical cavity to tune the coupling between the atom and the photons and realize quantum memory using a single atom. In this chapter, we explore this feasibility and show that, with a proper choice of atom-cavity parameters, one can realize an efficient

quantum memory using a single atom containing an I-AFC coupled to an optical cavity [77].

Considering the cavity as a tool to store single photons, one might think of using just an empty cavity with high quality factor to get storage. However, this won't be useful as it will not provide any control over the storage time, and the input photon will not come out at a fixed time. Coupling the atom with I-AFC gives us a predetermined echo-time along with control over the storage times.

We show that this joint single-atom-cavity setup results in a photon-echo, similar to the I-AFC-based quantum memory protocol [49]. The efficiency of storing light in this setup depends on the finesse of the optical cavity and the quality of the frequency comb. Using this setup, we can also achieve robust and efficient storage for polarization and time-bin qubits. As examples, we show that Cesium and Rubidium atoms coupled to nanophotonic waveguide cavities can serve as promising candidates for implementing this quantum memory protocol.

In principle, the efficiency of this protocol can reach up to 100%, whereas in the AFC and I-AFC protocols, the maximum efficiency in the forward propagation can only be 54%. This is because, unlike in the bulk AFC and I-AFC protocols, the re-absorption of the photon in the re-emission process is eliminated by keeping the atom-cavity setup in the Purcell regime and using only one atom for storing the light.

One of the most significant advantages of this scheme is that it provides a possible realization of on-chip quantum memory. Furthermore, since our protocol requires only a frequency comb coupled to a cavity, it can also be implemented using the quantum dots inside a cavity [140, 141, 142, 143]. On-demand single-photon sources have already been realized using quantum dots [144, 145, 70, 72]. Combining these two elements can pave the way for efficient on-chip photonic quantum computation.

We start with discussing the dynamics of a single atom containing I-AFC coupled to a cavity, and how it can be used to store single photons. We also discuss the parameters that affect the storage and the implementation of this protocol using the Rb and Cs atom.

6.1 Dynamics of single-atom consisting of I-AFC coupled to a cavity

Consider an atom that contains a frequency comb, coupled to a high finesse single-mode optical cavity [Fig. 6.1(a)]. The Hamiltonian for such an atom-cavity system consists of three parts, the free Hamiltonian of the single-mode cavity, the free Hamiltonian of the atom, and the interaction between the two systems, which reads [77]

$$\begin{aligned} H =& H_{\mathrm{c}} + H_{\mathrm{a}} + H_{\mathrm{int}} \\ =& \hbar\omega_c \hat{a}^\dagger \hat{a} + \sum_{n=1}^{N} \hbar\omega_n^e \left|e_n\right\rangle\!\left\langle e_n\right| + \sum_{n=1}^{N} \hbar\omega_n^g \left|g_n\right\rangle\!\left\langle g_n\right| - \hbar\left[\sum_n g_n \left|e_n\right\rangle\!\left\langle g_n\right| \hat{a} + \sum_n g_n^* \left|g_n\right\rangle\!\left\langle e_n\right| \hat{a}^\dagger\right], \end{aligned} \tag{6.1}$$

where we have considered the atom with N number of ground states $\{|g_n\rangle\}$ and N number of excited states $\{|e_n\rangle\}$. For simplicity, we assume that the transition is allowed only between $|e_n\rangle \leftrightarrow |g_n\rangle$ for all n with the coupling strength $g_n = \frac{d_n}{\hbar}\sqrt{\frac{\hbar\omega_c}{2\epsilon_0 V}}$. d_n is the transition dipole moment for the transition $|g_n\rangle \leftrightarrow |e_n\rangle$, and ω_c is the resonance frequency of the cavity. $\hat{a}$ is the photon annihilation operator for the cavity mode.

The dynamical equations for the cavity field operator $\hat{a}$ and the atomic lowering operator $\sigma_n^- \equiv |g_n\rangle\langle e_n|$ for a dipole allowed transition $|g_n\rangle \leftrightarrow |e_n\rangle$ using the input-output formalism as discussed in Sec. 3.3 read

$$\frac{\mathrm{d}\hat{a}}{\mathrm{d}t} = -i\omega_c\hat{a} + i\sum_{n,m} g_n^*\sigma_n^- - \frac{\kappa}{2}\hat{a} - \sqrt{\kappa}\hat{a}_{\mathrm{in}}, \tag{6.2}$$

$$\frac{\mathrm{d}\sigma_n^-}{\mathrm{d}t} = -\mathrm{i}(\omega_n^e - \omega_m^g)\sigma_n^- + \mathrm{i}g_n(\sigma_{nn}^g - \sigma_{nn}^e)\hat{a} - \frac{\gamma}{2}\sigma_n^-, \tag{6.3}$$

$$\sqrt{\kappa}\ \hat{a}(t) = \hat{a}_{\mathrm{out}}(t) - \hat{a}_{\mathrm{in}}(t). \tag{6.4}$$

Here, $\sigma_{nn}^g = |g_n\rangle\langle g_n|$, $\sigma_{nn}^e = |e_n\rangle\langle e_n|$, γ is the spontaneous decay rate of the atom in free space, and κ is the decay rate of the cavity field.

To solve equations (6.2) to (6.4), we apply the low intensity approximation ($\langle \hat{a}^\dagger{}_{\mathrm{in}}\hat{a}_{\mathrm{in}}\rangle \lesssim 1$) which gives $\sigma_{nn}^e \approx 0$ [146] and introduce the following transformations to go into the rotating frame with respect to the mean frequency of the

input field, ω_L,

$$\hat{a} \to \tilde{\hat{a}} e^{-i\omega_L t}, \qquad \hat{a}_{\text{in}} \to \tilde{\hat{a}}_{\text{in}} e^{-i\omega_L t}, \qquad \sigma_n^- \to \tilde{\sigma}_n^- e^{-i\omega_L t}, \tag{6.5}$$

Then, Eqs. (6.2) to (6.4) can be written as

$$\frac{\mathrm{d}\tilde{\hat{a}}}{\mathrm{d}t} = -i\Delta_c \tilde{\hat{a}} + i\sum_n g_n^* \tilde{\sigma}_n^- - \frac{\kappa}{2}\tilde{\hat{a}} - \sqrt{\kappa}\tilde{\hat{a}}_{\text{in}}, \tag{6.6}$$

$$\frac{\mathrm{d}\tilde{\sigma}_n^-}{\mathrm{d}t} = -i\Big(\delta_n - i\frac{\gamma}{2}\Big)\tilde{\sigma}_n^- + \mathrm{i}g_n\sigma_{nn}^g\tilde{\hat{a}}, \tag{6.7}$$

$$\tilde{\hat{a}}_{\text{out}}(t) = \sqrt{\kappa}\ \tilde{\hat{a}} + \tilde{\hat{a}}_{\text{in}}(t), \tag{6.8}$$

where the detunings with the input light are defined as $\Delta_c = \omega_c - \omega_L$, $\delta_n = (\omega_n^e - \omega_n^g) - \omega_L$ and $\tilde{\hat{a}}, \tilde{\sigma}_n^-$ are in the rotating frame. Next, we take the Fourier transform of Eqs. (6.6)-(6.8) ($t \to \omega$). The Fourier Transform of Eq. (6.7) gives

$$\tilde{\sigma}_n^-(\omega) = \frac{\mathrm{i}g_n\sigma_{nn}^g}{\Big[\mathrm{i}(\omega+\delta_n) + \frac{\gamma}{2}\Big]}\tilde{\hat{a}}(\omega). \tag{6.9}$$

Taking the Fourier transform of Eq. (6.6) w.r.t t and using Eq. (6.9), we get

$$\tilde{\hat{a}}(\omega) = -\frac{\sqrt{\kappa}}{\left[i(\omega+\Delta_c) + \sum_n \dfrac{\sigma_{nn}^g |g_n|^2}{\Big[i(\omega+\delta_n)+\frac{\gamma}{2}\Big]} + \dfrac{\kappa}{2}\right]}\tilde{\hat{a}}_{in}(\omega). \tag{6.10}$$

Finally, taking the Fourier transform of Eq. (6.8) and using Eq. (6.10) gives the following expression for the output field in frequency domain

$$\tilde{\hat{a}}_{\text{out}}(\omega) = \left[1 - \frac{\kappa}{\mathrm{i}(\omega+\Delta_c) + \mathcal{D}(\omega) + \frac{\kappa}{2}}\right]\tilde{\hat{a}}_{\text{in}}(\omega), \tag{6.11}$$

where

$$\mathcal{D}(\omega) = \sum_n \frac{\sigma_{nn}^g |g_n|^2}{\Big[i(\omega+\delta_n)+\frac{\gamma}{2}\Big]}. \tag{6.12}$$

The inverse Fourier-transform of Eq. (6.11) yields the output field in time $\hat{a}_{\text{out}}(t)$ [103].

In order for this atom-cavity setup to qualify for a quantum memory, there must be a delay between the input and output light. In Fig. 6.1(b), we plot the output intensity $I_{\text{out}} = \left\langle \hat{a}_{\text{out}}^\dagger(t)\hat{a}_{\text{out}}(t) \right\rangle$ as a function of time which we get by solving

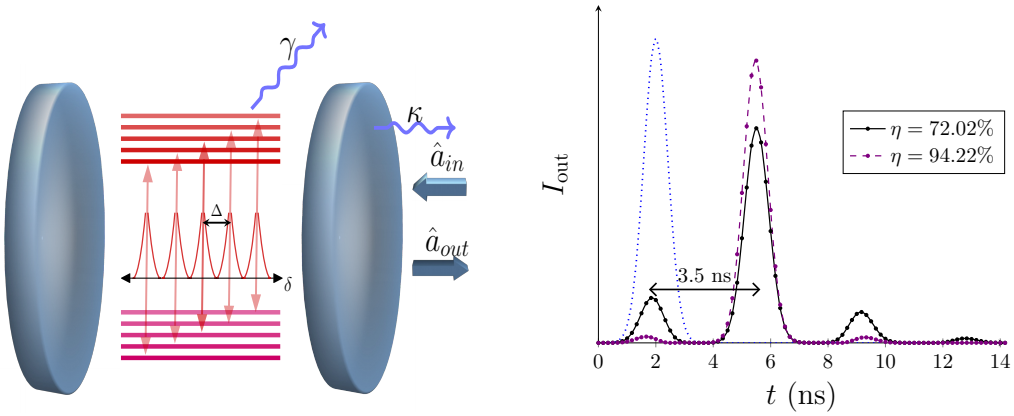

(a) (b)

Figure 6.1: (a) Schematic diagram of an I-AFC inside a cavity. Here, the I-AFC interacts with a single cavity mode with a decay rate κ. $\hat{a}_{\text{in}}$ and $\hat{a}_{\text{out}}$ represent the input and output field mode operators. γ is the spontaneous decay rate of the atom into free space. (b) Photon-echo after a delay of 3.5 ns for an ideal I-AFC coupled to a cavity with uniform comb spacing of $\Delta = 2\pi \times 300$ MHz, tooth width $\gamma = 7.5$ MHz, and cavity detuning $\Delta_c = 0$. The input field in Eq. (6.11) is a Gaussian pulse given by $e^{-\omega^2/(2b^2)}$ with $b = 2\pi \times 270$ MHz. The two photon echoes shown by dashed purple and solid black curve correspond to the cavity decay rates of 7 and 4 GHz, respectively, with corresponding efficiencies of 94.22% and 72.02%, respectively. Here, I_{out} represents the rate of photons in the output field (ns^{-1}), which is related to the input field through Eq. (6.11). Here the third peak coming at ~ 9 ns corresponds to the second photon-echo. The blue dotted curve shows the corresponding input field intensity, $I_{\text{in}} = \left\langle \hat{a}^{\dagger}_{\text{in}}(t)\hat{a}_{\text{in}}(t) \right\rangle$.

Eq. (6.11) numerically. Here, we consider a Gaussian input pulse of spectral width $2\pi \times 270$ MHz. The I-AFC associated with the atom has seven teeth with uniform comb spacing $\Delta = 2\pi \times 300$ MHz, tooth width $\gamma = 7.5$ MHz, and the detuning $\Delta_c = 0$. The solid curve and the dashed curve in this figure correspond to two different values of the cavity decay rates κ. In this figure, we can clearly see that the first prominent output pulse of light is at time $t = 2$ ns, which is due to the immediate reflection from the cavity. The second prominent output pulse occurs at $t \sim 5.5$ ns, which is due to the emission from the cavity. There is a delay of 3.5 ns which is approximately $2\pi/\Delta$ due to the interaction of light with the setup. Hence,

the atom-cavity setup behaves like an I-AFC.

6.2 Factors affecting the quality of quantum memory

Eqs. (6.11) and (6.12) suggest that the output field from the atom-cavity setup also depends on the cavity parameters g_n, κ, and Δ_c. Hence, they can affect the quality of the memory. In this section, we discuss the factors that affect the storage. The storage efficiency in this scheme is defined as

$$\eta = \frac{\int_{\pi/\Delta}^{3\pi/\Delta} \left\langle \hat{a}^{\dagger}_{\text{out}}(t)\hat{a}_{\text{out}}(t) \right\rangle \, dt}{\int \left\langle \hat{a}^{\dagger}_{\text{in}}(t)\hat{a}_{\text{in}}(t) \right\rangle \, dt}. \tag{6.13}$$

which is the ratio of the intensity of the output field mode in the first echo to the total intensity of the input field.

In Fig. 6.2(a), we plot the variation of the efficiency η as a function of the cavity detuning Δ_c while keeping g' and κ constant. As expected, it shows a drop in the efficiency as the cavity detuning increases. The efficiency also depends on the comb finesse $\mathcal{F} \equiv \Delta/\gamma$. In Fig. 6.2(b), we plot the efficiency as a function of comb finesse for the ideal comb with fixed comb spacing, $\Delta = 2\pi \times 300$ MHz by changing the peak width γ while keeping the cavity parameters fixed. This plot shows that the efficiency saturates to $\sim 100\%$ asymptotically for asymptotic values of the finesse.

Since the storage time is directly controlled by the comb spacing Δ, instead of using the spin state transfer to increase the storage time, an alternate method would be to decrease the comb spacing Δ which can be achieved by lowering the applied magnetic field strength. However, reducing Δ reduces the comb finesse ($\mathcal{F} = \Delta/\gamma$), resulting in lower storage efficiencies. In order to preserve the efficiency while decreasing Δ, one can try to preserve $\mathcal{F}$ by reducing the atomic decay rate γ, or try to find atomic systems where γ is small.

For an ideal I-AFC, since all the peaks are identical, i.e., $d_n \equiv d$, we may write $g_n = g$. We define $g' = g\sqrt{\sigma^g_{nn}}$ as the effective coupling constant and define the

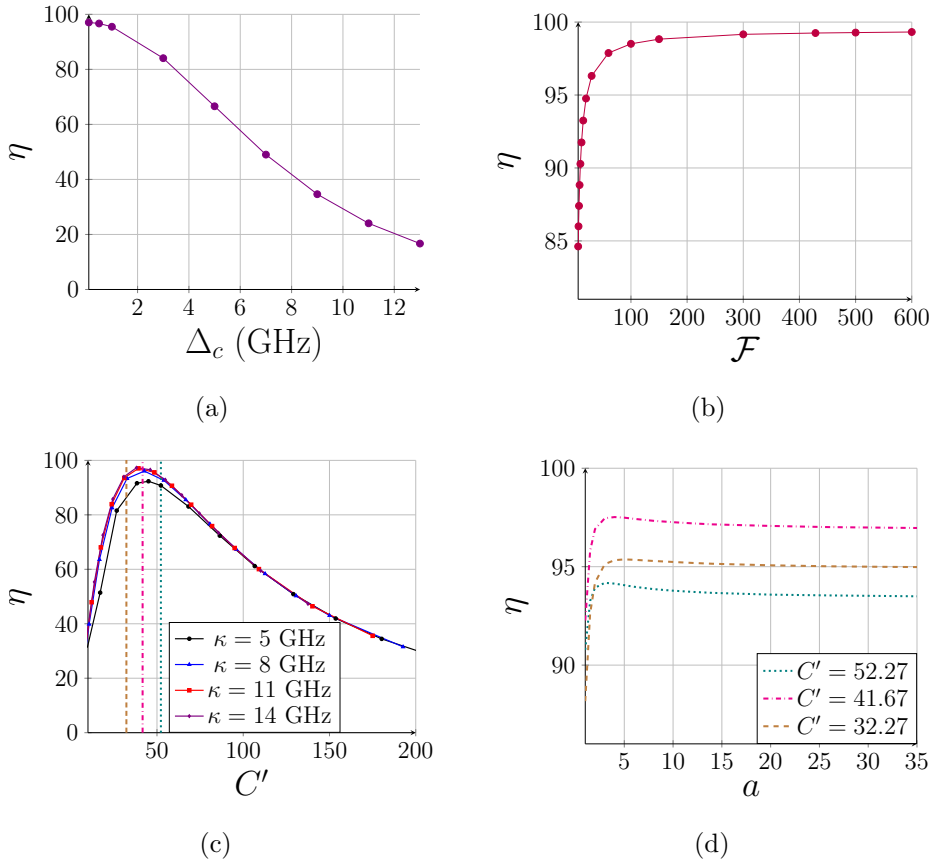

Figure 6.2: Effect of various parameters on the efficiency (η) of quantum memory in the single-atom-cavity setup for an ideal comb. In (a) and (b), we plot the variation of η as a function of the cavity detuning $\Delta_c = \omega_c - \omega_L$ and the comb finesse ($\mathcal{F}$), respectively for $(g', \kappa) = (1.8, 11)$ GHz with uniform comb spacing $\Delta = 2\pi \times 300$ MHz. (c) shows the plot of the variation of η as a function of cooperativity, $C' = g'^2/(\kappa\gamma)$ for different values of κ. (d) shows the variation of η as a function of κ given in terms of the parameter a such that $\kappa = a \times 5$ GHz, for fixed value of cooperativities as shown by the vertical lines in (c).

cooperativity parameter for the atom-cavity system as $C' = g'^2/(\kappa\gamma)$. In order to understand the effect of the cavity parameters g' and κ on the efficiency, in Fig. 6.2(c), we plot the variation of η as a function of the cooperativity C' for various values of κ and keeping $\Delta_c = 0$. Fig. 6.2(c) shows that the efficiency first increases, reaches an optimum value, and then starts decreasing, and there exists an optimum value of C' for every given value of κ, which maximizes the efficiency. The maximum efficiencies are obtained in the range $C' \sim$ 35-45 for all the values of κ. Note that in the case of the ensemble based quantum memories, the efficiency shows

a similar behaviour with respect to the optical depth and absorption coefficient [49]. Later, we will show the relation between the cooperativity and the absorption by the atom-cavity setup which will explain the apparent resemblance between the two.

An interesting observation from Fig. 6.2(c) is that for a fixed value of C' the efficiency increases as we increase κ. In Fig. 6.2(d), we plot the efficiency as a function of κ while keeping C' fixed. This is achieved by scaling the cavity decay rate κ by a number a and scaling g' by a factor $\sqrt{a}$ so that $C' = g'^2/\kappa\gamma$ remains invariant. Fig. 6.2(d) shows the variation of the efficiency with respect to the parameter a for the three different values of cooperativities corresponding to Fig. 6.2(c). This shows that for a fixed value of cooperativity C', the efficiency increases with increasing κ and then gets saturated to a constant value. The plot shows a slight dip around $a = 3$ before reaching the saturation. This is because the width of the input pulse is kept fixed while the parameter a varies. Optimizing the efficiency over the input width will result in the saturation of the efficiency without this slight dip. Thus, a combination of the parameters C' and κ determines the optimized efficiency.

6.3 Absorption by atom-cavity system

So far, we have studied numerically the effect of the various parameters on the efficiency of the quantum memory. Here, we discuss the absorption by atom-cavity system. While solving for the output field in Eq. (6.11), we assumed that there is a negligible absorption of the input field by the atom, i.e., ($\sigma^e_{nn} \sim 0$), but the efficiency of the storage by this system is still high. To understand this, we consider the expression for the susceptibility χ of the joint atom-cavity system, which reads [147]

$$\chi = \sqrt{\frac{2V}{\epsilon_0 \hbar \omega_c}} \frac{\langle P \rangle}{\langle \hat{a} \rangle}, \tag{6.14}$$

where $P = \frac{1}{V}\sum_n d_n^* \sigma_n^-$ is the atomic polarization of the atom exhibiting the I-AFC and V is the cavity mode volume. The above expression for susceptibility is equivalent to the classical field susceptibility $\chi_e = \frac{\langle P \rangle}{\epsilon_0 \mathcal{E}}$, where the classical field amplitude $\mathcal{E}$ being replaced by the expectation value of the $\hat{a}$ operator.

Substituting $\tilde{\sigma}_n^-$ from Eq. (6.9) and using Eq. (6.14) gives the following expression

for the joint susceptibility χ

$$\chi(\omega) = \frac{2\mathrm{i}}{\omega_c} \sum_n \frac{\sigma_{nn}^g |g_n|^2}{\left[i(\omega + \delta_n) + \frac{\gamma}{2}\right]}. \tag{6.15}$$

Further, using the definition of the Quality factor, $Q = \omega_c/\kappa$, it can be written as

$$\chi(\omega) = \frac{2\mathrm{i}}{Q} \sum_n \frac{\sigma_{nn}^g |g_n|^2/\kappa}{\left[i(\omega + \delta_n) + \frac{\gamma}{2}\right]}. \tag{6.16}$$

The imaginary part of χ gives the absorption coefficient for the atom-cavity system.

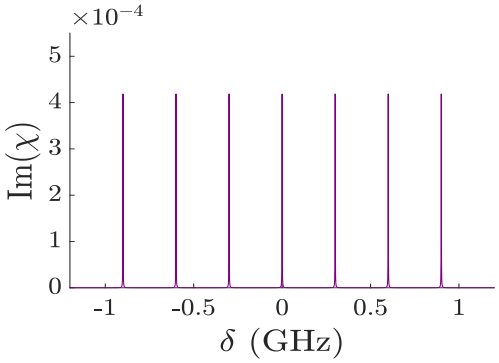

Figure 6.3: Plot for absorption of the joint atom-cavity system for an ideal frequency comb with uniform comb spacing $\Delta = 2\pi \times 300$ MHz, tooth width $\gamma = 7.5$ MHz, and cavity detuning $\Delta_c = 0$.

In Fig. 6.3, we plot the absorption for the I-AFC-cavity system. From this figure, we can see that the absorption profile of the joint atom-cavity system shows a comb like structure similar to the absorption profile in I-AFC. This comb like structure is responsible for the photon-echo, as shown in Fig. 6.1(b). Thus, the atom and the cavity together account for the photon storage, even though the absorption by the atom is negligible.

Moreover, as discussed earlier, Eq. (6.16) clearly shows the the direct relation between the absorption and the cooperativity parameter C'. This is similar to the dependence of the absorption in case of the conventional ensemble based protocol on the optical depth [49]. Hence, C' can be considered a parameter analogous to the optical depth in the ensemble based protocol which gives the optimized efficiencies for $C' \sim 35$–45. This eventually leads to the condition for obtaining the optimized efficiencies given by $\tau C' \gamma \sim 1$, where τ is the input pulse width and γ is the atomic decay rate.

Note that the width of the input pulse in the frequency domain, $\gamma_p \approx 1/\tau$ should be large enough to cover the frequency comb structure. In the atom-cavity setup, this puts another condition on the cavity decay rate κ, which should be comparable to the pulse width γ_p. In the above example of ideal comb, we have considered high value of cooperativity parameter, $C' \sim 35$–45 while keeping the large cavity decay width, $\kappa \sim$ GHz. It provides large enough spectral width for the input pulse. Further, for different echo times, we require different spectral widths of the input pulse and accordingly, the required value of C' will change. This can limit the spectral profile of the input pulse that can get into the cavity. One way to compensate for this is not to decrease the cavity linewidth while adjusting the cavity coupling strength g instead in order to get optimal efficiencies. In Sec 6.5, we discuss the possible implementation of this scheme with high coupling strengths and large enough cavity linewidth.

6.4 Storing polarization and time-bin qubits

The quantum memory protocol presented here can also be used to store polarization and time-bin photonic qubits. AFC and I-AFC-based quantum memories are known for storing time-bin qubits efficiently [43, 148, 61]. In time-multiplexing or time-bin qubits, a single photon is placed in a superposition of two time bins, say, an early time t and a later time $t + \tau$. Storing these qubits involves storing a single photon arriving at two different times. The corresponding photo-echo will occur at $t+2\pi/\Delta$ and $t + \tau + 2\pi/\Delta$. Since only one photon needs to be stored in this process, our scheme can easily achieve that task. Further, storing polarization states of light in I-AFC-based quantum memory was already been proposed in [51]. For storing polarization qubit, our aim is to store a single photon, which is in a superposition of two orthogonal polarizations. This can be achieved using the I-AFC-cavity setup with the single atom consisting of two overlapping frequency combs, which satisfy the selection rules corresponding to the two orthogonal polarizations, as discussed in the previous chapter. This results in an independent storage of the two polarization components [51]. Generally, the efficiency and the photon-echo time for the two polarizations can be different. By choosing the cavity parameters appropriately, one

can store arbitrary polarization in these systems [51].

Thus, we have shown that a single atom with an I-AFC coupled to an optical cavity can store photons efficiently. The results obtained here are also interesting from a fundamental point of view. We see that even though the I-AFC is necessary to store the photons in the atom-cavity system proposed here, the excitation probability of the atom is negligible. The interaction of the I-AFC with the cavity yields the comb like absorption profile of the joint atom-cavity system, which enables efficient quantum memory. In the following section, we present examples of systems capable of realizing this quantum memory protocol.

6.5 Realizing the quantum memory using Rb and Cs atoms

So far, we have discussed the photon storage assuming an ideal frequency comb with uniform comb spacing and the same peak height, which interacts with an optical cavity. However, if we consider realistic systems such as Rb and Cs atoms, the frequency combs obtained from them are usually non-uniform with unequal peak heights, which affects the storage process [49, 50]. In this section, we discuss the possibilities for experimental implementation of the single atom based quantum memory protocol in realistic systems such as Rb and Cs atoms coupled to a nanophotonic waveguide cavity and show that the current scheme can be implemented with the existing experimental techniques.

As discussed in Sec. 6.1, one of the requirements to achieve efficient quantum memory in I-AFC-cavity setup is a cavity with high coupling strength g of the order of GHz (see Fig. 6.2). This, in turn, requires a cavity with a low mode volume of the order of $(\sim \mu\text{m})^3$. Such strong coupling is difficult to achieve using the conventional Fabry-Pérot cavities, but can be achieved using the nano-cavities [149, 150] where the mode volume $V \sim \lambda^3$ have already been realized. Apart from this, the strong coupling has been realized in fiber-based Fabry-Pérot cavity [151] where the mirror surface of the cavity is designed on the optical fiber end faces. This tight confinement

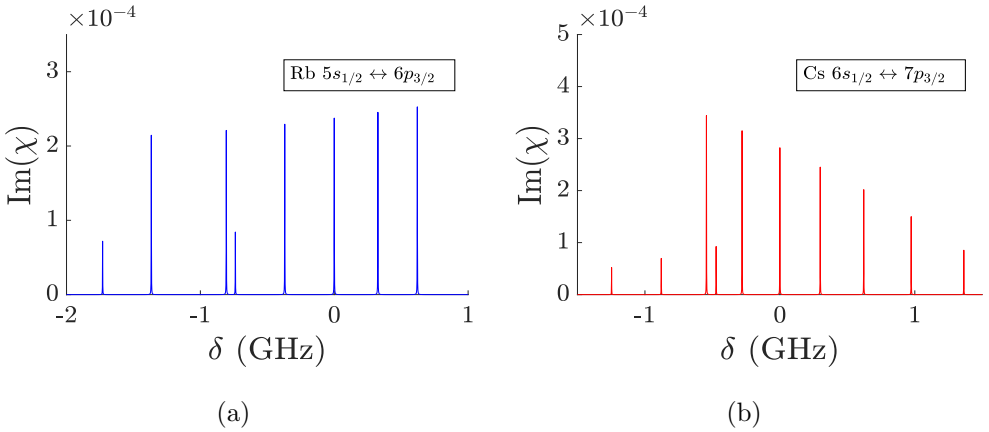

(a) (b)

Figure 6.4: (a) and (b) represent the frequency comb in Rb and Cs atoms for transitions between $5s_{1/2} \leftrightarrow 6p_{3/2}$ for Rb and $6s_{1/2} \leftrightarrow 7p_{3/2}$ for Cs. The applied magnetic field strength for Rb and Cs is taken to be 0.15 and 0.1 T, respectively.

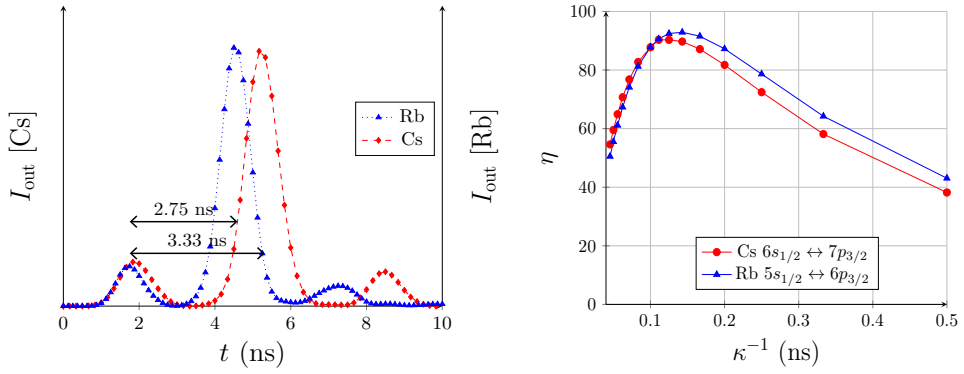

(a) (b)

Figure 6.5: (a) Photon-echo for the I-AFC in Rb and Cs atoms. (b) Variation of efficiency as a function of $1/\kappa$ in Rb and Cs atoms.

using nano-photonic cavities gives an additional advantage of potential integration with nano-photonics. Trapping in such low mode volumes results in the atom-cavity strong coupling of the order of $g \sim$ GHz along with the quality factor $Q = \omega_c/\kappa \sim 10^5$ [149].

Although the scheme presented here is applicable to a large class of atoms, molecules and quantum dots, here we consider Cs and Rb atoms as examples to realize this quantum memory protocol. The parameters such as the atomic transitions used in the Cs and Rb atoms, the wavelength, the applied magnetic field

Atom	Transition	λ (nm)	B (T)	$V(\mu\text{m})^3$	κ (GHz)	Q
Rb [152]	$5s_{1/2} \leftrightarrow 6p_{3/2}$	420.3	0.15	20	~ 7	10^5
Cs [153]	$6s_{1/2} \leftrightarrow 7p_{3/2}$	455.66	0.1	20	~ 8	10^5

Table 6.1: Rb and Cs parameters used in numerical calculations. λ is the wavelength of transition B is the magnetic field used in obtaining I-AFC. V, κ and Q are the mode volume, the decay rate, and the quality factor of the cavity, respectively.

strength and so on for the Rb and Cs atoms used for our calculations are given in Table 6.1. In Figs. 6.4(a) and 6.4(b), we plot the frequency comb obtained in the Rb and Cs atoms. Clearly, these frequency combs are not uniform in the comb spacing, nor do they have equal absorption peaks. In Fig. 6.5(a) we show the photon-echo from the Rb and Cs atoms calculated numerically by solving Eq. (6.11). The maximum efficiencies for the Rb and Cs atoms are found to be 92.9% and 90.36%, respectively, for the parameters specified in Table. 6.1.

Since in the case of the Cs and Rb atoms, each transition $|g_n\rangle \rightarrow |e_n\rangle$ constituting the frequency comb corresponds to a different value of the coupling constant g_n, it is difficult to study the behaviour of the efficiency with respect to the cooperativity parameter C'. However, we can consider the variation of the efficiency for Cs and Rb atoms as a function of $1/\kappa$ for fixed g_n and γ which essentially captures the behaviour of the efficiency as a function of the cooperativity. In Fig. 6.5(b), we plot the variation of the efficiency as a function of the $1/\kappa$ for Rb and Cs atoms. It is clear that the trend is similar to that of an ideal comb in Fig. 6.2(c) with maximum efficiency of $\sim$ 90%. The lower value of the efficiencies in the case of Rb and Cs atoms is due to the inherent non-uniformity present in the frequency combs. This non-uniformity is attributed to different values of the comb spacing Δ_n and the dipole matrix element d_n corresponding to the transition $|e_n\rangle \leftrightarrow |g_n\rangle$. Our calculations show that an efficient quantum memory using a single atom coupled to an optical cavity can be implemented using the current experimental techniques.

While solving the dynamics for an I-AFC coupled to a cavity, it is assumed that the single atom is at a fixed location. However, there might be an induced light shift when the atom is trapped using an optical dipole trap. Another factor that

can affect the protocol is the spatial inhomogeneous magnetic field. The induced light shift can change the detuning, δ_n of the concerned transition $|g_n\rangle \leftrightarrow |e_n\rangle$. Since the detuning of each transition in the frequency comb changes identically, the comb spacing remains the same, and the echo-time is not affected. On the other hand, the spatially inhomogeneous field will directly affect the comb spacing of the generated frequency comb. However, there will still be a photon-echo at time $2\pi/\Delta'$ where Δ' is the modified comb spacing due to the inhomogeneous magnetic field. To avoid such effects arising from trapping a single atom, one can choose quantum dots or defect centers with a frequency comb structure.

Part II

Chapter 7

Cascaded quantum systems and complete input-output theory

In chapter 3, we discussed the input-output formalism in the context of atom-cavity interactions which allows us to calculate the output field mode in terms of the input field mode upon its interaction with the atom-cavity system. It simply gives the output field amplitude as a function of time and the corresponding intensity. However, the standard input-output theory does not provide the exact state of the emitted output field. Further, the interaction of the input light pulse with a local quantum system may not always result in the emission of a single-mode output field. It can result in the scattering of the output field into multiple output field modes. Thus, we need a more general input-output theory that describes the dynamics of an input light pulse interacting with a local quantum system of interest and provides the full description quantum state of the propagating output field modes. The quantum system of interest here may be a cavity, an atom or an atom-cavity system in general.

In this chapter, we discuss the Kiilerich-Mølmer input-output (KMIO) formalism for quantum pulses interacting with a localized quantum system [79, 80]. This modified input-output formalism is an efficient tool to obtain the exact state of the output field once it interacts with a local quantum system. It is based on the concept of cascaded quantum systems, where the time-dependent input and output modes

are replaced by the virtual input and output cavities interacting with the quantum system of interest with complex time-dependent coupling strengths.

We start with discussing the theory of cascaded quantum system where the output from one quantum system is served as an input to another quantum system with a unidirectional coupling [154, 155, 156]. Subsequently, we discuss the KMIO formalism with quantum pulses.

7.1 Cascaded quantum systems

Consider a set of two quantum systems such that the output from system 1 is served as an input to system 2 while the reverse coupling from system 2 to 1 is not allowed, i.e., the flow of the input field is unidirectional, which is always from system 1 to 2. This is also known as the cascading the output from one quantum system to another, as shown in Fig. 7.1. These two quantum systems can be two cavities or two atoms or cavities coupled to atoms. To describe the dynamics of such cascaded quantum systems, we follow the approach by Gardiner as described in [154] and [156].

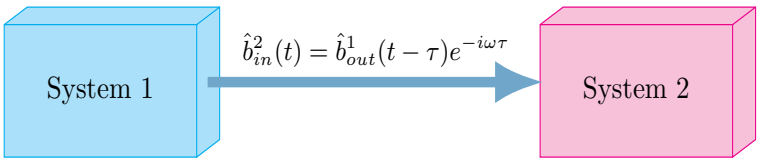

Figure 7.1: A set of two cascaded systems where output from system 1 drives the system 2, while the reverse coupling from system 2 to 1 is not allowed.

To begin with, we simply consider that the two identical systems are coupled to a common reservoir, such that the output from system 1 feeds as an input to system 2 placed at a distance $x = c\tau$ with τ being the propagation time of the field between

system 1 and 2. The Hamiltonian for such system can be written as[1] [154, 156]

$$\begin{aligned} H =& H_{S_1} + H_{S_2} + H_B + H_{I_1} + H_{I_2} \\ =& H_{S_T} + \int_{-\infty}^{\infty} d\omega \omega \hat{b}^\dagger(\omega)\hat{b}(\omega) + \mathrm{i}\int_{-\infty}^{\infty} d\omega \kappa_1(\omega)[\hat{b}^\dagger(\omega)\hat{c}_1 - \hat{c}_1^\dagger \hat{b}(\omega)] \\ &+ \mathrm{i}\int_{-\infty}^{\infty} d\omega \kappa_2(\omega)[\hat{b}^\dagger(\omega)\hat{c}_2 e^{-\mathrm{i}\omega\tau} - \hat{c}_2^\dagger \hat{b}(\omega) e^{\mathrm{i}\omega\tau}], \end{aligned} \tag{7.1}$$

where $H_{S_T} = H_{S_1} + H_{S_2}$ is the total system Hamiltonian with H_{S_1} and H_{S_2} being the free Hamiltonians for the two components or subsystems of the cascaded setup. $\hat{c}_1$ and $\hat{c}_2$ are arbitrary system operators corresponding to system 1 and 2, respectively. If the two components are cavities cascaded one after other, then $\hat{c}_1$ and $\hat{c}_2$ will simply correspond to the two cavity field mode operators. H_B is the bath Hamiltonian with $\hat{b}(\omega)$ and $\hat{b}^\dagger(\omega)$ being the bath operators satisfying $\left[\hat{b}(\omega), \hat{b}^\dagger(\omega')\right] = \delta(\omega - \omega')$. The terms H_{I_1} and H_{I_2} represents the coupling of the system operators $\hat{c}_1$ ($\hat{c}_2$) with the common bath with the corresponding coupling strengths $\kappa_1(\omega)$ and $\kappa_2(\omega)$, respectively. $\tau = x/c$ is the field propagation time between the two systems.

We can obtain the Heseinberg Langevin for the cascaded quantum system using the exact same approach as discussed in Sec. 3.3 of chapter 3. Using the Hamiltonian for the two cascaded systems given in Eq. (7.1), the dynamical equation for $b(\omega)$ reads

$$\dot{\hat{b}}(\omega) = -\mathrm{i}\omega\hat{b}(\omega) + \kappa_1(\omega)\hat{c}_1 + \kappa_2(\omega)\hat{c}_2 e^{-\mathrm{i}\omega\tau}, \tag{7.2}$$

Integrating this gives

$$\hat{b}(\omega) = e^{-\mathrm{i}\omega(t-t_0)} b_0(\omega) + \int_{t_0}^{t} dt' e^{-\mathrm{i}\omega(t-t')}\left(\kappa_1(\omega)\hat{c}_1(t) + \kappa_2(\omega)\hat{c}_2(t)e^{-\mathrm{i}\omega\tau}\right), \tag{7.3}$$

Invoking the Markov approximation, which assumes $\kappa_1(\omega)$ and $\kappa_2(\omega)$ to be independent of frequency over a narrow bandwidth of frequencies around the characteristic frequency Ω. This gives

$$\kappa_1(\Omega) = \sqrt{\frac{\gamma_1}{2\pi}},\ \kappa_2(\Omega) = \sqrt{\frac{\gamma_2}{2\pi}}, \tag{7.4}$$

while $\kappa_1(-\Omega) = \kappa_2(-\Omega) = 0$. This is a crucial step, since it breaks the reflection invariance as κ_1 and κ_2 for ngative frequency is 0.

[1] For simplicity, we consider $\hbar = 1$ hereafter.

Similarly, the dynamical equation for a general system operator $\hat{A}$ for this cascaded setup can be written as

$$\begin{aligned}\dot{\hat{A}} = -\mathrm{i}[A, H_{S_T}] + \int d\omega\ \kappa_1(\omega)\Big[\hat{b}^\dagger(\omega)\Big[\hat{A}, \hat{c}_1\Big] - \Big[\hat{A}, \hat{c}_1^\dagger\Big]\hat{b}(\omega)\Big] \\ + \int d\omega\ \kappa_2(\omega)\Big[\hat{b}^\dagger(\omega)\Big[\hat{A}, \hat{c}_2\Big]e^{-\mathrm{i}\omega\tau} - \Big[\hat{A}, \hat{c}_2^\dagger\Big]\hat{b}(\omega)e^{\mathrm{i}\omega\tau}\Big],\end{aligned} \tag{7.5}$$

Substituting $\hat{b}(\omega)$ from Eq. (7.3) and using Eq. (7.4) eventually gives the required equation of motion for A, which reads

$$\begin{aligned}\dot{\hat{A}} =& -\mathrm{i}[A, H_{S_T}] - [\hat{A}, \hat{c}_1^\dagger]\Big(\frac{\gamma_1}{2}\hat{c}_1 + \sqrt{\gamma_1}\hat{b}_{\mathrm{in}}(t)\Big) \\ &+ \Big(\frac{\gamma_1}{2}\hat{c}_1^\dagger + \sqrt{\gamma_1}\hat{b}_{\mathrm{in}}^\dagger(t)\Big)\Big[\hat{A}, \hat{c}_1\Big] - [\hat{A}, \hat{c}_2^\dagger]\Big(\frac{\gamma_2}{2}\hat{c}_2 + \sqrt{\gamma_1\gamma_2}\hat{c}_1(t-\tau) + \sqrt{\gamma_2}\hat{b}_{\mathrm{in}}(t-\tau)\Big) \\ &+ \Big(\frac{\gamma_2}{2}\hat{c}_2^\dagger + \sqrt{\gamma_1\gamma_2}\hat{c}_1^\dagger(t-\tau) + \sqrt{\gamma_2}\hat{b}_{\mathrm{in}}^\dagger(t-\tau)\Big)\Big[\hat{A}, \hat{c}_2\Big],\end{aligned} \tag{7.6}$$

where γ_1 and γ_2 now represent the decay rate of the two systems. Since the typical time scale of the dynamics are $\sim \gamma^{-1}$, hence for $\tau \ll \gamma^{-1}$, one can neglect the time delay τ. Thus, when the time delay $\tau \to 0$, the above equation simply becomes [154, 156]

$$\begin{aligned}\dot{\hat{A}} =& -\mathrm{i}[A, H_{S_T}] - [\hat{A}, \hat{c}_1^\dagger]\Big(\frac{\gamma_1}{2}\hat{c}_1 + \sqrt{\gamma_1}\hat{b}_{\mathrm{in}}\Big) \\ &+ \Big(\frac{\gamma_1}{2}\hat{c}_1^\dagger + \sqrt{\gamma_1}\hat{b}_{\mathrm{in}}^\dagger\Big)\Big[\hat{A}, \hat{c}_1\Big] - [\hat{A}, \hat{c}_2^\dagger]\Big(\frac{\gamma_2}{2}\hat{c}_2 + \sqrt{\gamma_1\gamma_2}\hat{c}_1 + \sqrt{\gamma_2}\hat{b}_{\mathrm{in}}\Big) \\ &+ \Big(\frac{\gamma_2}{2}\hat{c}_2^\dagger + \sqrt{\gamma_1\gamma_2}\hat{c}_1^\dagger + \sqrt{\gamma_2}\hat{b}_{\mathrm{in}}^\dagger\Big)\Big[\hat{A}, \hat{c}_2\Big].\end{aligned} \tag{7.7}$$

We note that if A is an operator belonging to the first system, then the terms $\big[A, c_2^\dagger\big]$ and $[A, c_2]$ in Eq. (7.7) vanish and the Langevin equation contains the terms corresponding to the first system only and reads

$$\dot{\hat{A}} = -\mathrm{i}\Big[\hat{A}, H_{S_T}\Big] - [\hat{A}, \hat{c}_1^\dagger]\Big(\frac{\gamma_1}{2}\hat{c}_1 + \sqrt{\gamma_1}\hat{b}_{\mathrm{in}}\Big) + \Big(\frac{\gamma_1}{2}\hat{c}_1^\dagger + \sqrt{\gamma_1}\hat{b}_{\mathrm{in}}^\dagger\Big)\Big[\hat{A}, \hat{c}_1\Big]. \tag{7.8}$$

This is similar to the the Langevin equation of motion as obtained for a single quantum system that interacts with a reservoir [Eq. (3.30)]. It clearly shows that there is no effect of system 2 on 1. However, if the operator A corresponds to system 2, then the Langevin equation contains non-zero terms proportional to $\hat{c}_1, \hat{c}_1^\dagger, \hat{c}_2, \hat{c}_2^\dagger$ and $\hat{b}_{\mathrm{in}}$. This shows the influence on system 2 due to system 1 and signifies the unidirectional flow of information from system 1 to 2 in a cascaded manner.

7.2 Effective Hamiltonian for cascaded quantum system

In order to reach Eq. (7.7), we started with the complete Hamiltonian of the two cascaded components and invoked a unidirectional coupling between the two components, which ensured that system 2 is driven by system 1 without any reverse coupling from system 2 to system 1. However, we can model the cascaded setup with two components as an effective single quantum system to make things simpler. Using this, we can get an effective Hamiltonian for the cascaded setup which can be directly used to solve the dynamics of such systems [156]. Thus, our aim is to find the unitary propagator $U(t)$ that directly generates the evolution of any general operator $\hat{A}$ of the cascaded system and bath in the Heisenberg picture, i.e., $\hat{A}(t) = U^\dagger(t)\hat{A}U(t)$. This unitary operator gives us the required Hamiltonian for an effective single quantum system.

However, before finding the unitary operator for the cascaded setup, we first discuss the form of the unitary propagator for a single quantum system in the next section. We then proceed to find the unitary operator for the cascaded setup in Sec. 7.2.2.

7.2.1 Unitary propagator for a single quantum system

We consider an arbitrary system operator $\hat{a}$. The Langevin equation for such system is given by Eq. (3.30)

$$\dot{\hat{a}} = -\mathrm{i}[a, H_S] - \left[\hat{a}, \hat{c}^\dagger\right]\left(\frac{\gamma}{2}\hat{c} + \sqrt{\gamma}\hat{b}_{\mathrm{in}}(t)\right) + \left(\frac{\gamma}{2}\hat{c}^\dagger + \sqrt{\gamma}\hat{b}^\dagger_{\mathrm{in}}(t)\right)[\hat{a}, \hat{c}]. \tag{7.9}$$

The corresponding unitary propagator for the Eq. (7.9) which governs the evolution of the system and bath can be obtained as [156] [2]

$$U(t) = \mathcal{T}exp\left\{\int_{t_0}^{t}\left[-\mathrm{i}H_S + (\sqrt{\gamma}\hat{c}\hat{b}^\dagger_{\mathrm{in}}(t') - \sqrt{\gamma}\hat{c}^\dagger\hat{b}_{\mathrm{in}}(t'))\right]dt'\right\}, \tag{7.10}$$

[2]Note that $\hat{a} \equiv \hat{a}_s \otimes I_b$ since we have not traced out the bath degree of freedom. Thus, the evolution of system plus bath can be expressed in terms of unitary propagator $U(t)$ and gives the corresponding dynamical equation gievn by Eq. (7.9).

with $U(t_0) = I_s \otimes I_b$ and the subscripts s and b correspond to the system and bath degrees of freedom, respectively.

To understand why $U(t)$ is the unitary propagator for a single quantum system, we consider the corresponding dynamical equation of the operator $\hat{a}$ which can be written as

$$\dot{a} = \dot{U}(t)^\dagger \hat{a} U(t) + U^\dagger(t)\hat{a}\dot{U}(t), \tag{7.11}$$

Further, $\dot{U}(t)$ can be written using Eq. (7.10) which reads

$$\begin{aligned}\dot{U} =& \Big[-\mathrm{i}H_S + \Big(\sqrt{\gamma}\hat{c}\hat{b}^\dagger_{\mathrm{in}}(t) - \sqrt{\gamma}\hat{c}^\dagger\hat{b}_{\mathrm{in}}(t)\Big)\Big]U(t)\\ =& \Big[-\mathrm{i}H_S + \Big(\hat{L}\hat{b}^\dagger_{\mathrm{in}}(t) - \hat{L}^\dagger\hat{b}_{\mathrm{in}}(t)\Big)\Big]U(t)\\ =& M(t)U(t),\end{aligned} \tag{7.12}$$

where $\hat{L} = \sqrt{\gamma}\hat{c}$ is defined as the coupling operator [156]. Eq. (7.12) gives the generator $M(t)$ of the unitary operator given by [156]

$$M(t) = \Big[-\mathrm{i}H_s + \Big(\hat{L}\hat{b}^\dagger_{\mathrm{in}}(t) - \hat{L}^\dagger\hat{b}_{\mathrm{in}}(t)\Big)\Big]. \tag{7.13}$$

Using Eq. (7.12), we can write Eq. (7.11) as

$$\begin{aligned}\dot{\hat{a}} &= \dot{U}(t)^\dagger\hat{a}U(t) + U^\dagger(t)\hat{a}\dot{U}(t)\\ &= U^\dagger(t)M^\dagger(t)\hat{a}U(t) + U^\dagger(t)\hat{a}M(t)U(t)\\ &= U^\dagger(t)\Big[\mathrm{i}H_s + \Big(\hat{b}^\dagger_{\mathrm{in}}(t)\hat{L}^\dagger - \hat{b}_{\mathrm{in}}(t)\hat{L}\Big)\Big]\hat{a}U(t)\\ &+ U^\dagger(t)\hat{a}\Big[-\mathrm{i}H_s + \Big(\hat{L}\hat{b}^\dagger_{\mathrm{in}}(t) - \hat{L}^\dagger\hat{b}_{\mathrm{in}}(t)\Big)\Big]U(t)\\ &= -\mathrm{i}U^\dagger[\hat{a}, H_s]U(t) - U^\dagger\Big[\hat{a}, \hat{L}^\dagger\Big]\hat{b}_{\mathrm{in}}(t)U(t) + U^\dagger(t)\hat{b}^\dagger_{\mathrm{in}}(t)\Big[\hat{a}, \hat{L}\Big]U(t).\end{aligned} \tag{7.14}$$

Further, using the following identity (see Refs. [156] and [157] for more details)

$$\Big[\hat{b}_{\mathrm{in}}(t), U(t)\Big] = \frac{\sqrt{\gamma}}{2}\hat{c}U(t) = \frac{LU(t)}{2}, \tag{7.15}$$

Eq. (7.14) becomes

$$\begin{aligned}\dot{\hat{a}} = -\mathrm{i}U^\dagger[\hat{a}, H_s]U(t) - U^\dagger\big[\hat{a}, L^\dagger\big]U(t)\hat{b}_{\mathrm{in}}(t) - \frac{1}{2}U^\dagger\big[\hat{a}, L^\dagger\big]LU(t)\\ + \hat{b}^\dagger_{\mathrm{in}}(t)U^\dagger(t)\Big[\hat{a}, \hat{L}\Big]U(t) + \frac{1}{2}U^\dagger(t)\hat{L}^\dagger\Big[\hat{a}, \hat{L}\Big]U(t).\end{aligned} \tag{7.16}$$

Substituting $\hat{L} = \sqrt{\gamma}\hat{c}$ in the above equation yields the required Langevin equation [Eq. (7.9)].

Thus, the generator $M(t)$ yields the same Langevin equation as given in Eq. (7.9). In the next section, we obtain the unitary propagator for two quantum systems coupled in a cascaded manner.

7.2.2 Unitary propagator for cascaded system

Here, we consider the system with two cascaded components for which the evolution of any operator $\hat{A}$ corresponding to this cascaded setup is given by Eq. (7.7). One can find the corresponding unitary propagator for this case also, which is given by $U(t) = \mathcal{T}exp\Big\{\int_{t_0}^{t} M_{\text{cas}}(t')dt'\Big\}$. The generator $M_{\text{cas}}(t)$ for the cascaded system is now given by [156]

$$\begin{aligned} M_{\text{cas}}(t) &= -\text{i}\Big(H_{S_1} + H_{S_2}\Big) - \frac{\sqrt{\gamma_1\gamma_2}}{2}\Big(\hat{c}_2^\dagger\hat{c}_1 - \hat{c}_1^\dagger\hat{c}_2\Big) + \Big(\sqrt{\gamma_1}\hat{c}_1 + \sqrt{\gamma_2}\hat{c}_2\Big)\hat{b}_{\text{in}}^\dagger(t) \\ &\qquad - \Big(\sqrt{\gamma_1}c_1^\dagger + \sqrt{\gamma_2}c_2^\dagger\Big)\hat{b}_{\text{in}}(t), \\ &= -\text{i}\Big[H_{S_1} + H_{S_2} - \frac{\text{i}}{2}\sqrt{\gamma_1\gamma_2}\Big(\hat{c}_2^\dagger\hat{c}_1 - \hat{c}_1^\dagger\hat{c}_2\Big)\Big] + \Big[\Big(\hat{L}_1 + \hat{L}_2\Big)\hat{b}_{\text{in}}^\dagger(t) - \Big(\hat{L}_1^\dagger + \hat{L}_2^\dagger\Big)\hat{b}_{\text{in}}(t)\Big], \end{aligned} \tag{7.17}$$

where $\hat{L}_1 = \sqrt{\gamma_1}\hat{c}_1$ and $\hat{L}_2 = \sqrt{\gamma_2}\hat{c}_2$ represent the coupling operator or the Lindblad operator for the two subsystems.

Similar to the case for a single quantum system, this unitary propagator generates the equation of motion for an operator A of the cascaded system given by $\dot{\hat{A}} = \dot{U}^\dagger\hat{A}U + U^\dagger\hat{A}\dot{U}$ which exactly matches Eq. (7.7).

Comparing the generator $M_{\text{cas}}(t)$ to the generator for a single quantum system given by Eq. (7.13), we note that this cascaded system with two components can be modeled as an effective single quantum system described by an effective Hamiltonian and the corresponding effective coupling operator given by [156]

$$H_{\text{eff}} = H_{S_1} + H_{S_2} - \frac{\text{i}}{2}\sqrt{\gamma_1\gamma_2}\Big(\hat{c}_2^\dagger\hat{c}_1 - \hat{c}_1^\dagger\hat{c}_2\Big), \tag{7.18}$$

$$\hat{L}_{\text{eff}} = \sqrt{\gamma_1}\hat{c}_1 + \sqrt{\gamma_2}\hat{c}_2. \tag{7.19}$$

Thus, we can model the composite system consisting of two cascaded subsystems as a single system with an effective Hamiltonian H_{eff} and the corresponding coupling operator $\hat{L}_{\text{eff}}$. This Hamiltonian can be used to obtain the equation of motion for an operator $\hat{A}$ of the cascaded system given by Eq. (7.7).

As an example, we consider a cascaded system consisting of two empty cavities with cavity field operators $\hat{a}_1$ and $\hat{a}_2$ with the corresponding decay rates κ_1 and κ_2. We can directly write the Heisenberg-Langevin equations for the two cavities using Eqs. (7.18) and (7.19).

$$\dot{\hat{a}}_1(t) = -\mathrm{i}\Big(\Delta_{c1} + \frac{\kappa_1}{2}\Big)\hat{a}_1(t) - \sqrt{\kappa_1}\hat{b}_{\text{in}}(t), \tag{7.20}$$

$$\dot{\hat{a}}_2(t) = -\mathrm{i}\Big(\Delta_{c2} + \frac{\kappa_2}{2}\Big)\hat{a}_2(t) - \sqrt{\kappa_1\kappa_2}\hat{a}_1(t) - \sqrt{\kappa_2}\hat{b}_{\text{in}}(t), \tag{7.21}$$

where Δ_{c1} and Δ_{c2} are the cavity detunings for the two cavities. Eq. (7.21) shows the effect of cavity 1 on the dynamics of cavity 2, which is due to the driving of cavity 2 by the output from cavity 1. At the same time, the dynamics of cavity 1 is not affected by cavity 2, as seen from Eq. (7.20). The corresponding input-output relation for this effective system becomes [156, 158]

$$\hat{b}_{\text{out}} = \hat{b}_{\text{in}} + \hat{L}_{\text{eff}} = \hat{b}_{\text{in}} + \sqrt{\kappa_1}\hat{a}_1(t) + \sqrt{\kappa_2}\hat{a}_2(t). \tag{7.22}$$

which shows that the output field consists of the contribution from the input field and the two cavities.

This description of the cascaded setup using an effective Hamiltonian becomes useful in describing the interaction of a quantum system with pulses of radiation. The interaction of a quantum system with an input pulse is modeled in terms of a virtual cavity that drives the quantum system of interest in a cascaded manner [79, 80].

7.3 Kiilerich-Mølmer input-output theory

In this section, we introduce the complete input-output theory that describes the interaction of a local quantum system with incident pulses of radiation [79, 80]. It is based on master equation formalism and serves as an efficient tool to study the

dynamics of interaction of an input light pulse prepared in an arbitrary quantum state interacting with a local quantum system which may scatter into an output field with a single mode or multiple modes with different pulse shapes. In general, the local quantum system here can be atom, cavity, or atom-cavity systems.

The fundamental idea behind this formalism is to model the input pulse of the quantum field interacing with the quantum system of interest as an output field released from a virtual input cavity that gets coupled to the quantum system with a complex time-dependent coupling. This virtual cavity simply emits the required pulse shape of the input field and is coupled to the quantum system of interest in a cascaded manner which drives the quantum system of interest. Similarly, this treatment is extended to model the scattered output field pulse as a virtual output cavity that captures the scattered output mode shape. This modeling enables us to solve the master equation of the full system, which gives the entire dynamics of the system along with the input and output field modes. We start by discussing the dynamics of the modeling of the input pulse as a virtual cavity which gets coupled to the quantum system of interest in a cascaded manner.

7.3.1 Modeling of an input field pulse by virtual cavity

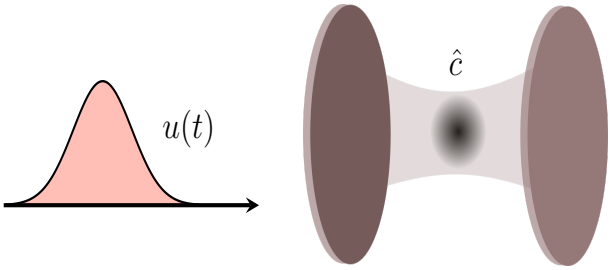

Figure 7.2: An atom-cavity system driven by an input field with pulse shape $u(t)$. $\hat{c}$ is the cavity operator.

We consider an atom-cavity system with Hamiltonian $\hat{H}_s$, which is driven by an input field with temporal pulse shape $u(t)$ through one of the mirrors as shown in Fig. 7.2. This can be modeled by an effective cascaded quantum system consisting of a virtual input cavity and the quantum system of interest. The input pulse is now replaced by a virtual cavity with a complex time-dependent coupling $g_u(t)$ [79, 80].

This complex time-dependent coupling ensures that the virtual cavity releases an output field with the required pulse shape $u(t)$ that drives the quantum system of interest, as shown in Fig. 7.3.

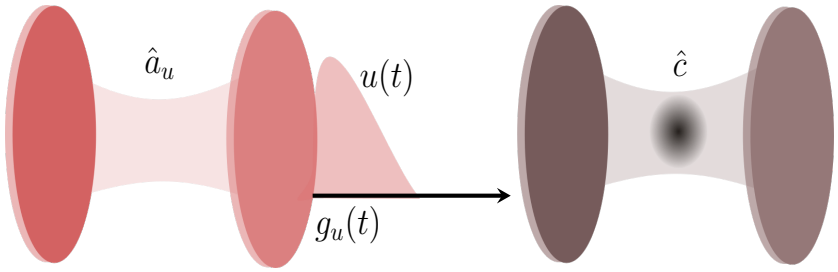

Figure 7.3: The input pulse is modeled as an output from a virtual cavity with cavity mode $\hat{a}_u$ with complex time-dependent coupling $g_u(t)$ which releases the required pulse shape $u(t)$.

The dynamics of this cascaded system can now be obtained using the master equation approach. For this, we can use the effective Hamiltonian approach as discussed in Sec. 7.2 to describe the coupling between the virtual input cavity and the quantum system. Following Eq. (7.18), this entire setup, as shown in Fig. 7.3 can be described by an effective Hamiltonian given by [79, 80]

$$H = H_s + \frac{\mathrm{i}}{2}\big(\sqrt{\kappa} g_u(t) \hat{a}_u^\dagger \hat{c} - H.c.\big), \tag{7.23}$$

where $\hat{c}$ and $\hat{a}_u$ are the operators for the system cavity and the virtual cavity field mode, respectively. κ is the decay rate of the system cavity. The Lindblad dissipator $\mathcal{D}[\hat{L}_0]$ for this effective system is described by the following operator [see Eq. (7.19)]

$$\hat{L}_0(t) = \sqrt{\kappa}\hat{c} + g_u^*(t)\hat{a}_u, \tag{7.24}$$

where the complex time-dependent coupling strength $g_u(t)$ is given in terms of the pulse shape $u(t)$ as [79, 80]

$$g_u(t) = \frac{u^*(t)}{\sqrt{1 - \int_0^t |u(t')|^2 dt'}}. \tag{7.25}$$

This time-dependent coupling results in the emission from the virtual cavity into a wavepacket of the required shape $u(t)$, which drives the quantum system.

The master equation for the effective system described by the combined state,

ρ_{us} of the virtual input cavity and the quantum system is given by [80]

$$\frac{\mathrm{d}\rho_{us}}{\mathrm{d}t} = -\mathrm{i}[H, \rho_{us}] + \mathcal{D}[\hat{L}_0]\rho_{us} + \sum_i \mathcal{D}[\hat{L}_i]\rho_{us}, \tag{7.26}$$

where $\hat{L}_i$ represents the additional Lindblad operators for the given quantum system. Eq. (7.26) can be further simplified by substituting $\hat{H}$ which gives

$$\begin{aligned}\frac{\mathrm{d}\rho_{us}}{\mathrm{d}t} = &-\mathrm{i}[H_s, \rho_{us}] + \sqrt{\kappa}g_u(t)\big(\hat{c}\rho_{us}\hat{a}_u^\dagger - \rho_{us}\hat{a}_u^\dagger\hat{c}\big) + \sqrt{\kappa}g_u^*(t)\big(\hat{a}_u\rho_{us}\hat{c}^\dagger - \hat{a}_u\hat{c}^\dagger\rho_{us}\big) \\ &+\mathcal{D}[\sqrt{\kappa}\hat{c}]\rho_{us} + \mathcal{D}[g_u^*(t)\hat{a}_u]\rho_{us} + \sum_i \mathcal{D}[\hat{L}_i]\rho_{us},\end{aligned} \tag{7.27}$$

The commutator of ρ_{us} with the interaction term in the Hamiltonian in Eq. (7.23) along with the term $\mathcal{D}[\hat{L}_0]\rho_{us}$ in Eq. (7.27) contribute together for the unidirectional flow of the input field. This can be seen from Eq. (7.27), where the density matrix ρ_{us} is only acted by the annihilation operator $\hat{a}_u$ from the left and the creation operator $\hat{a}_u^\dagger$ from the right. Thus, the input field is always annihilated from the virtual input cavity, which is the key requirement for the cascaded coupling of the virtual cavity to the system.

7.3.2 Obtaining the intensity and mode shape of the output field

The time-dependent Lindblad operator, $\hat{L}_0(t)$ described in Eq. (7.24) resembles the standard input-output relation $\hat{a}_{\mathrm{out}}(t) = \sqrt{\kappa}\hat{c} + \hat{a}_{\mathrm{in}}(t)$, for a cavity field mode $\hat{c}$ interacting with an input field $\hat{a}_{\mathrm{in}}$. This shows that the output field includes the contribution from the emission by the quantum system and the input field. Further, this also hints towards a direct correspondence between the Lindblad operator $\hat{L}_0(t)$ and the output field from the cavity. Hence, the intensity of the output field in this theory is simply given by $I_{\mathrm{out}}(t) = \Big\langle [\hat{L}_0(t)]^\dagger \hat{L}_0(t) \Big\rangle$.

Another important quantity of interest is the two-time autocorrelation function of the output field which is defined as [80] (see Appendix B.1)

$$g^{(1)}(t, t') = \Big\langle [\hat{L}_0(t)]^\dagger \hat{L}_0(t') \Big\rangle = Tr\Big\{\hat{L}_0^\dagger(t) V(t, t')\Big\{\hat{L}_0(t')\rho_{us}(t')\Big\}\Big\}, \tag{7.28}$$

where $V(t,t')$ represents the time evolution operator for the density matrix ρ_{us}. The usefulness of this two-time correlation function comes from its eigenmode decomposition [80]

$$g^{(1)}(t,t') = \left\langle [\hat{L}_0(t)]^\dagger \hat{L}_0(t') \right\rangle = \sum_i n_i v_i^*(t) v_i(t'), \tag{7.29}$$

which directly gives the set of most prominent orthogonal output modes in the output field given by $v_i(t)$ along with the corresponding number of excitations n_i associated with each mode.

Since $\hat{L}_0(t)$ represents the output field from the cavity, $g^{(1)}(t,t')$ in Eq. (7.29) denotes the correlation between the output electric field at different times. It is well known that the Fourier transform of the standard two-time correlation function of the electric field is used to obtain the spectrum of the field in the frequency domain [159]. In the present case, this autocorrelation function is used to obtain the shape of the orthogonal temporal field modes and the degree of excitation, which is obtained using the diagonalization of the autocorrelation function over a finite time grid, also known as the Mercer's expansion [131, 160]. Experimentally, obtaining the temporal modes through this method has been achieved using homodyne detection setup [161].

7.3.3 Dynamics of full cascaded system and quantum state of the output field

Here we discuss how one can completely determine the exact quantum state of a given output mode with shape $v(t)$. To gain complete knowledge about the state of an output field mode of shape $v(t)$, a virtual output cavity is now attached to the quantum system of interest. It is coupled to the quantum system with the corresponding time-dependent input coupling $g_v(t)$ in a cascaded manner such that the virtual output cavity completely captures the required output mode $v(t)$. The corresponding complex time-dependent coupling $g_v(t)$ in order to acquire the required output mode $v(t)$ is given by [79, 80]

$$g_v(t) = -\frac{v^*(t)}{\sqrt{\int_0^t |v(t')|^2 dt'}}. \tag{7.30}$$

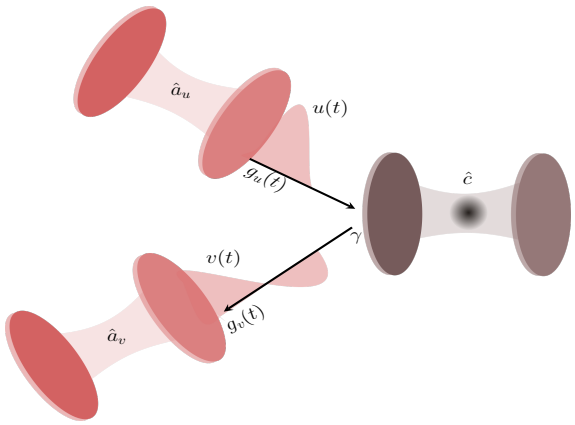

Figure 7.4: Full cascaded system with virtual input cavity (with cavity mode $\hat{a}_u$) relasing the required input mode with pulse shape $u(t)$, and a virtual output cavity (with cavity mode $\hat{a}_v$) which captures the output mode with mode shape $v(t)$. $g_u(t)$, and $g_v(t)$ are the corresponding complex time-dependent coupling strengths of the the virtual input and output cavity, respectively.

The state of the entire system can now be described by an effective cascaded quantum system consisting of the three components, which include: (a) The virtual input cavity with cavity mode $\hat{a}_u$ that releases the input pulse. (b) The quantum system, which interacts with the input field and (c) the virtual output cavity with cavity mode $\hat{a}_v$, which gradually acquires the output field mode. This is described in Fig. 7.4.

The Hamiltonian of the entire cascaded system with the system operator $\hat{c}$ and the input and output virtual cavity field operators given by $\hat{a}_u$ and $\hat{a}_v$, respectively, reads [79, 80]

$$H = H_s + \frac{\mathrm{i}}{2}\big(\sqrt{\kappa} g_u(t)\hat{a}_u^\dagger \hat{c} + \sqrt{\kappa} g_v^*(t)\hat{c}^\dagger \hat{a}_v + g_u(t)g_v^*(t)\hat{a}_u^\dagger \hat{a}_v - H.c.\big). \tag{7.31}$$

The damping term is now described by the Lindblad dissipator $\mathcal{D}[\hat{L}_0'(t)]$ with

$$\hat{L}_0'(t) = \sqrt{\kappa}\hat{c} + g_u^*(t)\hat{a}_u + g_v^*(t)\hat{a}_v, \tag{7.32}$$

which shows the contributions from the system and the two virtual cavities.

Solving the master equation for this complete cascaded system (represented by state ρ_{usv} in the Hilbert space of the virtual input cavity, the system and the virtual output cavity) gives complete information about the quantum state of the outgoing field mode. One can use this effective Hamiltonian to know the exact state of any

desired output field mode. In other words, the virtual output cavity with the the input coupling $g_v(t)$ simply acts as a filter to capture the required ouptut mode with pulse shape $v(t)$, while the other output modes are described as loss and get reflected off from the virtual output cavity.

Moreover, if the output field consists of multiple modes denoted by $v_i(t)$, we can also accommodate them using this theory. This is done by considering a sequence of cascaded virtual output cavities with the corresponding coupling strengths $g_{vi}(t)$ placed one after the other. In this approach, each virtual cavity with cavity mode $\hat{a}_{vi}$ acts as a filter for the corresponding output mode $v_i(t)$. (See the Appendix of [80] for more details). In the next section, we discuss an example applying this theory [79, 80].

7.3.4 Multiple output modes from an empty cavity with phase noise

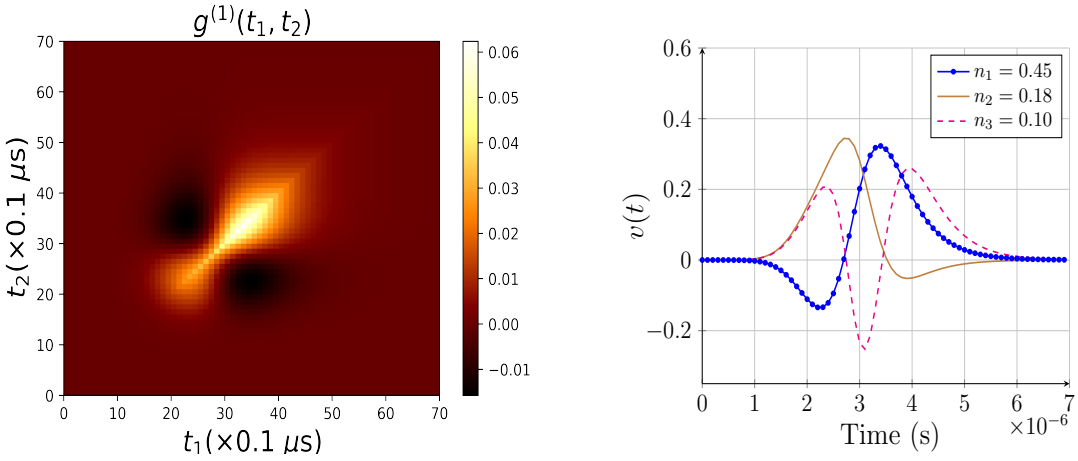

(a) (b)

Figure 7.5: Input fock state $|1\rangle$ to an empty cavity with phase noise. (a) Two time correlation function, $g^{(1)}(t_1, t_2)$ obtained numericallly using Eq. (7.28). (b) Shape of the first three prominent output modes along with the mean excitation carried by each mode. The cavity parameters considered are $(\kappa, \kappa_p) = (2, 2)$ MHz.

Here, we consider a simple example of an empty cavity as a quantum system of

interest that carries a phase noise corresponding to an additional Lindblad operator $\hat{L}_1 = \sqrt{\kappa_p}\hat{c}^\dagger\hat{c}$ in Eq. (7.26) as discussed in [80]. We consider the input field as fock state $|1\rangle$ with a Gaussian pulse shape given by

$$u(t) = \frac{1}{\sqrt{\tau}\pi^{1/4}} \exp\left\{-\frac{(t-t_0)^2}{2\tau^2}\right\}, \tag{7.33}$$

with temporal width τ centered at t_0.

The output field can be obtained using the two-time correlation function, which reveals that the output field consists of multiple orthogonal output modes. Fig. 7.5(a) shows the plot for the two-time correlation function $g^{(1)}(t_1, t_2)$ obtained numericallly using Eq. (7.28). Fig. 7.5(b) shows the first three prominent orthogonal modes of the output field along with the quanta of excitation carried by each mode. This shows that the maximum population carried by the most dominant mode is 0.45. Further, as expected, the excitations carried by all the modes sum up to 1, i.e., $\sum_i n_i = 1$. The numerical calculations are done using the QuTiP toolbox [102, 162]. The cavity parameters taken for the above calculations are $(\kappa, \kappa_p) = (2, 2)$ MHz.

Thus, using this theory, we can solve the dynamics of arbitrary atom-cavity systems interacting with quantum pulses of radiation and obtain the exact state of the single or multiple field output modes. However, one should note that this is based on solving the master equation of the full cascaded system. This can pose difficulty if the Hilbert space dimension of the full system, N, becomes very large as this amounts to the evolution of the density matrix of order N^2. However, an alternate approach to overcome this computational complexity is to use the Monte Carlo wave function method (MCWF) [163], which is based on unraveling the master equation into a set of quantum trajectories. This method uses the evolution of wave function, which is a N dimensional state vector using an effective non-Hermitian Hamiltonian (see Appendix B.2 for details).

In the next chapter, we use the this complete input-output theory to investigate the photon-subtraction process using an atom-cavity system.

Chapter 8

Photon subtraction using atom-cavity interactions

The photon subtraction process removes a single photon from a given incident field with state $|n\rangle$ and converts it to state $|n-1\rangle$. It is an important tool in quantum information and long-range quantum communication and is useful in generating non-classical states of light [81, 82, 83, 84, 85, 86], verifying the fundamental nature of quantum mechanics [87, 88], and increasing the entanglement between the Gaussian states [164, 165].

The most common scheme to subtract a single photon from the input field has been implemented using a beam splitter with very high transmissivity, with one detector placed in one of the output modes. However, it is a probabilistic process relying on the heralded detection of a single photon, which indicates that a single photon has been subtracted from the input light field and accompanies the disadvantage of having low success rates [87]. Moreover, in this scheme, the subtracted single photon is detected and lost, and only the photon subtracted state is available and used to implement quantum information processing tasks.

Another method for single photon subtraction uses atom-cavity interactions, which can subtract a single photon with very high efficiencies. Moreover, the subtracted single photon is spatially separated and can be used to implement further

quantum information processing tasks. The only limiting factor in the photon subtraction process using the atom-cavity system is the decay rate of the excited state of the atom. The photon-subtraction scheme using atom-cavity interactions includes a three-level atom coupled to an optical cavity [14]. The two transitions of the atom are coupled to the two orthogonal polarization through different cavity modes. An input pulse with state $|n\rangle$ and carrying a particular polarization corresponding to one of the transitions is transformed to the state $|n-1\rangle$ along with the emission of a single photon state $|1\rangle$ in the orthogonal polarization mode.

In this chapter, we investigate the photon subtraction process using complete input-output theory as discussed in the previous chapter. This reveals the scattering of the output field into multiple modes upon the photon subtraction process and provides a clear picture of the photon-subtraction process. We first describe the photon-subtraction scheme using atom-cavity interactions in Sec. 8.1. Subsequently, in Sec. 8.2, we discuss the dynamics for the photon-subtraction process applying the complete input-output theory [79]. We verify the photon subtraction for the input field as the fock state $|1\rangle$, which matches with the usual description of the photon subtraction process [14] in Sec 8.2.1. In the subsequent sections, we discuss the photon subtraction for the input field containing more than one photon, which does not fit into the standard single mode description of the photon subtracted field. In each case, we also find out the state of the prominent output modes in the output field.

8.1 Photon subtraction scheme using atom cavity system

The photon-subtraction process using an atom-cavity system consists of a Λ-type three-level atom with two degenerate ground states ($|g\rangle$, $|s\rangle$) and one excited state ($|e\rangle$). The two atomic transitions $|g\rangle \leftrightarrow |e\rangle$ and $|e\rangle \leftrightarrow |s\rangle$ are coupled to the two orthogonal cavity modes $\hat{a}$ and $\hat{b}$ respectively, corresponding to the two orthogonal polarization components of light. The system is shown in Fig. 8.1. Here, κ is the decay rate of the cavity field modes, which is considered to be the same for both

cavities.

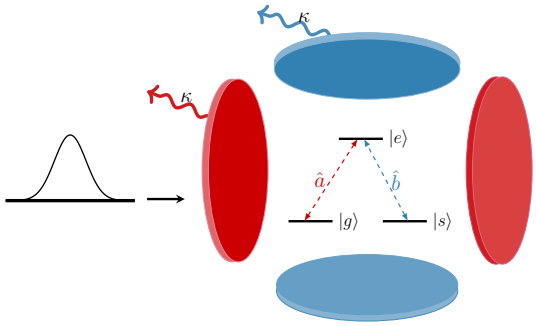

Figure 8.1: Atom-cavity system used as a photon subtractor. A lambda-type three-level atom with two ground states $|g\rangle$, $|s\rangle$ and one excited state $|e\rangle$ is considered. Here, the transition $|g\rangle \leftrightarrow |e\rangle$ is coupled to the horizontal cavity mode $\hat{a}$ (shown in red), while the transition $|e\rangle \leftrightarrow |s\rangle$ is coupled to an identical vertical cavity mode $|b\rangle$ (shown in blue). κ is the decay rate of the two cavities.

If the initial state of the atom is $|g\rangle$, and an input light pulse with temporal width τ is sent as an input to drive the horizontal cavity mode $\hat{a}$ (shown in red), it gets coupled to the atomic transition $|g\rangle \rightarrow |e\rangle$. For the case when the input pulse with sufficient temporal pulse width, i.e., $\tau \gg \kappa^{-1}$ (also known as the adiabatic limit), the adiabatic following takes place which results in the transfer of the atomic state from $|g\rangle$ to $|s\rangle$. This leads to the emission of a single photon into the vertical cavity mode (shown in blue) [14] which eventually leaks out of the cavity mode $\hat{b}$ with a decay rate of κ. This complete transfer of the atomic state from $|g\rangle$ to $|s\rangle$ resulting in the single photon emission into the vertical cavity mode has been shown in [14] using the space-time description model.

The entire process results in the single photon subtraction from the input pulse containing n photons giving $(n-1)$ photons in the output from the horizontal cavity and a single photon in the output from the vertical cavity mode. Since the atomic state is transferred from $|g\rangle$ to $|s\rangle$ in this process, the atom-cavity system becomes transparent to further photons in the input field, and there is no further subtraction of the photons from the input field.

The extraction of a single photon from the input field has been experimentally verified for a weak classical input pulse following a similar protocol based on a three-level atom in which the two transitions of the atom are coupled to the different

directions of a single mode wave-guide [166]. Here, the subtracted single photon gets deterministically reflected, while the rest of the photons get transmitted.

Unlike other protocols, in the photon subtraction scheme based on a single three-level atom, not more than a single photon can be subtracted since after the transition of the atom from one ground state to another, the system becomes transparent to the further photons in the input pulse.

The photon-subtraction using the atom-cavity system seems promising for use in the quantum information protocols. However, one needs to be careful, as we will see that removing a single photon from the input state does not guarantee that the input state $|n\rangle$ will transform to $|n-1\rangle$. We also need to know how a given input state gets modified after the removal of the single photon. In this work, we show that although there is always a single photon that is being removed from the input field, the state after the photon subtraction gets scattered over multiple orthogonal temporal modes. This may affect the quantum information processes and protocols that depend on the photon subtraction.

In the upcoming section, we show that for an input field pulse consisting of more than one photon, the usual description of the photon-subtraction process in terms of a single mode output field as proposed in [14] does not apply. The output field from the cavity modes in such cases is scattered over multiple orthogonal temporal modes, with each mode carrying a different amount of excitation and having a different quantum state. We will also discuss the example of photon subtraction by considering different kind of states in the input field such as fock state $|n\rangle$ $(n = 1, 2, 3)$, superposition state $(|1\rangle + |2\rangle)/\sqrt{(2)}$ and a weak coherent state $|\alpha = 1\rangle$.

8.2 Obtaining the dynamics of photon-subtraction using complete input-output theory

We consider the atom-cavity system used as a photon subtractor as described in Fig. 8.1. The Hamiltonian in the interaction picture for this system is given by

$$H_s = \hbar g(|e\rangle\langle g|\,\hat{a} + |e\rangle\langle s|\,\hat{b} + H.c). \tag{8.1}$$

Here, it is assumed that both the transitions are in resonance with the cavity mode frequency. As discussed in Sec. 8.1, if the initial state of the atom is $|g\rangle$, and the cavity mode $\hat{a}$ is driven by the input quantum pulse, the atomic state transfers from $|g\rangle$ to $|s\rangle$ resulting in a single photon into the vertical cavity mode $\hat{b}$.

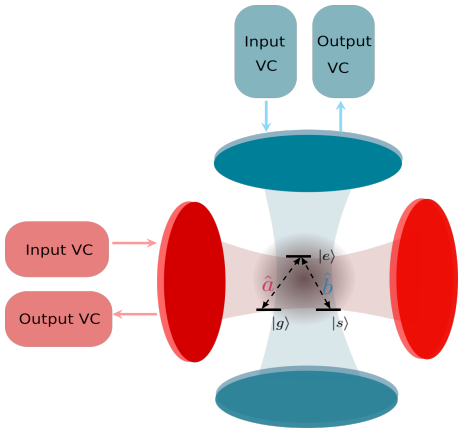

Figure 8.2: Virtual input and output cavities attached to both cavity modes to obtain the state of the output field mode.

In order to gain complete information about the output field from the two cavity modes as shown in Fig. 8.1, we apply the KMIO formalism as discussed in Sec. 7.3. To proceed, we simply consider the atom-cavity system in Fig. 8.1, and attach the virtual input and output cavities with complex time-dependent couplings to each cavity mode. The effective system after attaching the cascaded virtual cavities is shown in Fig. 8.2.

Following the approach as discussed in Sec. 7.3 and using Eq. (7.31), the Hamiltonian for the complete system consisting of two sets of virtual cavities attached to the quantum system as shown in Fig. 8.1 can be written as [79, 80]

$$
\begin{aligned}
H_f &= H_s + H_{c_a} + H_{c_b}, \\
&= H_s + \frac{\mathrm{i}}{2}\Big(\sqrt{\kappa} g_{ua}(t)\hat{a}_u^\dagger \hat{a} + \sqrt{\kappa} g_{va}^*(t)\hat{a}^\dagger \hat{a}_v + g_{ua}(t) g_{va}^*(t)\hat{a}_u^\dagger \hat{a}_v - H.c\Big) + \\
&\quad \frac{\mathrm{i}}{2}\Big(\sqrt{\kappa} g_{ub}(t)\hat{b}_u^\dagger \hat{b} + \sqrt{\kappa} g_{vb}^*(t)\hat{b}^\dagger \hat{b}_v + g_{ub}(t) g_{vb}^*(t)\hat{b}_u^\dagger \hat{b}_v - H.c\Big).
\end{aligned} \tag{8.2}
$$

Here, H_s is the system Hamiltonian given by Eq. (8.1). H_{c_a} and H_{c_b} denote the Hamiltonians corresponding to the cascaded interactions of the virtual input and output cavities with the cavity modes $\hat{a}$ and $\hat{b}$ respectively. $\hat{a}_u(\hat{b}_u)$ denote the cavity field mode operators for the virtual input cavity attached to the horizontal (vertical) cavity mode $\hat{a}$ $(\hat{b})$. Similarly, $\hat{a}_v$ $(\hat{b}_v)$ represents the cavity mode operator for the virtual output cavity coupled to the cavity mode $\hat{a}$ $(\hat{b})$ as shown in Fig. 8.2.

The corresponding Lindblad operators associated with the two decay channels corresponding to the two cavity modes $\hat{a}$ and $\hat{b}$ respectively in accordance with Eq. (7.32) are [80]

$$
\hat{L}_a(t) = \sqrt{\kappa}\hat{a} + g_{ua}^*(t)\hat{a}_u + g_{va}^*(t)\hat{a}_v, \tag{8.3}
$$

$$
\hat{L}_b(t) = \sqrt{\kappa}\hat{b} + g_{ub}^*(t)\hat{b}_u + g_{vb}^*(t)\hat{b}_v, \tag{8.4}
$$

with the corresponding coupling strengths of these virtual input and output cavities given by

$$
g_{ua}(t) = \frac{u_a^*(t)}{\sqrt{1 - \int_0^t |u_a(t')|^2 dt'}},\ g_{ub}(t) = \frac{u_b^*(t)}{\sqrt{1 - \int_0^t |u_b(t')|^2 dt'}}, \tag{8.5}
$$

$$
g_{va}(t) = -\frac{v_a^*(t)}{\sqrt{\int_0^t |v_a(t')|^2 dt'}},\ g_{vb}(t) = -\frac{v_b^*(t)}{\sqrt{\int_0^t |v_b(t')|^2 dt'}}, \tag{8.6}
$$

where $u_a(t)$ and $v_a(t)$ are the mode shpaes corresponding to the input, and the output field modes of the cavity $\hat{a}$, respectively. Similarly, $u_b(t)$ and $v_b(t)$ correspond to the mode shapes of the input, and the output field of the cavity mode $\hat{b}$, respectively.

Solving the master equation for the complete system using this Hamiltonian and the corresponding Lindblad dissipator $\mathcal{D}[\hat{L}_a(t)]$ and $\mathcal{D}[\hat{L}_b(t)]$ gives us the required quantum state of the outgoing field mode after the photon subtraction process. To solve the master equation for the full system, we require the information about the mode shapes $v_a(t)$ and $v_b(t)$ corresponding to the output field modes $\hat{a}_v$ and $\hat{b}_v$ respectively.

The most prominent output modes can be calculated using the the two-time auto-correlation function following the approach discussed in Sec. 7.3.2. For this, we consider the atom-cavity system being attached to the virtual input cavities only. Following Eq. (7.23), the Hamiltonian for such a system can be written as

$$H = H_s + \frac{\mathrm{i}}{2}\left[\sqrt{\kappa} g_{ua}(t)\hat{a}_u^\dagger \hat{a} - \sqrt{\kappa} g_{ua}^*(t)\hat{a}_u \hat{a}^\dagger\right] + \frac{\mathrm{i}}{2}\left[\sqrt{\kappa} g_{ub}(t)\hat{b}_u^\dagger \hat{b} - \sqrt{\kappa} g_{ub}^*(t)\hat{b}_u \hat{b}^\dagger\right], \tag{8.7}$$

The Lindblad operators for the two decay channels corresponding to the two cavity modes $\hat{a}$ and $\hat{b}$ will simply become (from Eq. 7.24)

$$\hat{L}_a^0(t) = \sqrt{\kappa}\hat{a} + g_{ua}^*(t)\hat{a}_u, \tag{8.8}$$

$$\hat{L}_b^0(t) = \sqrt{\kappa}\hat{b} + g_{ub}^*(t)\hat{b}_u. \tag{8.9}$$

Solving the master equation for this system with the Hamiltonian in Eq. (8.7) along with the Lindblad operators in Eqs. (8.8) and (8.9) gives the required output correlation functions corresponding to the two decay channels as

$$g_a^{(1)}(t,t') = \left\langle \hat{L}_a^{0\dagger}(t)\hat{L}_a^0(t)\right\rangle \text{ and } g_b^{(1)}(t,t') = \left\langle \hat{L}_b^{0\dagger}(t)\hat{L}_b^0(t)\right\rangle. \tag{8.10}$$

Here $g_a^{(1)}(t,t')$ and $g_b^{(1)}(t,t')$ denotes the two time correlation function corresponding to the cavity mode $\hat{a}$ and $\hat{b}$, respectively. Finally, the eigen mode decomposition of the two time correlation functions $g_a^{(1)}(t,t')$ and $g_b^{(1)}(t,t')$ given by

$$g_a^{(1)}(t,t') = \sum_i n_{ai} v_{ai}^*(t) v_{ai}(t'), \tag{8.11}$$

$$g_b^{(1)}(t,t') = \sum_i n_{bi} v_{bi}^*(t) v_{bi}(t'), \tag{8.12}$$

gives us the output mode $v_{ai}(t)$ and $v_{bi}(t)$, respectively along with the associated photon excitation number n_{ai} and n_{bi}, respectively.

In the next section, we consider the input field as fock state $|1\rangle$ and verify the photon-subtraction process using the Hamiltonian in Eq. (8.2), with the decay channels described by Eqs. (8.3) and (8.4).

8.2.1 Input with fock state $|1\rangle$

We start with the simplest case when the input field is a single fock state, $|1\rangle$ with

a Gaussian pulse shape given by

$$u_a(t) = \frac{1}{\sqrt{\tau}\pi^{1/4}} \exp\left\{-\frac{(t-t_0)^2}{2\tau^2}\right\}, \tag{8.13}$$

with temporal width τ.

In order to obtain the complete dynamics of the photon subtraction process, we solve the following master equation for the full system given by

$$\frac{\mathrm{d}\rho}{\mathrm{d}t} = -\mathrm{i}[H_f(t), \rho] + \sum_{i=a,b} \mathcal{D}[L_i]\rho, \tag{8.14}$$

where ρ is the density matrix of the complete system with

$$\mathcal{D}[\hat{L}_i]\rho = \frac{1}{2}\left(2\hat{L}_i\rho\hat{L}_i^\dagger - \hat{L}_i^\dagger\hat{L}_i\rho - \rho\hat{L}_i^\dagger\hat{L}_i\right). \tag{8.15}$$

Here, H_f is the Hamiltonian for the full system given by Eq. (8.2), while $\mathcal{D}[\hat{L}_a(t)]$ and $\mathcal{D}[\hat{L}_b(t)]$ describe the corresponding Lindblad dissipators in Eq. (8.3) and (8.4). Note that we do not consider the finite decay rate of the atom into account which will be discussed later.

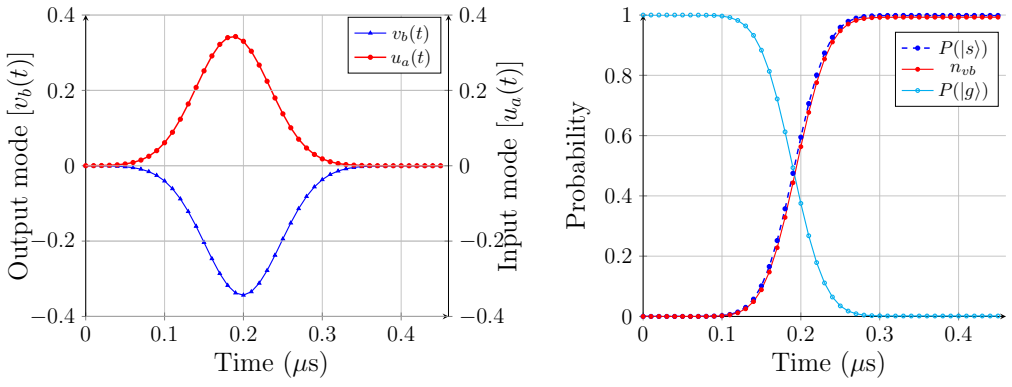

(a) (b)

Figure 8.3: Input fock state $|1\rangle$. (a) Output mode shape obtained from the vertical cavity mode (red) corresponding to the fock state $|1\rangle$ and the input pulse with Gaussian profile $u_a(t)$ (blue). (b) Probability of the atom in $|g\rangle$ and $|s\rangle$ and mean excitation in the output mode $n_{vb} = \left\langle b_v^\dagger b_v \right\rangle$. The cavity parameters taken for the calculations are $(g, \kappa) = 2\pi \times (30, 60)$ MHz.

Since we have a single photon pulse in the input, the photon subtraction in this case would simply correspond to vacuum in the mode $\hat{a}_v$ and a single photon in the

mode $\hat{b}_v$. We expect the single photon in the output mode $\hat{b}_v$ with the same mode shape as that of the input pulse. To confirm this, we first calculate the two time correlation functions corresponding to the two decay channels given by Eq. (8.11) and (8.12). It is found that the eigenmode decomposition of the autocorrelation function $g_b^{(1)}(t,t')$ gives a single mode with the same Gaussian pulse shape as that of the input. This single mode carries single excitation while there is no photon in the output mode $\hat{a}_v$. Fig. 8.3(a) shows the numerically obtained shape of the output mode $v_b(t)$ (shown in blue) along with the input pulse shape (shown in red). From Fig. 8.3(a), it is confirmed that we obtain the same Gaussian profile as the input pulse except for a phase difference.

Next, we take this same Gaussian shape for the output mode and solve the master equation in Eq. (8.14) for the full system. The initial state of the full system given by $\rho(0) = |\Psi(0)\rangle\langle\Psi(0)|$, with

$$\begin{aligned} |\Psi(0)\rangle &= |\psi\rangle_{ua} \otimes |\psi\rangle_{ub} \otimes |\psi\rangle_a \otimes |\psi\rangle_b \otimes |\psi\rangle_A \otimes |\psi\rangle_{va} \otimes |\psi\rangle_{vb} \\ &= |1\rangle_{ua} |0\rangle_{ub} |0\rangle_a |0\rangle_b |g\rangle_A |0\rangle_{va} |0\rangle_{vb} . \end{aligned} \tag{8.16}$$

Here, $|\psi\rangle_{ua}$ and $|\psi\rangle_{ub}$ represents the initial state of the two input virtual cavities which are coupled to the cavity modes $\hat{a}$ and $\hat{b}$ respectively. Similarly, $|\psi\rangle_{va}$ and $|\psi\rangle_{vb}$ represent the initial state of the two virtual output cavities. $|\psi\rangle_a$ and $|\psi\rangle_b$ are the initial state corresponding to the horizontal and vertical cavity modes $\hat{a}$ and $\hat{b}$ respectively, and $|\psi\rangle_A$ is the initial state of the three-level atom.

Taking the initial state as specified in Eq. (8.16) and numerically solving the master equation of the full system gives us the final state of the complete system i.e., $\rho(t)$. We plot the probability of the atom in the state $|g\rangle$ and $|s\rangle$ and the mean excitation in the virtual output cavity mode $\hat{b}_v$ given by $n_{vb} = \langle b_v^\dagger b_v \rangle$ as a function of time in Fig. 8.3(b). From Fig. 8.3(b), its clear that there is a complete transfer of the atomic state from $|g\rangle$ to $|s\rangle$ with time. Furthermore, the average excitation in the virtual output cavity i.e., n_{vb} saturates to ~ 1 as the atomic state goes to $|s\rangle$. This indicates the complete capture of the output mode $v_b(t)$ by the virtual output cavity. Thus, the single photon in the input pulse is completely transferred to the vertical cavity mode and confirms the photon-subtraction process. All these numerical calculations are performed using the QuTiP toolbox [102, 162]. The cavity

parameters taken for the above calculations are $(g, \kappa, \tau^{-1}) = 2\pi \times (30, 60, 3)$ MHz which gives the required condition, $\kappa\tau \gg 1$ for the population transfer from the atomic state $|g\rangle$ to $|s\rangle$ leading to the photon-subtraction [14].

Hence, for a single photon in the input field, we get a corresponding single mode in the output mode $\hat{b}_v$ upon the photon-subtraction. However, as we will see, this simplified description of single photon subtraction fails when we consider the input fock state with more than one photon which is discussed in the subsequent sections.

8.2.2 Input with fock state $|2\rangle$

Here, we consider the input state as fock state $|2\rangle$ with the same Gaussian pulse shape given by Eq. (8.13). Owing to the photon subtraction process, one expects the subtraction of a single photon from the input state $|2\rangle$ in this case also. It is expected that the subtracted single photon should show up as a single mode output from the vertical cavity mode, while the remaining single photon should come out from the output of the horizontal cavity mode.

Surprisingly, this is not the case for the input field consisting of fock state $|2\rangle$, and we observe multiple output modes in the output field from both cavities. To understand this multi-mode character of the output field, we calculate the set of most prominent output modes and the mean excitation associated with each of these modes.

Figs. 8.4(a) and 8.4(b) show the set of the most prominent orthogonal output modes obtained numerically, along with the number of excitation carried by each mode. From Fig. 8.4, it is clear that the output field from both the cavities is scattered over multiple modes. The excitation carried by the most prominent mode in the output from both cavities is ~ 0.84. Thus, the single excitation in the output field is now distributed over the multiple orthogonal modes.

Nevertheless, the sum of the total excitation corresponding to all the output modes for each cavity is ~ 1 i.e., $\sum_i n_{ai} = \sum_i n_{bi} = 1$. This is expected as the total excitation has to be conserved since we did not consider the spontaneous decay

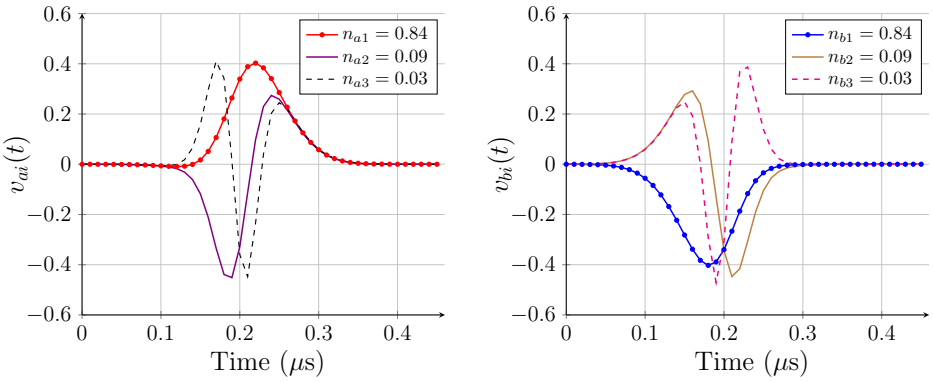

(a) (b)

Figure 8.4: Input fock state $|2\rangle$. (a), (b) First three prominent output modes from horizontal and vertical cavity modes, respectively, along with the photon fraction corresponding to each mode.

rate of the atomic state $|e\rangle$ into the free space modes. Thus, the total excitation $(\sum_i n_{ai} + \sum_i n_{bi} = 2)$ is conserved. The effect of the finite decay rate shows up as a decrease in the total excitation carried by the output field modes (see Appendix C for more details). However, obtaining the correct mode shape and the corresponding mean excitation is not enough to get the complete knowledge of the state of these output modes. In the next section, we analyse the output state of these modes.

8.2.2.1 State of the output field

Once we get the set of most prominent output modes corresponding to the two cavity modes, we can find out the associated state of these output modes using Eq. (8.14). Let $\rho_{v_{a1},v_{a2}..v_{an},v_{b1},v_{b2},..v_{bn}}$ represents the total output state density matrix. The marginal density matrix of any output mode can be calculated from here. There are mainly two states of interest, the density matrix of the photon subtracted state and the density matrix of the single photon state. We focus on these two states in the output. This requires taking into account all the orthogonal modes, which increases the numerical complexity due to the increase in the Hilbert space dimensions of the density matrix. However, we can still find out the output state considering only the first two prominent orthogonal modes from each cavity i.e. (v_{a1}, v_{a2}) and (v_{b1}, v_{b_2}) respectively since they carry most amount of the total excitation i.e., $n_{a1} + n_{a2} =$

$n_{b1} + n_{b2} \sim 0.93$.

The density matrix $\rho_{v_{a1},v_{a2}}$ for the photon subtracted state coming out of the horizontal cavity in the fock basis $\{|0,0\rangle, |0,1\rangle, |1,0\rangle, |1,1\rangle\}$ is given by

$$\rho_{v_{a1},v_{a2}} = \begin{pmatrix} 0.07 & 0 & 0 & 0 \\ 0 & 0.1 & -0.08 & 0 \\ 0 & -0.08 & 0.83 & 0 \\ 0 & 0 & 0 & 0 \end{pmatrix}. \tag{8.17}$$

Similarly, the density matrix $\rho_{v_{b1},v_{b2}}$ for the output from the vertical cavity mode is obtained to be

$$\rho_{v_{b1},v_{b2}} = \begin{pmatrix} 0.07 & 0 & 0 & 0 \\ 0 & 0.1 & 0.07 & 0 \\ 0 & 0.07 & 0.83 & 0 \\ 0 & 0 & 0 & 0 \end{pmatrix}, \tag{8.18}$$

which reiterates the fact that the contribution of the photon emission into the first mode is highest, which carries maximum excitation (~ 0.83). Also, these two density matrix indicates that the two output modes in the photon-subtracted state as well as the single photon state are correlated with each other.

We can also obtain the individual density matrix of the most prominent mode for the photon subtracted and the single photon state which turn out to be the same and are given by (in the basis $\{|0\rangle, |1\rangle\}$)

$$\rho_{va1} \simeq \rho_{vb1} = \begin{pmatrix} 0.17 & 0 \\ 0 & 0.83 \end{pmatrix}. \tag{8.19}$$

In order to see whether there is any correlation between the photon subtracted state and the single photon state, we also calculate the joint density matrix of the most prominent output mode of the photon subtracted field and the single photon state, which is given by

$$\rho_{v_{a1},v_{b1}} = \begin{pmatrix} 0.168 & 0 & 0 & 0 \\ 0 & 0.005 & 0 & 0 \\ 0 & 0 & 0.003 & 0 \\ 0 & 0 & 0 & 0.823 \end{pmatrix}, \tag{8.20}$$

which is a diagonal matrix and does not show any entanglement between the two modes. Note that there is a finite contribution from the vacuum in both output modes. This is because we did not take into account all the modes except for the first prominent mode from the output of each cavity i.e., $v_{a1}(t)$ and $v_{b1}(t)$.

8.2.3 Input with fock state $|3\rangle$

For the case when the input state is the fock state $|3\rangle$, we follow the same approach as in the previous section. Fig. 8.5 shows the first three dominant orthogonal output modes from both cavity modes and the mean excitation carried by each mode. The most prominent output mode from the vertical cavity mode carries ~ 0.8 quanta of excitation [Fig. 8.5(b)]. The primary output mode from the horizontal cavity mode carries ~ 1.76 as the mean excitation number [Fig. 8.5(a)].

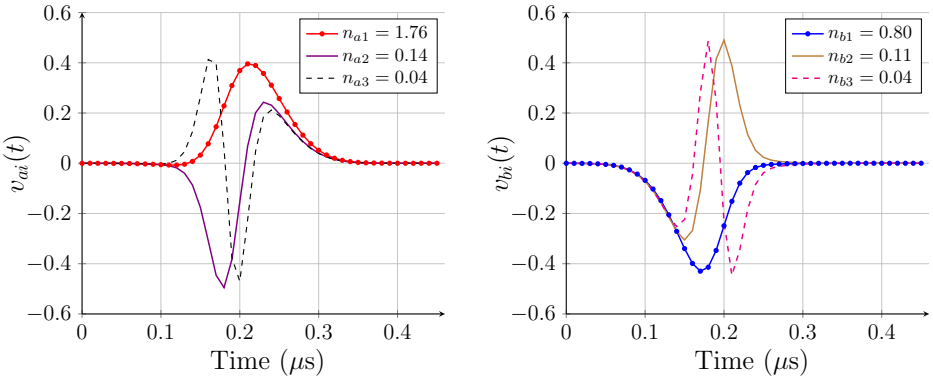

(a) (b)

Figure 8.5: Input fock state $|3\rangle$. (a), (b) First three prominent output modes from horizontal and vertical cavity, respectively, along with the photon excitation corresponding to each mode.

If we consider the total excitation number carried by the output from each cavity,

it follows that $\sum_i n_{ai} = 2$ and $\sum_i n_{bi} = 1$. This confirms that, on average, one photon is subtracted and shows up in the vertical output modes, while the remaining two are present in the output modes of the photon subtracted state. In order to confirm the fock state components associated with each output, we do the output state analysis as discussed in the previous section. The joint density matrix $\rho_{v_{a1},v_{a2}}$ for the photon subtracted state in the basis $\{|0,0\rangle, |0,1\rangle, |1,0\rangle, |0,2\rangle, |1,1\rangle, |2,0\rangle, |1,2\rangle, |2,1\rangle, |2,2\rangle\}$ is obtained as

$$\rho_{v_{a1},v_{a2}} = \begin{pmatrix} 0.01 & 0 & 0 & 0 & 0 & 0 & 0 & 0 & 0 \\ 0 & 0.01 & 1.15\times10^{-3} & 0 & 0 & 0 & 0 & 0 & 0 \\ 0 & 1.15\times10^{-3} & 0.079 & 0 & 0 & 0 & 0 & 0 & 0 \\ 0 & 0 & 0 & 0.01 & -2.36\times10^{-3} & 0.061 & 0 & 0 & 0 \\ 0 & 0 & 0 & -2.36\times10^{-3} & 0.12 & -0.11 & 0 & 0 & 0 \\ 0 & 0 & 0 & 0.061 & -0.11 & 0.77 & 0 & 0 & 0 \\ 0 & 0 & 0 & 0 & 0 & 0 & 6.24\times10^{-5} & -7.06\times10^{-5} & 0 \\ 0 & 0 & 0 & 0 & 0 & 0 & -7.06\times10^{-5} & 7.98\times10^{-5} & 0 \\ 0 & 0 & 0 & 0 & 0 & 0 & 0 & 0 & 0 \end{pmatrix}. \tag{8.21}$$

It is clear from the above density matrix that it is divided into smaller diagonal blocks where the total number of photons is conserved. Similarly, the density matrix for the single photon state $\rho_{v_{b1},v_{b2}}$ for the output from the vertical cavity mode in the basis $\{|0,0\rangle, |0,1\rangle, |1,0\rangle, |1,1\rangle\}$ is given by

$$\rho_{v_{b1},v_{b2}} = \begin{pmatrix} 0.094 & 0 & 0 & 0 \\ 0 & 0.116 & 0.066 & 0 \\ 0 & 0.066 & 0.790 & 0 \\ 0 & 0 & 0 & 0 \end{pmatrix}, \tag{8.22}$$

which again indicates a correlation between the two prominent output modes.

The density matrix of the first two prominent modes of the photon subtracted state in the basis $\{|0\rangle, |1\rangle, |2\rangle\}$ are

$$\rho_{v_{a1}} = \begin{pmatrix} 0.031 & 0 & 0 \\ 0 & 0.199 & 0 \\ 0 & 0 & 0.77 \end{pmatrix}, \quad \rho_{v_{a2}} = \begin{pmatrix} 0.86 & 0 & 0 \\ 0 & 0.13 & 0 \\ 0 & 0 & 0.01 \end{pmatrix}, \tag{8.23}$$

which reveals that in the photon subtraction from the fock state $|3\rangle$, although the photon subtracted modes contain 2 photon excitation, the state of the prominent modes consists of contribution from both $|1\rangle$ as well as $|2\rangle$ fock state. However, the subtracted single photon which shows up in the output from the vertical cavity mode still consists of only fock state $|1\rangle$ component.

8.2.4 Input with superposition state $\frac{|1\rangle + |2\rangle}{\sqrt{2}}$

Here, we discuss the case when the input is in a superposition of fock states $|1\rangle$ and $|2\rangle$ respectively which is an interesting state since it carries 1.5 mean number of photons. To understand how the atom-cavity system interacts with this state as the input, we first obtain the most prominent mode as earlier. Fig 8.6 shows the first three dominant output modes along with the excitation number carried by each mode for the output from both cavities. From Fig. 8.6(b), it is clear that the most prominent mode in the output from the vertical cavity mode carries ~ 0.88 excitation number. Also, the sum of the mean excitation number carried by all modes in this case, is 1 i.e., $\sum_i n_{bi} = 1$, which reiterates that even when we send a superposition state, all the vertical output modes still carry 1 excitation in total. While the remaining 0.5 excitation is being carried by the output modes from the horizontal cavity ($\sum_i n_{ai} = 0.5$) [Fig. 8.6(a)] where the dominant mode carries most of the excitation (~ 0.42). Thus, on average, one photon is being subtracted even when we send a superposition state and shows up in multiple orthogonal output modes.

A close inspection of the orthogonal output modes of the photon subtracted state corresponding to different inputs reveals that the mode shapes are almost the same in each case and do not change when we change the input state. In contrast, the mode shapes of the subtracted single photon differ and depend on the input state

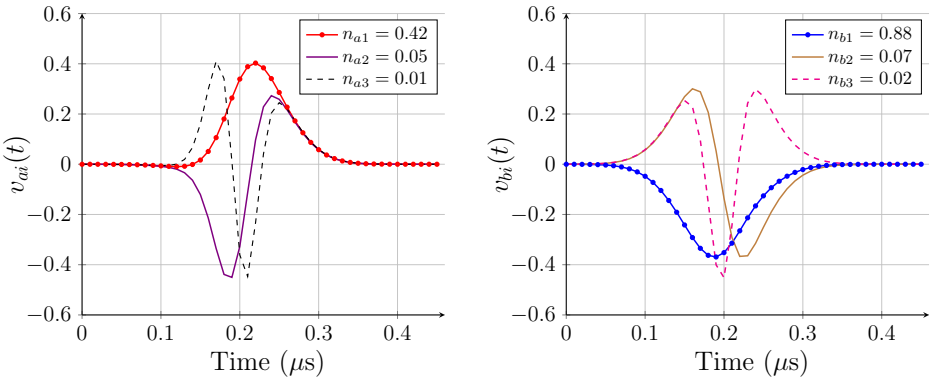

(a) (b)

Figure 8.6: Input state $(|1\rangle + |2\rangle)/\sqrt{2}$. (a), (b) First three prominent output modes from horizontal and vertical cavity, respectively, along with the photon excitation corresponding to each mode.

we send (comparing Fig. 8.6 with Figs. 8.5 and 8.4). The state analysis gives the following joint states for the first two dominant output modes for the single photon field in the basis $\{|0,0\rangle, |0,1\rangle, |1,0\rangle, |1,1\rangle\}$

$$\rho_{v_{b1},v_{b2}} = \begin{pmatrix} 0.05 & 0 & 0 & 0 \\ 0 & 0.078 & -0.061 & 0 \\ 0 & -0.061 & 0.872 & 0 \\ 0 & 0 & 0 & 0 \end{pmatrix}, \tag{8.24}$$

and the density matrix for the photon subtracted field in the basis $\{|0,0\rangle, |0,1\rangle, |1,0\rangle, |1,1\rangle, |2,0\rangle, |2,1\rangle\}$ reads

$$\rho_{v_{a1},v_{a2}} = \begin{pmatrix} 0.537 & -0.004 & -0.417 & 0 & 0 & 0 \\ -0.004 & 0.050 & -0.039 & 7.070\times10^{-6} & -1.281\times10^{-4} & 0 \\ -0.417 & -0.038 & 0.413 & 6.023\times10^{-6} & -1.096\times10^{-4} & 0 \\ 0 & 7.070\times10^{-6} & 6.023\times10^{-6} & 1.208\times10^{-7} & -3.186\times10^{-6} & 0 \\ 0 & -1.281\times10^{-4} & -1.096\times10^{-4} & -3.186\times10^{-6} & 5.792\times10^{-5} & 0 \\ 0 & 0 & 0 & 0 & 0 & 0 \end{pmatrix}. \tag{8.25}$$

8.2.5 Input with weak coherent pulse $|\alpha = 1\rangle$

Studying photon subtraction for the coherent state is challenging as it amounts dealing with large Hilbert space dimensions of the density matrix. Here, we consider a weak coherent pulse with $\alpha = 1$ having a Gaussian pulse shape and calculate only the shape of the output mode obtained from each cavity mode. The output field due to the coherent state is also scattered over multiple modes. Fig. 8.7 shows the first three prominent output modes from each cavity along with the mean excitation contained in each mode.

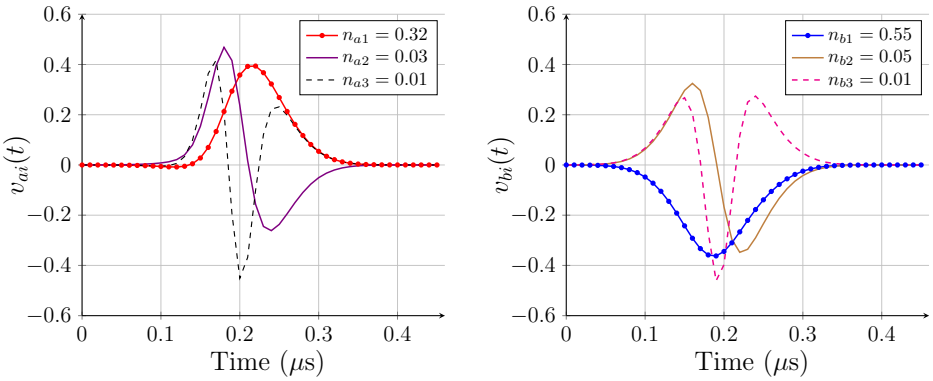

(a) (b)

Figure 8.7: Input coherent state $|\alpha = 1\rangle$. (a), (b) First three prominent output modes from horizontal and vertical cavity, respectively, along with the photon excitation corresponding to each mode.

Interestingly, for the coherent state with $\alpha = 1$, the vertical output mode carries 0.63 excitation in total, indicating that one photon is not subtracted in this case. However, this can be understood, if we look at the expression for the coherent state in fock basis which is given by

$$|\alpha\rangle = \sum_n c_n |n\rangle \tag{8.26}$$

where $c_n = e^{-|\alpha|^2/2} \dfrac{\alpha^n}{\sqrt{n!}}$ denotes the coefficient corresponding to the fock state $|n\rangle$. Here, the coefficient c_0 indicates the coefficient corresponding to the vacuum component, and for $\alpha = 1$, $c_0 = 0.607$. Thus, the remaining excitation probability, which does not correspond to the vacuum, is given by $1 - |c_0|^2 \simeq 0.63$, which matches with the total number of excitations obtained from the vertical cavity mode i.e.

$\sum_i n_{bi} \sim 0.63$ (with $\sum_i n_{bi} + n_{ai} \sim 1$). This suggests that in order to perform photon subtraction using the coherent state, one needs to go for coherent states with higher values of α such that contribution from vacuum component $c_0 \sim 0$. This behaviour of photon subtraction has been observed in [166], where the efficiency of the photon subtraction is less for lower values of α and increases as the strength of the input light increases. Thus, this theory verifies this observation.

Although its difficult to obtain the photon subtracted state as it requires huge hilbert space dimesnions, however, we can obtain the density matrix of the most prominent mode of the single photon state which reads (in the basis $\{|0,0\rangle, |0,1\rangle, |1,0\rangle, |1,1\rangle\}$)

$$\rho_{v_{b1},v_{b2}} = \begin{pmatrix} 0.4 & 0 & 0 & 0 \\ 0 & 0.052 & -0.037 & 0 \\ 0 & -0.037 & 0.548 & 0 \\ 0 & 0 & 0 & 0 \end{pmatrix}, \tag{8.27}$$

which shows the highest contribution from the single photon in the first mode.

This confirms that although there is always a single photon being removed from the input field, however, for the input containing more than one photon, the photon subtracted field, as well as the single photon field, gets scattered into multiple temporal modes with different states for each of the temporal modes.

8.3 Implementation

In the above calculations, we have assumed two degenerate transitions $|g\rangle \leftrightarrow |e\rangle$ and $|s\rangle \leftrightarrow |e\rangle$ are coupled to two orthogonal polarizations. If we consider the transition $|g\rangle \leftrightarrow |e\rangle$ interacts with the right circularly polarized light and $|s\rangle \leftrightarrow |e\rangle$ interacts with the left circularly polarized light, the input field in this case will be selected to be right circularly polarized. To implement this, we can consider the hyperfine levels of an atom in the absence of the external magnetic field, and the atom is coupled to a single bimodal cavity, which can support two degenerate polarization modes. The quantization axis, in this case, is chosen along the cavity axis, and such

setup has also been used to implement atom-photon gates [167, 168]. Alternatively, one can also implement this scheme without using a bimodal cavity by considering an experimental setup as described in [166, 169], where the two degenerate states are used as the two ground states and the corresponding transitions are coupled through a single microresonator deterministically to two different directions of a waveguide. The subtracted single photon, in this case, gets reflected while the rest of the photons are transmitted [166].

Chapter 9

Conclusion

Photons are essential for long-range quantum communication and quantum computation. Quantum teleportation, quantum entanglement, and quantum key distribution are significant areas where photonic quantum information processing has shown dominance. Even though the photons work as excellent flying qubits, specific quantum computation tasks need to store the quantum information encoded in photons which requires quantum memory, which can store and retrieve single photons on demand. Another critical requirement in quantum information processing is to engineer and manipulate the quantum states of light. This can be accomplished through atom-cavity interactions which provide strong coupling between single atom and photons and work as as an interface between the photonic and atomic qubits.

In this thesis, we have reviewed the dynamics of atom-field interactions and their usage in the photonic quantum memory with a particular focus on I-AFC-based quantum memory. We have also discussed the atom-cavity interactions and how they can be used to manipulate the quantum states of light. As an application, we have presented the storage of vector vortex states of light using I-AFC quantum memory. We show that an atomic ensemble consisting of an I-AFC structure and the homogeneous number density in the transverse plane can efficiently store the OAM modes of light. Further, the ensemble of atoms with dual I-AFC, with two frequency combs having similar mean frequencies, can efficiently store the polarization states of light. These two features together result in a quantum memory for VV states.

We have also discussed the factors that affect the quality of the quantum memory and show that the Cs and Rb atoms can serve as promising candidates for storing VV states of light.

We have also presented a scheme to store photons using only a single atom coupled to an optical cavity. The atom exhibits an I-AFC, which enables the joint atom-cavity system to store photons. Ideally, this quantum memory protocol can store photons with $\sim 100\%$ efficiency. We have also discussed the implementation of this scheme using single Cesium and Rubidium atoms coupled to nanophotonic cavities. It allows us to realize an on-chip quantum memory suitable for integrated photonic chips. Although we have presented this quantum memory protocol using trapped atoms, this can also be achieved using quantum dots and quantum defect centers. Since deterministic single photon sources have already been realized using quantum dots, combining them with the on-chip quantum memory can provide a robust integrated platform for photonic quantum computation.

Further, we have also reviewed the atom-cavity interactions in the context of complete input-output theory with quantum pulses, which is an effective tool to obtain the quantum state of the output field mode upon the interaction of an input pulse with atom-cavity systems. Using this, we describe the multi-modal nature of the photon subtraction process using the atom-cavity systems, which provides a clear and better understanding of the photon-subtraction process.

The next step would be to realize the quantum memory using quantum dots. This can provide an integrated and robust platform to achieve scalable quantum information processing. We also plan to utilize the understanding of atom-cavity interactions to implement quantum operations and manipulate the quantum states of light efficiently, which can provide a complete platform for quantum information processing using atom-cavity systems.

Appendix A

Propagation of LG modes in medium

The generalized paraxial wave equation inside a medium reads [Eq. (2.33)]

$$\left[\nabla_{\perp}^{2} + 2ik\left(\frac{\partial}{\partial z} + \frac{1}{c}\frac{\partial}{\partial t}\right)\right]\mathcal{E}(\mathbf{r},t) = -\frac{k^{2}}{\epsilon_{0}}\mathcal{P}(\mathbf{r},t), \tag{A.1}$$

where $\mathcal{P}$ is the induced atomic polarization. Fourier transform of Eq. (A.1) in the transverse plane and the time coordinate results in

$$\frac{\partial\tilde{\mathcal{E}}(\mathbf{q},z,\omega)}{\partial z} = \frac{1}{2ik}\left[(q^{2} + \frac{2wk}{c})\tilde{\mathcal{E}}(\mathbf{q},z,\omega) - \frac{w_{L}k}{c\epsilon_{0}}\tilde{\mathcal{P}}(\mathbf{q},z,\omega)\right]. \tag{A.2}$$

The atomic polarization amplitude $\mathcal{P}$ in terms of atomic coherence ρ_{nm} between the atomic transition $|n\rangle \leftrightarrow |m\rangle$ can be written as [49]

$$\mathcal{P}(\mathbf{r}_{\perp},z,t) = 2\mathcal{N}(\mathbf{r}_{\perp})\sum_{n,m} d_{nm}\rho_{nm}(\mathbf{r}_{\perp},z,t), \tag{A.3}$$

where $\mathcal{N}(\mathbf{r}_{\perp})$ is the atomic distribution function in the transverse plane. The same equation can be written upon taking the Fourier transform in the transverse plane and time, which reads

$$\tilde{\mathcal{P}}(\mathbf{q},z,\omega) = 2\tilde{\mathcal{N}}(\mathbf{q}) * \sum_{n,m} d_{nm}\tilde{\rho}_{nm}(\mathbf{q},z,\omega). \tag{A.4}$$

The dynamical equation for the atomic coherence reads

$$\frac{\partial\rho_{nm}(\mathbf{r}_{\perp},z,t)}{\partial t} + \left(i\Delta_{nm} + \frac{\gamma}{2}\right)\rho_{nm}(\mathbf{r}_{\perp},z,t) = i\frac{d_{nm}\mathcal{E}(\mathbf{r}_{\perp},z,t)}{2\hbar}\rho_{mm}. \tag{A.5}$$

We can solve for $\rho_{nm}(\mathbf{q}, z, w)$ by taking the Fourier transform of Eq. (A.5) w.r.t t and $\mathbf{r}_\perp$. The expression for the Fourier transform of $\rho_{nm}(\mathbf{q}, z, w)$ reads

$$\tilde{\rho}_{nm}(\mathbf{q}, z, w) = \frac{id_{nm}\tilde{\mathcal{E}}(\mathbf{q}, z, \omega)\rho_{mm}}{2\hbar\left[i(\Delta_{nm} + w) + \frac{\gamma}{2}\right]}. \tag{A.6}$$

Substituting Eq. (A.6) in Eq. (A.4) yields

$$\tilde{\mathcal{P}}(\mathbf{q}, z, \omega) = 2\tilde{\mathcal{N}}(\mathbf{q}) * \sum_{n,m} \frac{\mathrm{i}d_{nm}^2\tilde{\mathcal{E}}(\mathbf{q}, z, \omega)\rho_{mm}}{2\hbar\left[\mathrm{i}(\Delta_{nm} + w) + \frac{\gamma}{2}\right]}. \tag{A.7}$$

Substituting above in Eq. (A.2) gives

$$\frac{\partial\tilde{\mathcal{E}}}{\partial z} = \left(\frac{q^2}{2\mathrm{i}k} - \frac{\mathrm{i}\omega}{c}\right)\tilde{\mathcal{E}}(\mathbf{q}, z, \omega) - \tilde{\mathcal{N}}(\mathbf{q}) * \mathcal{D}'(\omega)\tilde{\mathcal{E}}(\mathbf{q}, z, \omega), \tag{A.8}$$

where

$$g'_{mm} = \frac{\omega_L\rho_{mm}}{2c\hbar\epsilon_0}, \;\; \mathcal{D}'(\omega) = \sum_{nm} \frac{g'_{mm}}{\left[\mathrm{i}(\Delta_{nm} + \omega) + \frac{\gamma}{2}\right]} d_{nm}^2. \tag{A.9}$$

Solving Eq. (A.8) will yield the solution for the propagation of electric field through a medium. However, in general solving this equation is difficult.

A simple scenario is the homogeneous medium, where $\mathcal{N}$ is a constant. In this case, the equation can be simplified and the solution reads

$$\tilde{\mathcal{E}}(\mathbf{q}, z, \omega) = \exp\left[\left(\frac{q^2}{2\mathrm{i}k} - \frac{\mathrm{i}\omega}{c} - \mathcal{D}(\omega)\right)z\right]\tilde{\mathcal{E}}(\mathbf{q}, 0, \omega). \tag{A.10}$$

where $\mathcal{D}(\omega) = N\mathcal{D}'(\omega)$ follows from Eq. (4.45) Again, taking inverse Fourier transform ($w \to t$)

$$\tilde{\mathcal{E}}(\mathbf{q}, z, t) = \exp\left(\frac{q^2 z}{2ik}\right)\mathcal{F}^{-1}[\exp\left(-\mathcal{D}(\omega)z\right)] * \mathcal{F}^{-1}\left[\exp\left(-\frac{\mathrm{i}\omega z}{c}\right)\tilde{\mathcal{E}}(\mathbf{q}, 0, \omega)\right], \tag{A.11}$$

and applying convolution gives

$$\begin{aligned}\tilde{\mathcal{E}}(\mathbf{q}, z, t) &= \exp\left(\frac{q^2 z}{2ik}\right)\left[N(z, t)) * \tilde{\mathcal{E}}(\mathbf{q}, 0, t - \frac{z}{c})\right] \\ &= \exp\left(\frac{q^2 z}{2ik}\right)\left[\int N(z, t - \tau)\tilde{\mathcal{E}}(\mathbf{q}, 0, \tau - \frac{z}{c})d\tau\right],\end{aligned} \tag{A.12}$$

where

$$N(t,z) = \mathcal{F}^{-1}[\exp(-\mathcal{D}(\omega)z)] = \frac{1}{2\pi}\int e^{\mathrm{i}\omega t} e^{-\mathcal{D}(\omega)z} dw. \tag{A.13}$$

Now, taking inverse Fourier transform ($\mathbf{q} \to \mathbf{r}_\perp$) and using Eq. (2.45) gives

$$\begin{aligned}
\mathcal{E}(\mathbf{r}_\perp, z, t) =& \mathcal{F}^{-1}\left[\exp\left(\frac{q^2 z}{2\mathrm{i}k}\right)\right] * \mathcal{F}^{-1}\left[\int N(t-\tau, z)\tilde{\mathcal{E}}(\mathbf{q}, 0, \tau - \frac{z}{c})d\tau\right], \\
=& M(\mathbf{r}_\perp, z) * \left[\int N(t-\tau, z)\mathcal{E}(\mathbf{r}_\perp, 0, \tau - \frac{z}{c}))d\tau\right], \\
=& \int M(\mathbf{r}_\perp - \mathbf{r}'_\perp, z)\left[\int N(t-\tau, z)\mathcal{E}(\mathbf{r}'_\perp, 0, \tau - \frac{z}{c})d\tau\right] d^2\mathbf{r}'_\perp.
\end{aligned} \tag{A.14}$$

Appendix B

B.1 Two time correlation function

The two time correlation function in general is defined as $\langle A(t+\tau)B(t)\rangle$ where A and B are the system operators in the Heisenberg picture. It can be written as [159, 170]

$$\langle A(t+\tau)B(t)\rangle = Tr[A(t+\tau)B(t)\rho_{tot}] = Tr_s\{Tr_b\{A(t+\tau)B(t)(\rho_s\otimes\rho_b\})\} \quad \text{(B.1)}$$

where ρ_s and ρ_b represents the system and bath density matrix respectively. This can be further simplified by using the time evolution for the operators and the density matrix [159, 170]

$$A(t+\tau) = e^{\mathrm{i}H(t+\tau)}Ae^{-\mathrm{i}H(t+\tau)}, \quad \text{(B.2)}$$

$$B(t) = e^{\mathrm{i}Ht}Be^{-\mathrm{i}Ht}, \quad \text{(B.3)}$$

$$\rho_{tot}(t) = e^{-\mathrm{i}Ht}\rho_{tot}e^{\mathrm{i}Ht}, \quad \text{(B.4)}$$

which gives

$$\begin{aligned}\langle A(t+\tau)B(t)\rangle =& Tr_s\big\{Tr_b\big\{e^{\mathrm{i}H(t+\tau)}Ae^{-\mathrm{i}H(t+\tau)}e^{\mathrm{i}Ht}Be^{-\mathrm{i}Ht}(\rho_s\otimes\rho_b)\big\}\big\}\\ =& Tr_s\big\{Tr_b\big\{Ae^{-\mathrm{i}H\tau}B\rho_{tot}(t)e^{\mathrm{i}H\tau}\big\}\big\}\\ =& Tr_s\big\{A\ Tr_b\big\{e^{-\mathrm{i}H\tau}B\rho_{tot}(t)e^{\mathrm{i}H\tau}\big\}\big\}\\ =& Tr_s\{A\ Tr_b\{X(\tau,t)\}\},\end{aligned} \quad \text{(B.5)}$$

where $X(\tau,t) = e^{-\mathrm{i}H\tau}B\rho_{tot}(t)e^{\mathrm{i}H\tau}$.

In order to solve it further, we consider the equation of motion for the quantity $X(\tau, t)$ w.r.t τ which is given by [159]

$$\frac{\partial}{\partial \tau} X(\tau, t) = \frac{1}{\mathrm{i}\hbar}[H, X(\tau, t)], \tag{B.6}$$

where $X(0, t) = B\rho_{tot}(t)$. To obtain the reduced dynamics of the system alone, we need to calculate the trace over $X(\tau, t)$ w.r.t bath which can be written as [1]

$$Tr_b\{X(\tau, t)\} = V(t+\tau, t) Tr_b\{X(0, t)\} = V(t+\tau, t)\{B\rho(t)\}, \tag{B.7}$$

where $\rho(t) = Tr_b\{\rho_{tot}\}$ is the reduced density matrix for the system alone in the Schrodinger picture. Thus, the final expression for the two-time correlation function can be written as

$$\langle A(t+\tau)B(t)\rangle = Tr_s\{A\ V(t+\tau, t)\{B\rho(t)\}\}, \tag{B.8}$$

which is entirely in terms of the system operators and the reduced density matrix for the system.

Following the similar procedure, we can write the correlation function corresponding to $\langle A(t)B(t+\tau)\rangle$ which is given by

$$\begin{aligned}
\langle A(t)B(t+\tau)\rangle =& Tr_s\Big\{Tr_b\Big\{e^{\mathrm{i}Ht}Ae^{-\mathrm{i}Ht}e^{\mathrm{i}H(t+\tau)}Be^{-\mathrm{i}H(t+\tau)}\rho_{tot}\Big\}\Big\} \\
=& Tr_s\Big\{B\ Tr_b\Big\{e^{-\mathrm{i}H\tau}\rho_{tot}(t)Ae^{\mathrm{i}H\tau}\Big\}\Big\} \\
=& Tr_s\{B\ V(t+\tau, t)\{\rho(t)A\}\}.
\end{aligned} \tag{B.9}$$

Note that if the operators A and B are Hermitian conjugate of each other i.e., $A = B^\dagger$, then

$$\langle A(t+\tau)B(t)\rangle = \langle A(t)B(t+\tau)\rangle^\dagger. \tag{B.10}$$

Using this, one can calculate the two-time correlation function $g^{(1)}(t, t') = \left\langle \hat{L}_0^\dagger(t)\hat{L}_0(t')\right\rangle$ as

$$g^{(1)}(t, t') = Tr\Big\{\hat{L}_0^\dagger(t)V(t, t')\Big\{\hat{L}_0(t')\rho_{us}(t')\Big\}\Big\} = Tr\Big\{\hat{L}_0^\dagger(t)V(t, t')\Big\{\hat{L}_0(t')V(t', 0)\rho_{us}(0)\Big\}\Big\}. \tag{B.11}$$

[1] In the same way as the density matrix ρ satisfies the master equation $\rho(t) = V(t, t_0)\rho(t_0)$, with $V(t, t_0)$ being the time evolution operator, the quantity $Tr_b\{X(\tau, t)\}$ also satisfies the master equation as a function of τ.

B.2 Monte Carlo wave-function method

Solving the dynamics of quantum system interacting with a reservoir using the master equation approach can pose difficulty if the Hilbert space dimensions of the quantum system of interest, N is large. The corresponding order of density matrix is N^2 which creates difficulty for solving the dynamics for large value of N. Monte Carlo wave-function method is an alternate and equivalent approach, This method serves as an efficient computational tool that reduces the dimensionality from N^2 elements to N and is a very useful technique to study the quantum systems with large values of N. In this section, we give a brief overview of this technique.

The evolution in this approach is governed by the Schrödinger equation using an effective non-Hermitian Hamiltonian and the random quantum jumps which which is used to evolve the wave function which is basically a N dimensional state vector. The following steps describe the Monte Carlo wave function procedure [163]

1. Consider a system in a state $\psi(t)$ at time t, which is a normalized wave function. To evolve the system from time t to a time $t + \delta t$, an effective non-Hermitian Hamiltonian is used which is given by

$$H = H_S - \frac{\mathrm{i}\hbar}{2} \sum_n L_n^\dagger L_n, \tag{B.12}$$

where H_S is the system Hamiltonian and L_n are the collapse operators or the Lindblad jump operators corresponding to the Lindblad dissipator [Eq. (2.37)].

2. This gives the wave function at time $t + \delta t$, for a small time-step δt as

$$\begin{aligned} |\psi(t+\delta t)\rangle =& e^{-\mathrm{i}H\delta t/\hbar} |\psi(t)\rangle \\ \simeq& \left(1 - \frac{\mathrm{i}H_{eff}}{\hbar}\delta t\right) |\psi(t)\rangle \\ \equiv& \left|\psi^{(1)}(t+\delta t)\right\rangle . \end{aligned} \tag{B.13}$$

3. This wave function after the evolution is not normalized due to the non-Hermitian Hamiltonian which reduces the norm of the evolved wave function

to

$$\begin{aligned}\langle\psi(t+\delta t)|\psi(t+\delta t)\rangle =& 1-\delta t\frac{\mathrm{i}}{\hbar}\langle\psi(t)|H_{eff}-H_{eff}^{\dagger}|\psi(t)\rangle\\ =& 1-\delta t\sum_{n}\langle\psi(t)|L_{n}^{\dagger}L_{n}|\psi(t)\rangle\\ =& 1-\sum_{n}\delta p_{n}\\ =& 1-\delta p,\end{aligned} \tag{B.14}$$

where $\delta p=\sum_n \delta p_n$, with $\delta p_n=\delta t\,\langle\psi(t)|L_n^{\dagger}L_n|\psi(t)\rangle$.

Here the time step δt is chosen such that $\delta p(=\sum_n \delta t\,\langle\psi(t)|L_n^{\dagger}L_n|\psi(t)\rangle)\ll 1$.[2] Thus the probability of remaining in the state $\psi(t)$ is $1-\delta p$, while δp represents the probability of making a quantum jump.

4. The next step of the evolution of the wave function involves a quantum jump, which is directly related to the probability δp. To decide whether a quantum jump occurs or not, a random number, r is drawn between 0 to 1 and compared with δp.

5. If r is greater than δp, (which occurs most of the times since $\delta p\ll 1$), no quantum jump occurs, and the new normalized wave-function is taken at time $t+\delta t$ which reads

$$|\psi(t+\delta t)\rangle\;|_{\text{No jump}}=\frac{|\psi(t+\delta t)\rangle}{\sqrt{1-\delta p}},\qquad\qquad (r>\delta p) \tag{B.15}$$

6. If r is less than δp, a quantum jump occurs, and the new wave function is chosen out of the different states $L_n|\psi(t)\rangle$ with the corresponding probability $P_n=\delta p_n/\delta p$ ($\sum_n P_n=1$) giving the final normalized wave-function after jump as

$$|\psi(t+\delta t)\rangle\;|_{\text{Jump}}=\frac{L_n|\psi(t)\rangle}{\sqrt{\delta p_n/\delta t}}=\frac{L_n|\psi(t)\rangle}{\sqrt{\langle\psi(t)|L_n^{\dagger}L_n|\psi(t)\rangle}},\qquad\qquad (r<\delta p) \tag{B.16}$$

7. The system is evolved further using the steps from 2 to 6 to get the new normalized wave function at time $t+2\delta t$ and continued till the state is evolved

[2] This ensures that the probability of more than one quantum jump in the same time step is zero.

to a final time t_f. The entire process of evolving the state to final time is repeated multiple times which gives different trajectories in each run and the final state is the average over all possible outcomes for sufficiently large number of runs.

It can be shown that the above procedure is equivalent to the master equation approach [163]. For this we consider the quantity $\overline{\sigma(t)}$ which is averaged over $\sigma(t) = |\psi(t)\rangle\langle\psi(t)|$ obtained from different trajectories after the evolution from $|\psi(0)\rangle$ to $|\psi(t)\rangle$. For a Monte Carlo wave function $|\psi(t)\rangle$, at time t, the average value of $\overline{\sigma(t+\delta t)}$ at time $t+\delta t$, can be written as

$$\overline{\sigma(t+\delta t)} = (1-\delta p)\frac{\left|\psi^{(1)}(t+\delta t)\right\rangle}{\sqrt{1-\delta p}}\frac{\left\langle\psi^{(1)}(t+\delta t)\right|}{\sqrt{1-\delta p}} + \delta p\sum_n \frac{\delta p_n}{\delta p}\frac{L_n|\psi(t)\rangle}{\sqrt{\delta p_n/\delta t}}\frac{\langle\psi(t)|L_n^\dagger}{\sqrt{\delta p_n/\delta t}}. \tag{B.17}$$

Using (B.13), the above equation can be simplified to

$$\overline{\sigma(t+\delta t)} = \sigma(t) + \delta t\frac{\mathrm{i}}{\hbar}[\sigma(t), H_S] + \delta t\sum_n \mathcal{D}[L_n]\sigma(t), \tag{B.18}$$

where L_n are the jump operator with

$$\mathcal{D}[L_n]\sigma(t) = \frac{1}{2}\left[2L_n\sigma(t)L_n^\dagger - L_n^\dagger L_n\sigma(t) - \sigma(t)L_n^\dagger L_n\right]. \tag{B.19}$$

Averaging the above equation over $\overline{\sigma(t)}$ yields

$$\frac{\mathrm{d}\overline{\sigma(t)}}{\mathrm{d}t} = \frac{\mathrm{i}}{\hbar}\left[\overline{\sigma(t)}, H_S\right] + \sum_n \mathcal{D}[L_n]\overline{\sigma(t)}, \tag{B.20}$$

which is the Lindblad master equation in terms of $\overline{\sigma(t)}$ [3]. Thus, for a large number of trajectories, the Monte Carlo method is similar to the master equation approach.

Furthermore, the expectation value of any system observable, A in terms of system density matrix is given by $\langle A\rangle = Tr[\rho_s(t)A]$. This can be extended to Monte Carlo method in order to obtain the expectation values. This requires to calculate the quantum average over all the possible outcomes $\left|\psi^{(i)}(t)\right\rangle$ using Monte Carlo

[3]Here, it is assumed that the the the density matrix $\rho_s(0)$ at time $t = 0$ coincides with $|\psi(0)\rangle\langle\psi(0)|$.

method i.e., obtaining $\langle\psi^{(i)}(t)|A|\psi^{(i)}(t)\rangle$. The expectation value of the observable A is then given by the average over all the posible outcomes $|\psi^{(i)}(t)\rangle$and reads

$$\langle A\rangle_m = \frac{1}{m}\sum_{i=1}^{m}\langle\psi^{(i)}(t)|A|\psi^{(i)}(t)\rangle\,, \tag{B.21}$$

where m is the number of trajectories, and is chosen to be sufficiently large such that

$$\langle A\rangle_m \equiv \langle A\rangle\,. \tag{B.22}$$

Thus, the Monte Carlo method is an efficient and effective technique which reduces the Hilbert space dimensions from N^2 to N and takes lesser memory and computational time for very large values of N.

Appendix C

Effect of the atomic decay rate on the photon subtraction process

Here, we discuss the effect of decay rate of the excited state $|e\rangle$ on the photon subtraction. The finite decay rate of the excited state affects the probability of the photon-subtracion. We consider the spontaneous decay rate of the excited state $|e\rangle$ to the two ground states $|g\rangle$ and $|s\rangle$ to be γ_a. To incorporate this into the dynamics, we consider two additional Lindblad terms corresponding to the two decay channels, $\hat{L}_1 = \sqrt{\gamma_a}\,|g\rangle\langle e|$, and $\hat{L}_2 = \sqrt{\gamma_a}\,|s\rangle\langle e|$.

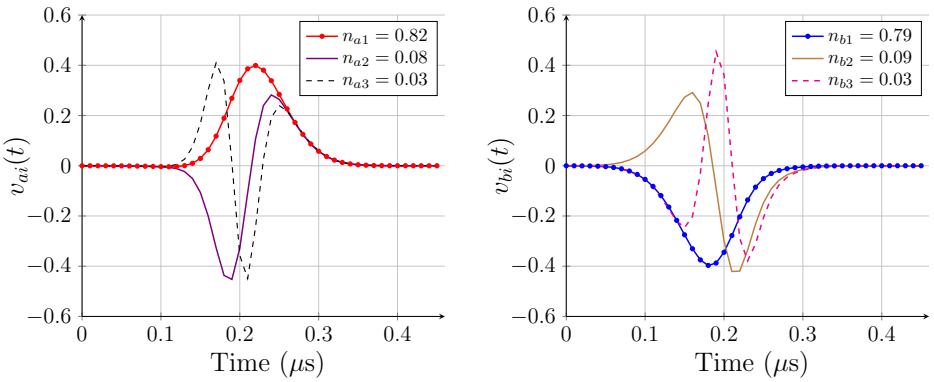

(a) (b)

Figure C.1: Input fock state $|2\rangle$ including finite decay rate of atom. (a), (b) First three prominent output modes from horizontal and vertical cavity respectively along with the photon excitation corresponding to each mode.

We consider an example of the input state as fock state $|2\rangle$ with a Gaussian pulse shape and solve the dynamics for the photon-subtraction including the decay rate of the excited state. Fig. C.1 shows the prominent modes from the output from of both cavities. The atom-cavity parameters for the calculations are taken to be $(g, \kappa, \gamma_a) = 2\pi \times (30, 60, 3)$ MHz. However, in this case the total photon number number in the output field is not conserved, because of the spontaneous emission of into the free space modes. The total excitation carried by the output field from the vertical cavity is $\sum_i n_{bi} = 0.94$, while the total excitation contained in the subtracted field from the horizontal cavity mode is $\sum_i n_{ai} = 0.96$. The total excitation sums to 1.9 indicating the loss due to spontaneous emission. Nevertheless, we still get the single photon subtraction as before.

This small drop in the total excitation is observed for the case of other input states also. Thus, the effect of the decay rate of the atom shows up as a decrease in the total excitation carried by the output field, while it does not affect the shape of the multiple output modes.

Bibliography

[1] Michael A. Nielsen and Isaac L. Chuang. *Quantum Computation and Quantum Information: 10th Anniversary Edition*. Cambridge University Press, 2010.

[2] Thaddeus D Ladd, Fedor Jelezko, Raymond Laflamme, Yasunobu Nakamura, Christopher Monroe, and Jeremy Lloyd O'Brien. Quantum computers. *nature*, 464(7285):45–53, 2010.

[3] Fulvio Flamini, Nicolo Spagnolo, and Fabio Sciarrino. Photonic quantum information processing: a review. *Reports on Progress in Physics*, 82(1):016001, 2018.

[4] Sergei Slussarenko and Geoff J Pryde. Photonic quantum information processing: A concise review. *Applied Physics Reviews*, 6(4):041303, 2019.

[5] Pieter Kok, William J Munro, Kae Nemoto, Timothy C Ralph, Jonathan P Dowling, and Gerard J Milburn. Linear optical quantum computing with photonic qubits. *Reviews of modern physics*, 79(1):135, 2007.

[6] Valerio Scarani, Helle Bechmann-Pasquinucci, Nicolas J. Cerf, Miloslav Dušek, Norbert Lütkenhaus, and Momtchil Peev. The security of practical quantum key distribution. *Rev. Mod. Phys.*, 81:1301–1350, Sep 2009.

[7] Stefano Pirandola, Ulrik L Andersen, Leonardo Banchi, Mario Berta, Darius Bunandar, Roger Colbeck, Dirk Englund, Tobias Gehring, Cosmo Lupo, Carlo Ottaviani, et al. Advances in quantum cryptography. *Advances in Optics and Photonics*, 12(4):1012–1236, 2020.

[8] Dik Bouwmeester, Jian-Wei Pan, Klaus Mattle, Manfred Eibl, Harald Wein-

furter, and Anton Zeilinger. Experimental quantum teleportation. *Nature*, 390(6660):575–579, 1997.

[9] Xi-Lin Wang, Xin-Dong Cai, Zu-En Su, Ming-Cheng Chen, Dian Wu, Li Li, Nai-Le Liu, Chao-Yang Lu, and Jian-Wei Pan. Quantum teleportation of multiple degrees of freedom of a single photon. *Nature*, 518(7540):516–519, 2015.

[10] Nicolas Sangouard, Christoph Simon, Hugues De Riedmatten, and Nicolas Gisin. Quantum repeaters based on atomic ensembles and linear optics. *Reviews of Modern Physics*, 83(1):33, 2011.

[11] Alexander I Lvovsky, Barry C Sanders, and Wolfgang Tittel. Optical quantum memory. *Nat. Photonics*, 3(12):706–714, 2009.

[12] C Simon, M Afzelius, J Appel, A Boyer de la Giroday, SJ Dewhurst, N Gisin, CY Hu, F Jelezko, S Kröll, JH Müller, et al. Quantum memories-a review based on the european integrated project "qubit applications (qap)" p. *The European Physical Journal D*, 58(1), 2010.

[13] Khabat Heshami, Duncan G England, Peter C Humphreys, Philip J Bustard, Victor M Acosta, Joshua Nunn, and Benjamin J Sussman. Quantum memories: emerging applications and recent advances. *J. Mod. Opt.*, 63(20):2005–2028, 2016.

[14] Julio Gea-Banacloche and William Wilson. Photon subtraction and addition by a three-level atom in an optical cavity. *Phys. Rev. A*, 88:033832, Sep 2013.

[15] Bastian Hacker, Stephan Welte, Severin Daiss, Armin Shaukat, Stephan Ritter, Lin Li, and Gerhard Rempe. Deterministic creation of entangled atom–light schrödinger-cat states. *Nature Photonics*, 13(2):110–115, 2019.

[16] J McKeever, A Boca, AD Boozer, R Miller, JR Buck, A Kuzmich, and HJ Kimble. Deterministic generation of single photons from one atom trapped in a cavity. *Science*, 303(5666):1992–1994, 2004.

[17] Martin Mücke, Joerg Bochmann, Carolin Hahn, Andreas Neuzner, Christian Nölleke, Andreas Reiserer, Gerhard Rempe, and Stephan Ritter. Generation

of single photons from an atom-cavity system. *Phys. Rev. A*, 87:063805, Jun 2013.

[18] Kevin M Birnbaum, Andreea Boca, Russell Miller, Allen D Boozer, Tracy E Northup, and H Jeff Kimble. Photon blockade in an optical cavity with one trapped atom. *Nature*, 436(7047):87–90, 2005.

[19] Christoph Hamsen, Karl Nicolas Tolazzi, Tatjana Wilk, and Gerhard Rempe. Two-photon blockade in an atom-driven cavity qed system. *Physical review letters*, 118(13):133604, 2017.

[20] Andreas Reiserer and Gerhard Rempe. Cavity-based quantum networks with single atoms and optical photons. *Rev. Mod. Phys.*, 87:1379–1418, Dec 2015.

[21] H Jeff Kimble. The quantum internet. *Nature*, 453(7198):1023–1030, 2008.

[22] Christoph Simon. Towards a global quantum network. *Nat. Photonics*, 11(11):678–680, 2017.

[23] L-M Duan, Mikhail D Lukin, J Ignacio Cirac, and Peter Zoller. Long-distance quantum communication with atomic ensembles and linear optics. *Nature*, 414(6862):413–418, 2001.

[24] Zeng-Bing Chen, Bo Zhao, Yu-Ao Chen, Jörg Schmiedmayer, and Jian-Wei Pan. Fault-tolerant quantum repeater with atomic ensembles and linear optics. *Phys. Rev. A*, 76:022329, Aug 2007.

[25] Nicolas Sangouard, Christoph Simon, Hugues de Riedmatten, and Nicolas Gisin. Quantum repeaters based on atomic ensembles and linear optics. *Rev. Mod. Phys.*, 83:33–80, Mar 2011.

[26] M. Fleischhauer and M. D. Lukin. Quantum memory for photons: Dark-state polaritons. *Phys. Rev. A*, 65:022314, Jan 2002.

[27] David Höckel and Oliver Benson. Electromagnetically induced transparency in cesium vapor with probe pulses on the single-photon level. *Phys. Rev. Lett.*, 105:153605, Oct 2010.

[28] Ya-Fen Hsiao, Pin-Ju Tsai, Hung-Shiue Chen, Sheng-Xiang Lin, Chih-Chiao Hung, Chih-Hsi Lee, Yi-Hsin Chen, Yong-Fan Chen, Ite A. Yu, and Ying-Cheng Chen. Highly efficient coherent optical memory based on electromagnetically induced transparency. *Phys. Rev. Lett.*, 120:183602, May 2018.

[29] Yunfei Wang, Jianfeng Li, Shanchao Zhang, Keyu Su, Yiru Zhou, Kaiyu Liao, Shengwang Du, Hui Yan, and Shi-Liang Zhu. Efficient quantum memory for single-photon polarization qubits. *Nat. Photonics*, 13(5):346, 2019.

[30] S. A. Moiseev and S. Kröll. Complete reconstruction of the quantum state of a single-photon wave packet absorbed by a doppler-broadened transition. *Phys. Rev. Lett.*, 87:173601, Oct 2001.

[31] B. Kraus, W. Tittel, N. Gisin, M. Nilsson, S. Kröll, and J. I. Cirac. Quantum memory for nonstationary light fields based on controlled reversible inhomogeneous broadening. *Phys. Rev. A*, 73:020302, Feb 2006.

[32] A. L. Alexander, J. J. Longdell, M. J. Sellars, and N. B. Manson. Photon echoes produced by switching electric fields. *Phys. Rev. Lett.*, 96:043602, Feb 2006.

[33] Nicolas Sangouard, Christoph Simon, Mikael Afzelius, and Nicolas Gisin. Analysis of a quantum memory for photons based on controlled reversible inhomogeneous broadening. *Phys. Rev. A*, 75:032327, Mar 2007.

[34] Ivan Iakoupov and Anders S Sørensen. An efficient quantum memory based on two-level atoms. *New Journal of Physics*, 15(8):085012, 2013.

[35] G. Hétet, J. J. Longdell, A. L. Alexander, P. K. Lam, and M. J. Sellars. Electro-optic quantum memory for light using two-level atoms. *Phys. Rev. Lett.*, 100:023601, Jan 2008.

[36] Morgan P Hedges, Jevon J Longdell, Yongmin Li, and Matthew J Sellars. Efficient quantum memory for light. *Nature*, 465(7301):1052–1056, 2010.

[37] Mahdi Hosseini, Ben M Sparkes, Geoff Campbell, Ping K Lam, and Ben C Buchler. High efficiency coherent optical memory with warm rubidium vapour. *Nat. Commun.*, 2:174, 2011.

[38] J Nunn, IA Walmsley, MG Raymer, K Surmacz, FC Waldermann, Z Wang, and D Jaksch. Mapping broadband single-photon wave packets into an atomic memory. *Physical Review A*, 75(1):011401, 2007.

[39] Mason Klein, M Hohensee, A Nemiroski, Y Xiao, DF Phillips, and RL Walsworth. Slow light in narrow paraffin-coated vapor cells. *Appl. Phys. Lett.*, 95(9):091102, 2009.

[40] KF Reim, P Michelberger, KC Lee, J Nunn, NK Langford, and IA Walmsley. Single-photon-level quantum memory at room temperature. *Physical Review Letters*, 107(5):053603, 2011.

[41] A. E. Kozhekin, K. Mølmer, and E. Polzik. Quantum memory for light. *Phys. Rev. A*, 62:033809, Aug 2000.

[42] Jinxian Guo, Xiaotian Feng, Peiyu Yang, Zhifei Yu, LQ Chen, Chun-Hua Yuan, and Weiping Zhang. High-performance raman quantum memory with optimal control in room temperature atoms. *Nat. Commun.*, 10(1):148, 2019.

[43] Mikael Afzelius, Christoph Simon, Hugues de Riedmatten, and Nicolas Gisin. Multimode quantum memory based on atomic frequency combs. *Phys. Rev. A*, 79:052329, May 2009.

[44] Mikael Afzelius, Imam Usmani, Atia Amari, Björn Lauritzen, Andreas Walther, Christoph Simon, Nicolas Sangouard, Ji ří Minář, Hugues de Riedmatten, Nicolas Gisin, and Stefan Kröll. Demonstration of atomic frequency comb memory for light with spin-wave storage. *Phys. Rev. Lett.*, 104:040503, Jan 2010.

[45] Pierre Jobez, Nuala Timoney, Cyril Laplane, Jean Etesse, Alban Ferrier, Philippe Goldner, Nicolas Gisin, and Mikael Afzelius. Towards highly multimode optical quantum memory for quantum repeaters. *Phys. Rev. A*, 93:032327, Mar 2016.

[46] Adrian Holzäpfel, Jean Etesse, Krzysztof T Kaczmarek, Alexey Tiranov, Nicolas Gisin, and Mikael Afzelius. Optical storage for 0.53 s in a solid-state atomic frequency comb memory using dynamical decoupling. *New Journal of Physics*, 22(6):063009, 2020.

[47] Moritz Businger, Alexey Tiranov, Krzysztof T Kaczmarek, Sacha Welinski, Z Zhang, A Ferrier, P Goldner, and Mikael Afzelius. Optical spin-wave storage in a solid-state hybridized electron-nuclear spin ensemble. *Physical review letters*, 124(5):053606, 2020.

[48] Sebastian P. Horvath, Mohammed K. Alqedra, Adam Kinos, Andreas Walther, Jan Marcus Dahlström, Stefan Kröll, and Lars Rippe. Noise-free on-demand atomic frequency comb quantum memory. *Phys. Rev. Res.*, 3:023099, May 2021.

[49] G. P. Teja, Christoph Simon, and Sandeep K. Goyal. Photonic quantum memory using an intra-atomic frequency comb. *Phys. Rev. A*, 99:052314, May 2019.

[50] G. P. Teja and Sandeep K. Goyal. Studying the effect of fluctuating environment on intra-atomic frequency comb based quantum memory. *Sci. Rep.*, 11(1):11439, Jun 2021.

[51] Chanchal, G. P. Teja, Christoph Simon, and Sandeep K. Goyal. Storing vector-vortex states of light in an intra-atomic frequency-comb quantum memory. *Phys. Rev. A*, 104:043713, Oct 2021.

[52] Yunfei Wang, Jianfeng Li, Shanchao Zhang, Keyu Su, Yiru Zhou, Kaiyu Liao, Shengwang Du, Hui Yan, and Shi-Liang Zhu. Efficient quantum memory for single-photon polarization qubits. *Nature Photonics*, 13(5):346–351, 2019.

[53] Zong-Quan Zhou, Jian Wang, Chuan-Feng Li, and Guang-Can Guo. Efficient spectral hole-burning and atomic frequency comb storage in nd3+: Ylif4. *Scientific reports*, 3(1):2754, 2013.

[54] Valentina Parigi, Vincenzo D'Ambrosio, Christophe Arnold, Lorenzo Marrucci, Fabio Sciarrino, and Julien Laurat. Storage and retrieval of vector beams of light in a multiple-degree-of-freedom quantum memory. *Nature communications*, 6:7706, 2015.

[55] EA Vashukevich, T Yu Golubeva, and Yu M Golubev. Conversion and storage of modes with orbital angular momentum in a quantum memory scheme. *Physical Review A*, 101(3):033830, 2020.

[56] Cyril Laplane, Pierre Jobez, Jean Etesse, Nuala Timoney, Nicolas Gisin, and Mikael Afzelius. Multiplexed on-demand storage of polarization qubits in a crystal. *New Journal of Physics*, 18(1):013006, 2015.

[57] Tian-Shu Yang, Zong-Quan Zhou, Yi-Lin Hua, Xiao Liu, Zong-Feng Li, Pei-Yun Li, Yu Ma, Chao Liu, Peng-Jun Liang, Xue Li, et al. Multiplexed storage and real-time manipulation based on a multiple degree-of-freedom quantum memory. *Nature communications*, 9(1):1–8, 2018.

[58] Daniel Viscor, Alessandro Ferraro, Yu Loiko, J Mompart, and Verònica Ahufinger. Quantum-state storage and processing for polarization qubits in an inhomogeneously broadened λ-type three-level medium. *Physical Review A*, 84(4):042314, 2011.

[59] D. B. Higginbottom, B. M. Sparkes, M. Rancic, O. Pinel, M. Hosseini, P. K. Lam, and B. C. Buchler. Spatial-mode storage in a gradient-echo memory. *Phys. Rev. A*, 86:023801, Aug 2012.

[60] Mahdi Hosseini, Ben M Sparkes, Gabriel Hétet, Jevon J Longdell, Ping Koy Lam, and Ben C Buchler. Coherent optical pulse sequencer for quantum applications. *Nature*, 461(7261):241–245, 2009.

[61] Antonio Ortu, Adrian Holzäpfel, Jean Etesse, and Mikael Afzelius. Storage of photonic time-bin qubits for up to 20 ms in a rare-earth doped crystal. *NPJ Quantum Inf.*, 8(1):1–7, 2022.

[62] Vincenzo D'Ambrosio, Gonzalo Carvacho, Francesco Graffitti, Chiara Vitelli, Bruno Piccirillo, Lorenzo Marrucci, and Fabio Sciarrino. Entangled vector vortex beams. *Phys. Rev. A*, 94:030304, Sep 2016.

[63] Julio T Barreiro, Tzu-Chieh Wei, and Paul G Kwiat. Remote preparation of single-photon "hybrid" entangled and vector-polarization states. *Physical review letters*, 105(3):030407, 2010.

[64] Daniele Cozzolino, Emanuele Polino, Mauro Valeri, Gonzalo Carvacho, Davide Bacco, Nicolò Spagnolo, Leif KK Oxenløwe, and Fabio Sciarrino. Air-core fiber distribution of hybrid vector vortex-polarization entangled states. *Advanced Photonics*, 1(4):046005, 2019.

[65] Vincenzo D'ambrosio, Nicolo Spagnolo, Lorenzo Del Re, Sergei Slussarenko, Ying Li, Leong Chuan Kwek, Lorenzo Marrucci, Stephen P Walborn, Leandro Aolita, and Fabio Sciarrino. Photonic polarization gears for ultra-sensitive angular measurements. *Nature communications*, 4(1):1–8, 2013.

[66] Andrea Crespi, Roberta Ramponi, Roberto Osellame, Linda Sansoni, Irene Bongioanni, Fabio Sciarrino, Giuseppe Vallone, and Paolo Mataloni. Integrated photonic quantum gates for polarization qubits. *Nat. Commun.*, 2(1):1–6, 2011.

[67] M Kohnen, M Succo, PG Petrov, RA Nyman, M Trupke, and EA Hinds. An array of integrated atom–photon junctions. *Nat. Photonics*, 5(1):35–38, 2011.

[68] Y Meng, J Lee, M Dagenais, and SL Rolston. A nanowaveguide platform for collective atom-light interaction. *Applied Physics Letters*, 107(9):091110, 2015.

[69] Bastian Hacker, Stephan Welte, Gerhard Rempe, and Stephan Ritter. A photon–photon quantum gate based on a single atom in an optical resonator. *Nature*, 536(7615):193–196, 2016.

[70] Ravitej Uppu, Freja T Pedersen, Ying Wang, Cecilie T Olesen, Camille Papon, Xiaoyan Zhou, Leonardo Midolo, Sven Scholz, Andreas D Wieck, Arne Ludwig, et al. Scalable integrated single-photon source. *Science advances*, 6(50):eabc8268, 2020.

[71] A Laucht, S Pütz, T Günthner, N Hauke, R Saive, S Frédérick, M Bichler, M-C Amann, AW Holleitner, M Kaniber, et al. A waveguide-coupled on-chip single-photon source. *Physical Review X*, 2(1):011014, 2012.

[72] Chao-Yang Lu and Jian-Wei Pan. Quantum-dot single-photon sources for the quantum internet. *Nat. Nanotechnol.*, 16(12):1294–1296, 2021.

[73] Shaojie Yin, Huaqing Qiu, Zhibin Wang, Daoxin Dai, and Xiaowei Guan. On-chip silicon switchable polarization beam splitter. *Optics Letters*, 47(4):961–964, 2022.

[74] Samuel Gyger, Julien Zichi, Lucas Schweickert, Ali W Elshaari, Stephan Steinhauer, Saimon F Covre da Silva, Armando Rastelli, Val Zwiller, Klaus D Jöns, and Carlos Errando-Herranz. Reconfigurable photonics with on-chip single-photon detectors. *Nat. Commun.*, 12(1):1–8, 2021.

[75] Tian Zhong, Jonathan M Kindem, John G Bartholomew, Jake Rochman, Ioana Craiciu, Evan Miyazono, Marco Bettinelli, Enrico Cavalli, Varun Verma, Sae Woo Nam, et al. Nanophotonic rare-earth quantum memory with optically controlled retrieval. *Science*, 357(6358):1392–1395, 2017.

[76] Chao Liu, Tian-Xiang Zhu, Ming-Xu Su, You-Zhi Ma, Zong-Quan Zhou, Chuan-Feng Li, and Guang-Can Guo. On-demand quantum storage of photonic qubits in an on-chip waveguide. *Phys. Rev. Lett.*, 125:260504, Dec 2020.

[77] Chanchal, G. P. Teja, and Sandeep K. Goyal. Intra-atomic frequency-comb-based photonic quantum memory using single-atom-cavity setup. *Phys. Rev. A*, 107:012614, Jan 2023.

[78] C. W. Gardiner and M. J. Collett. Input and output in damped quantum systems: Quantum stochastic differential equations and the master equation. *Phys. Rev. A*, 31:3761–3774, Jun 1985.

[79] Alexander Holm Kiilerich and Klaus Mølmer. Input-output theory with quantum pulses. *Phys. Rev. Lett.*, 123:123604, Sep 2019.

[80] Alexander Holm Kiilerich and Klaus Mølmer. Quantum interactions with pulses of radiation. *Phys. Rev. A*, 102:023717, Aug 2020.

[81] M. S. Kim, E. Park, P. L. Knight, and H. Jeong. Nonclassicality of a photon-subtracted gaussian field. *Phys. Rev. A*, 71:043805, Apr 2005.

[82] Stefano Olivares and Matteo GA Paris. Squeezed fock state by inconclusive photon subtraction. *Journal of Optics B: Quantum and Semiclassical Optics*, 7(12):S616, 2005.

[83] J. S. Neergaard-Nielsen, B. Melholt Nielsen, C. Hettich, K. Mølmer, and E. S. Polzik. Generation of a superposition of odd photon number states for quantum information networks. *Phys. Rev. Lett.*, 97:083604, Aug 2006.

[84] Asoka Biswas and G. S. Agarwal. Nonclassicality and decoherence of photon-subtracted squeezed states. *Phys. Rev. A*, 75:032104, Mar 2007.

[85] Hiroki Takahashi, Kentaro Wakui, Shigenari Suzuki, Masahiro Takeoka, Kazuhiro Hayasaka, Akira Furusawa, and Masahide Sasaki. Generation of large-amplitude coherent-state superposition via ancilla-assisted photon subtraction. *Phys. Rev. Lett.*, 101:233605, Dec 2008.

[86] GS Agarwal. Engineering non-gaussian entangled states with vortices by photon subtraction. *New Journal of Physics*, 13(7):073008, 2011.

[87] Valentina Parigi, Alessandro Zavatta, Myungshik Kim, and Marco Bellini. Probing quantum commutation rules by addition and subtraction of single photons to/from a light field. *Science*, 317(5846):1890–1893, 2007.

[88] A Zavatta, V Parigi, MS Kim, and M Bellini. Subtracting photons from arbitrary light fields: experimental test of coherent state invariance by single-photon annihilation. *New Journal of Physics*, 10(12):123006, 2008.

[89] B Barrett, A Bertoldi, and P Bouyer. Inertial quantum sensors using light and matter. *Physica Scripta*, 91(5):053006, 2016.

[90] Tatjana Wilk, Simon C Webster, Axel Kuhn, and Gerhard Rempe. Single-atom single-photon quantum interface. *Science*, 317(5837):488–490, 2007.

[91] Christopher Gerry, Peter Knight, and Peter L Knight. *Introductory quantum optics*. Cambridge university press, 2005.

[92] David J Griffiths. Introduction to electrodynamics, 2005.

[93] Marlan O Scully and M Suhail Zubairy. Quantum optics, 1999.

[94] M. Lukin. (unpublished).

[95] Heinz-Peter Breuer, Francesco Petruccione, et al. *The theory of open quantum systems*. Oxford University Press on Demand, 2002.

[96] Les Allen, Marco W Beijersbergen, RJC Spreeuw, and JP Woerdman. Orbital angular momentum of light and the transformation of laguerre-gaussian laser modes. *Physical Review A*, 45(11):8185, 1992.

[97] L Allen, MJ Padgett, and M Babiker. Iv the orbital angular momentum of light. In *Progress in optics*, volume 39, pages 291–372. Elsevier, 1999.

[98] Rodney Loudon. *The quantum theory of light*. OUP Oxford, 2000.

[99] Edwin T Jaynes and Frederick W Cummings. Comparison of quantum and semiclassical radiation theories with application to the beam maser. *Proceedings of the IEEE*, 51(1):89–109, 1963.

[100] Bruce W Shore and Peter L Knight. The jaynes-cummings model. *Journal of Modern Optics*, 40(7):1195–1238, 1993.

[101] Michel Brune, F Schmidt-Kaler, Abdelhamid Maali, J Dreyer, E Hagley, JM Raimond, and S Haroche. Quantum rabi oscillation: A direct test of field quantization in a cavity. *Physical review letters*, 76(11):1800, 1996.

[102] J Robert Johansson, Paul D Nation, and Franco Nori. Qutip: An open-source python framework for the dynamics of open quantum systems. *Computer Physics Communications*, 183(8):1760–1772, 2012.

[103] GJ Milburn and S Basiri-Esfahani. Quantum optics with one or two photons. *Proceedings of the Royal Society A: Mathematical, Physical and Engineering Sciences*, 471(2180):20150208, 2015.

[104] Ben Q. Baragiola and Joshua Combes. Quantum trajectories for propagating fock states. *Phys. Rev. A*, 96:023819, Aug 2017.

[105] L.-M. Duan, B. Wang, and H. J. Kimble. Robust quantum gates on neutral atoms with cavity-assisted photon scattering. *Phys. Rev. A*, 72:032333, Sep 2005.

[106] Andreas Reiserer, Norbert Kalb, Gerhard Rempe, and Stephan Ritter. A quantum gate between a flying optical photon and a single trapped atom. *Nature*, 508(7495):237–240, 2014.

[107] Pierre Vernaz-Gris, Kun Huang, Mingtao Cao, Alexandra S Sheremet, and Julien Laurat. Highly-efficient quantum memory for polarization qubits in a spatially-multiplexed cold atomic ensemble. *Nature communications*, 9(1):1–6, 2018.

[108] Connor Kupchak, Thomas Mittiga, Bertus Jordaan, Mehdi Namazi, Christian Nölleke, and Eden Figueroa. Room-temperature single-photon level memory for polarization states. *Scientific reports*, 5(1):1–5, 2015.

[109] Mehdi Namazi, Connor Kupchak, Bertus Jordaan, Reihaneh Shahrokhshahi, and Eden Figueroa. Ultralow-noise room-temperature quantum memory for polarization qubits. *Physical Review Applied*, 8(3):034023, 2017.

[110] Zhongxiao Xu, Yuelong Wu, Long Tian, Lirong Chen, Zhiying Zhang, Zhihui Yan, Shujing Li, Hai Wang, Changde Xie, and Kunchi Peng. Long lifetime and high-fidelity quantum memory of photonic polarization qubit by lifting zeeman degeneracy. *Physical review letters*, 111(24):240503, 2013.

[111] Mustafa Gündoğan, Patrick M Ledingham, Attaallah Almasi, Matteo Cristiani, and Hugues de Riedmatten. Quantum storage of a photonic polarization qubit in a solid. *Physical review letters*, 108(19):190504, 2012.

[112] Zong-Quan Zhou, Wei-Bin Lin, Ming Yang, Chuan-Feng Li, and Guang-Can Guo. Realization of reliable solid-state quantum memory for photonic polarization qubit. *Physical review letters*, 108(19):190505, 2012.

[113] Christoph Clausen, Félix Bussieres, Mikael Afzelius, and Nicolas Gisin. Quantum storage of heralded polarization qubits in birefringent and anisotropically absorbing materials. *Physical review letters*, 108(19):190503, 2012.

[114] Zachary Dutton and Janne Ruostekoski. Transfer and storage of vortex states in light and matter waves. *Physical review letters*, 93(19):193602, 2004.

[115] Rami Pugatch, Moshe Shuker, Ofer Firstenberg, Amiram Ron, and Nir Davidson. Topological stability of stored optical vortices. *Physical review letters*, 98(20):203601, 2007.

[116] D Moretti, D Felinto, and JWR Tabosa. Collapses and revivals of stored orbital angular momentum of light in a cold-atom ensemble. *Physical Review A*, 79(2):023825, 2009.

[117] Dong-Sheng Ding, Zhi-Yuan Zhou, Bao-Sen Shi, and Guang-Can Guo. Single-photon-level quantum image memory based on cold atomic ensembles. *Nature communications*, 4(1):1–7, 2013.

[118] Lucile Veissier, Adrien Nicolas, Lambert Giner, Dominik Maxein, AS Sheremet, Elisabeth Giacobino, and Julien Laurat. Reversible optical memory for twisted photons. *Optics letters*, 38(5):712–714, 2013.

[119] A Nicolas, L Veissier, L Giner, E Giacobino, D Maxein, and J Laurat. A quantum memory for orbital angular momentum photonic qubits. *Nature Photonics*, 8(3):234, 2014.

[120] Zhengyang Bai, Datang Xu, and Guoxiang Huang. Storage and retrieval of electromagnetic waves with orbital angular momentum via plasmon-induced transparency. *Optics express*, 25(2):785–798, 2017.

[121] Shuai Shi, Dong-Sheng Ding, Wei Zhang, Zhi-Yuan Zhou, Ming-Xin Dong, Shi-Long Liu, Kai Wang, Bao-Sen Shi, and Guang-Can Guo. Transverse azimuthal dephasing of a vortex spin wave in a hot atomic gas. *Physical Review A*, 95(3):033823, 2017.

[122] Ying-Hao Ye, Ming-Xin Dong, Yi-Chen Yu, Dong-Sheng Ding, and Bao-Sen Shi. Experimental realization of optical storage of vector beams of light in warm atomic vapor. *Optics letters*, 44(7):1528–1531, 2019.

[123] Holger P Specht, Christian Nölleke, Andreas Reiserer, Manuel Uphoff, Eden Figueroa, Stephan Ritter, and Gerhard Rempe. A single-atom quantum memory. *Nature*, 473(7346):190–193, 2011.

[124] Norbert Kalb, Andreas Reiserer, Stephan Ritter, and Gerhard Rempe. Heralded storage of a photonic quantum bit in a single atom. *Physical review letters*, 114(22):220501, 2015.

[125] D Viscor, A Ferraro, Yu Loiko, R Corbalán, J Mompart, and V Ahufinger. Optical quantum memory for polarization qubits with v-type three-level atoms. *Journal of Physics B: Atomic, Molecular and Optical Physics*, 44(19):195504, 2011.

[126] Y-W Cho, GT Campbell, JL Everett, J Bernu, DB Higginbottom, MT Cao, J Geng, NP Robins, PK Lam, and BC Buchler. Highly efficient optical quantum memory with long coherence time in cold atoms. *Optica*, 3(1):100–107, 2016.

[127] Brian Harold Bransden and Charles Jean Joachain. *Physics of atoms and molecules*. Pearson Education India, 2003.

[128] Les Allen, M. Babiker, and W.L. Power. Azimuthal doppler-shift in light-beams with orbital angular-momentum. *Optics Communications*, 112:141–144, 11 1994.

[129] W. L. Power, L. Allen, M. Babiker, and V. E. Lembessis. Atomic motion in light beams possessing orbital angular momentum. *Phys. Rev. A*, 52:479–488, Jul 1995.

[130] S. Barreiro, J. W. R. Tabosa, H. Failache, and A. Lezama. Spectroscopic observation of the rotational doppler effect. *Phys. Rev. Lett.*, 97:113601, Sep 2006.

[131] Leonard Mandel and Emil Wolf. *Optical coherence and quantum optics*. Cambridge university press, 1995.

[132] Abdoulaye Camara, Robin Kaiser, and Guillaume Labeyrie. Scaling behavior of a very large magneto-optical trap. *Physical Review A*, 90(6):063404, 2014.

[133] N Radwell, G Walker, and S Franke-Arnold. Cold-atom densities of more than 10 12 cm- 3 in a holographically shaped dark spontaneous-force optical trap. *Physical Review A*, 88(4):043409, 2013.

[134] Shayne Bennetts, Chun-Chia Chen, Benjamin Pasquiou, Florian Schreck, et al. Steady-state magneto-optical trap with 100-fold improved phase-space density. *Physical review letters*, 119(22):223202, 2017.

[135] Kyle N Jarvis, JA Devlin, TE Wall, BE Sauer, and MR Tarbutt. Blue-detuned magneto-optical trap. *Physical review letters*, 120(8):083201, 2018.

[136] Solomon Freer, Stephanie Simmons, Arne Laucht, Juha T Muhonen, Juan P Dehollain, Rachpon Kalra, Fahd A Mohiyaddin, Fay E Hudson, Kohei M

Itoh, Jeffrey C McCallum, et al. A single-atom quantum memory in silicon. *Quantum Science and Technology*, 2(1):015009, 2017.

[137] James G Titchener, Markus Gräfe, René Heilmann, Alexander S Solntsev, Alexander Szameit, and Andrey A Sukhorukov. Scalable on-chip quantum state tomography. *NPJ Quantum Inf.*, 4(1):1–6, 2018.

[138] Ali W Elshaari, Wolfram Pernice, Kartik Srinivasan, Oliver Benson, and Val Zwiller. Hybrid integrated quantum photonic circuits. *Nat. Photonics*, 14(5):285–298, 2020.

[139] Jianwei Wang, Fabio Sciarrino, Anthony Laing, and Mark G Thompson. Integrated photonic quantum technologies. *Nat. Photonics*, 14(5):273–284, 2020.

[140] A Kiraz, C Reese, B Gayral, Lidong Zhang, WV Schoenfeld, BD Gerardot, PM Petroff, EL Hu, and Atac Imamoglu. Cavity-quantum electrodynamics with quantum dots. *Journal of Optics B: Quantum and Semiclassical Optics*, 5(2):129, 2003.

[141] JM An, A Franceschetti, and A Zunger. The excitonic exchange splitting and radiative lifetime in pbse quantum dots. *Nano Lett.*, 7(7):2129–2135, 2007.

[142] Pengfei Zhang, Gang Song, and Li Yu. Optical trapping of single quantum dots for cavity quantum electrodynamics. *Photonics Res.*, 6(3):182–185, 2018.

[143] Dana E Westmoreland, Kevin P McClelland, Kaitlyn A Perez, James C Schwabacher, Zhengyi Zhang, and Emily A Weiss. Properties of quantum dots coupled to plasmons and optical cavities. *J. Chem. Phys.*, 151(21):210901, 2019.

[144] Dirk Heinze, Dominik Breddermann, Artur Zrenner, and Stefan Schumacher. A quantum dot single-photon source with on-the-fly all-optical polarization control and timed emission. *Nat. Commun.*, 6(1):1–6, 2015.

[145] Feng Liu, Alistair J Brash, John O'Hara, Luis MPP Martins, Catherine L Phillips, Rikki J Coles, Benjamin Royall, Edmund Clarke, Christopher Bentham, Nikola Prtljaga, et al. High purcell factor generation of indistinguishable on-chip single photons. *Nat. Nanotechnol.*, 13(9):835–840, 2018.

[146] C. Y. Hu and J. G. Rarity. Extended linear regime of cavity-qed enhanced optical circular birefringence induced by a charged quantum dot. *Phys. Rev. B*, 91:075304, Feb 2015.

[147] Yue Chang, T. Shi, Yu-xi Liu, C. P. Sun, and Franco Nori. Multistability of electromagnetically induced transparency in atom-assisted optomechanical cavities. *Phys. Rev. A*, 83:063826, Jun 2011.

[148] Mustafa Gündoğan, Patrick M. Ledingham, Kutlu Kutluer, Margherita Mazzera, and Hugues de Riedmatten. Solid state spin-wave quantum memory for time-bin qubits. *Phys. Rev. Lett.*, 114:230501, Jun 2015.

[149] D. van Oosten and L. Kuipers. Trapping a single atom with a fraction of a photon using a photonic crystal nanocavity. *Phys. Rev. A*, 84:011802, Jul 2011.

[150] Jeffrey Douglas Thompson, TG Tiecke, Nathalie Pulmones de Leon, J Feist, AV Akimov, M Gullans, Alexander S Zibrov, V Vuletić, and Mikhail D Lukin. Coupling a single trapped atom to a nanoscale optical cavity. *Science*, 340(6137):1202–1205, 2013.

[151] David Hunger, Tilo Steinmetz, Yves Colombe, Christian Deutsch, Theodor W Hänsch, and Jakob Reichel. A fiber fabry–perot cavity with high finesse. *New J. Phys.*, 12(6):065038, 2010.

[152] Jean E Sansonetti. Wavelengths, transition probabilities, and energy levels for the spectra of rubidium (rb i through rb xxxvii). *Journal of physical and chemical reference data*, 35(1):301–421, 2006.

[153] JE Sansonetti. Wavelengths, transition probabilities, and energy levels for the spectra of cesium (cs i–cs lv). *Journal of Physical and Chemical Reference Data*, 38(4):761–923, 2009.

[154] C. W. Gardiner. Driving a quantum system with the output field from another driven quantum system. *Phys. Rev. Lett.*, 70:2269–2272, Apr 1993.

[155] H. J. Carmichael. Quantum trajectory theory for cascaded open systems. *Phys. Rev. Lett.*, 70:2273–2276, Apr 1993.

[156] Joshua Combes, Joseph Kerckhoff, and Mohan Sarovar. The slh framework for modeling quantum input-output networks. *Advances in Physics: X*, 2(3):784–888, 2017.

[157] John E Gough and Matthew R James. The series product for gaussian quantum input processes. *Reports on Mathematical Physics*, 79(1):111–133, 2017.

[158] Jing Zhang, Yu-xi Liu, Re-Bing Wu, Kurt Jacobs, and Franco Nori. Non-markovian quantum input-output networks. *Phys. Rev. A*, 87:032117, Mar 2013.

[159] Crispin Gardiner and Peter Zoller. *Quantum noise: a handbook of Markovian and non-Markovian quantum stochastic methods with applications to quantum optics*. Springer Science & Business Media, 2004.

[160] C. Fabre and N. Treps. Modes and states in quantum optics. *Rev. Mod. Phys.*, 92:035005, Sep 2020.

[161] Olivier Morin, Claude Fabre, and Julien Laurat. Experimentally accessing the optimal temporal mode of traveling quantum light states. *Phys. Rev. Lett.*, 111:213602, Nov 2013.

[162] J.R. Johansson, P.D. Nation, and Franco Nori. Qutip 2: A python framework for the dynamics of open quantum systems. *Computer Physics Communications*, 184(4):1234–1240, 2013.

[163] Klaus Mølmer, Yvan Castin, and Jean Dalibard. Monte carlo wave-function method in quantum optics. *JOSA B*, 10(3):524–538, 1993.

[164] Alexei Ourjoumtsev, Aurélien Dantan, Rosa Tualle-Brouri, and Philippe Grangier. Increasing entanglement between gaussian states by coherent photon subtraction. *Phys. Rev. Lett.*, 98:030502, Jan 2007.

[165] Carlos Navarrete-Benlloch, Raúl García-Patrón, Jeffrey H. Shapiro, and Nicolas J. Cerf. Enhancing quantum entanglement by photon addition and subtraction. *Phys. Rev. A*, 86:012328, Jul 2012.

[166] Serge Rosenblum, Orel Bechler, Itay Shomroni, Yulia Lovsky, Gabriel Guendelman, and Barak Dayan. Extraction of a single photon from an optical pulse. *Nature Photonics*, 10(1):19–22, 2016.

[167] Adrien Borne, Tracy E Northup, Rainer Blatt, and Barak Dayan. Efficient ion-photon qubit swap gate in realistic ion cavity-qed systems without strong coupling. *Optics express*, 28(8):11822–11839, 2020.

[168] Kazuki Koshino, Satoshi Ishizaka, and Yasunobu Nakamura. Deterministic photon-photon $\sqrt{\text{swap}}$gate using a Λ system. *Phys. Rev. A*, 82:010301, Jul 2010.

[169] Itay Shomroni, Serge Rosenblum, Yulia Lovsky, Orel Bechler, Gabriel Guendelman, and Barak Dayan. All-optical routing of single photons by a one-atom switch controlled by a single photon. *Science*, 345(6199):903–906, 2014.

[170] Howard Carmichael. *An open systems approach to quantum optics: lectures presented at the Université Libre de Bruxelles, October 28 to November 4, 1991*, volume 18. Springer Science & Business Media, 2009.